

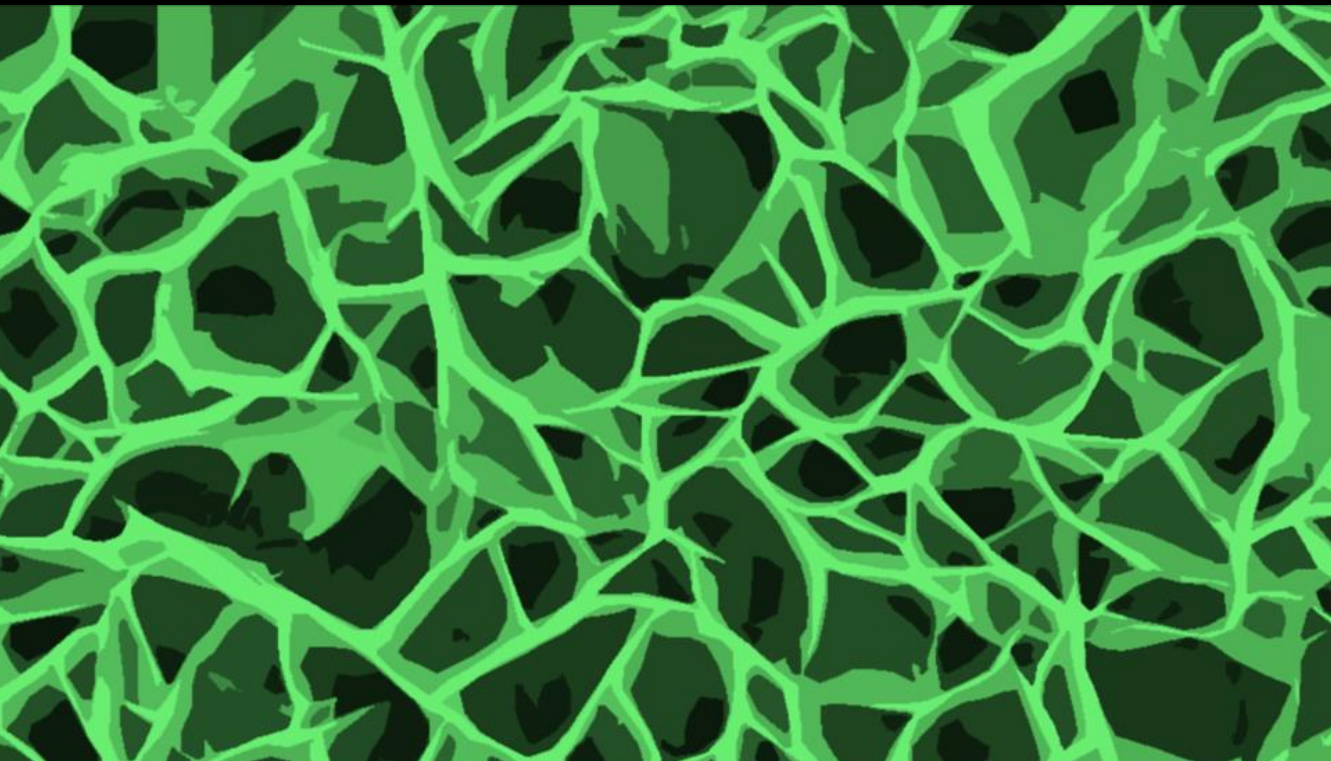
UNIVERSITÀ DEGLI STUDI DI CATANIA
IN CONVENZIONE CON
UNIVERSITÀ DEGLI STUDI DI PALERMO

DOTTORATO DI RICERCA IN
SCIENZA DEI MATERIALI E NANOTECNOLOGIE - XXXII CICLO

**NOVEL NI-BASED NANOSTRUCTURES:
SYNTHESIS AND APPLICATION IN
SENSING AND ENERGY STORAGE**

MARIO URSO

TUTOR: PROF. FRANCESCO PRIOLO
PROF. SALVO MIRABELLA
COORDINATORE: PROF.SSA MARIA GRAZIA GRIMALDI





UNIVERSITÀ DEGLI STUDI DI CATANIA

IN CONVENZIONE CON



UNIVERSITÀ DEGLI STUDI DI PALERMO

DOTTORATO DI RICERCA IN

SCIENZA DEI MATERIALI E NANOTECNOLOGIE - XXXII CICLO

MARIO URSO

NOVEL NI-BASED NANOSTRUCTURES:
SYNTHESIS AND APPLICATION IN SENSING
AND ENERGY STORAGE

TUTOR: PROF. FRANCESCO PRIOLO

PROF. SALVO MIRABELLA

COORDINATORE: PROF.SSA MARIA GRAZIA GRIMALDI

TESI PER IL CONSEGUIMENTO DEL TITOLO

To my family

Cover

False coloured plan-view SEM image of Ni-based nanowalls obtained by chemical bath deposition method. More details can be found within the Contents of this thesis.

**Novel Ni-based Nanostructures: Synthesis and Application
in Sensing and Energy Storage**

Mario Urso

Ph.D. Thesis

**Ph.D. in Materials Science and Nanotechnologies (XXXII
cycle), University of Catania**

Printed in Catania, November 2019

“The Impossible Dream (The Quest)”

*To dream the impossible dream
To fight the unbeatable foe
To bear with unbearable sorrow
To run where the brave dare not go*

*To right the unrightable wrong
To love pure and chaste from afar
To try when your arms are too weary
To reach the unreachable star*

*This is my quest, to follow that star
No matter how hopeless, no matter how far
To fight for the right
Without question or pause
To be willing to march
Into hell for a heavenly cause*

*And I know if I'll only be true
To this glorious quest
That my heart will lay peaceful and calm
When I'm laid to my rest*

*And the world will be better for this
That one man scorned and covered with scars
Still strove with his last ounce of courage
To fight the unbeatable foe
To reach the unreachable star*

Song by Mitch Leigh, with lyrics written by Joe Darion. It was first sung in the 1972 movie “Man of La Mancha” by Don Quixote as he stands vigil over his armor, in response to Aldonza (Dulcinea)’s question about what he means by “following the quest”.

Contents

Preface	11
1 Introduction to nickel hydroxide and oxide nanostructures	15
1.1 Metal oxides nanostructures and their applications . . .	16
1.2 Nickel (oxy)hydroxide and oxide: structure, properties and synthesis	20
1.2.1 Nickel (oxy)hydroxide	20
1.2.2 Nickel oxide	25
1.2.3 Synthesis methods	27
1.3 Nickel hydroxide and oxide thin films grown by chemical bath deposition	33
1.3.1 Historical overview	33
1.3.2 Film formation and growth	37
1.3.3 Film growth kinetics	41
1.4 Conclusions	43
References	43
2 Ni-based nanowalls for non-enzymatic glucose sensing	51
2.1 Non-enzymatic glucose sensing	52
2.2 Materials and methods	57
2.2.1 Synthesis	57
2.2.2 Characterization	58
2.3 Ni-based nanowalls	59

2.3.1	Morphological, structural and chemical characterization	59
2.3.2	Growth model	67
2.3.3	Electrochemical properties	72
2.3.4	Glucose detection performances	74
2.4	Conclusions	79
	References	80
3	Au decorated NiO nanowalls for PCR-free Mycoplasma agalactiae sensing	83
3.1	Contagious Agalactia	84
3.2	Materials and methods	89
3.2.1	Synthesis	89
3.2.2	Characterization	91
3.3	Au decorated NiO nanowalls	92
3.3.1	Morphological and chemical characterization	92
3.3.2	Mycoplasma agalactiae DNA sensing	94
3.4	Conclusions	99
	References	100
4	NiO nanostructures for gas sensing	105
4.1	The need of gas sensors	107
4.2	Materials and methods	109
4.2.1	Synthesis	109
4.2.2	Characterization	110
4.3	Acetone sensor based on NiO nanowalls	110
4.3.1	Overview of acetone sensors based on NiO	110
4.3.2	Morphological and electrical characterization	112
4.3.3	Acetone sensing performances	113
4.4	NO ₂ sensor based on nanoporous NiO film	118
4.4.1	Overview of NO ₂ sensors based on NiO	118
4.4.2	Morphological and electrical characterization	120
4.4.3	NO ₂ sensing performances	121
4.4.4	NO ₂ sensing mechanism	132

4.5	Conclusions	136
	References	137
5	Ni(OH)₂@Ni core-shell nanochains for energy storage applications	145
5.1	Hybrid supercapacitors	147
5.2	Materials and methods	152
5.2.1	Synthesis	152
5.2.2	Characterization	153
5.3	Ni(OH) ₂ @Ni core-shell nanochains	153
5.3.1	Morphological, structural and chemical characterization	153
5.3.2	Energy storage performances	160
5.3.3	Energy storage mechanism	169
5.4	Conclusions	175
	References	175
	Conclusions and perspectives	181
	Appendix	185
	Curriculum Vitae	209
	List of Publications	217
	Acknowledgments	221

Preface

Nanotechnology is a field related to materials and devices with characteristic dimensions in the nanometer scale where unique size, shape and structure-dependent physical and chemical properties emerge, opening new opportunities in science and technology. Among the various nanostructured materials, metal oxide nanostructures and, specifically, nickel hydroxide $[\text{Ni}(\text{OH})_2]$ and nickel oxide (NiO) nanostructures have recently attracted increasing attentions due to their excellent performances in many applications, such as electrochromic smart windows, electrochemical (bio)sensing, gas sensing, energy storage and water splitting. $\text{Ni}(\text{OH})_2$ and NiO nanostructures can be prepared by various methods. However, some of them require expensive or complex experimental setup which can not be used for large scale production. Therefore, in the last decades researchers have devoted many efforts in developing simple, low-cost and scalable synthesis methods of $\text{Ni}(\text{OH})_2$ and NiO nanostructures. Among them, the chemical bath deposition (CBD) is considered the most advantageous one. In fact, CBD involves the simple immersion of substrates into an aqueous solution of $\text{Ni}(\text{OH})_2$ precursors which allows to deposit nanostructured Ni-based thin films, named “nanowalls”, with high surface-to-volume ratio and porous structure. Since the pioneering NiO CBD by Pramanik and Battacharya in 1990, CBD has been widely used to prepare Ni-based nanowalls. Still, as a solution-based method, CBD lacks of a good control and reproducibility. To overcome these limitations, CBD needs to be fully investigated and controlled. In this thesis, a careful analysis of the most important

CBD parameters (reagents, deposition time and temperature) is conducted, leading to a better control and reproducibility of the method. Moreover, a growth model for Ni-based nanowalls is proposed. The full comprehension of Ni-based nanowalls growth allows to enhance their electrochemical properties. To further improve the electrical and electrochemical properties of Ni-based nanowalls for specific applications, several strategies are presented, including thermal annealing and/or electrochemical processes, or decoration with metals by electroless deposition method. In this way, novel Ni-based nanostructures, such as Ni nanofoam, Au decorated NiO nanowalls, nanoporous NiO film and Ni(OH)₂@Ni core-shell nanochains, are obtained, showing excellent performances for various applications, including non-enzymatic glucose sensing, PCR-free DNA sensing, acetone and NO₂ sensing, and energy storage.

The thesis is organized as follows:

- the first chapter is an introduction to nickel hydroxide and oxide nanostructures. The fundamental properties and fabrication methods of Ni(OH)₂ and NiO nanostructures are first presented. Then, a literature overview of Ni(OH)₂ and NiO thin films grown by low-cost CBD is reported, focusing on the proposed models for film formation and growth;
- the second chapter concerns the careful investigation of the most important CBD parameters, which leads to a new model for film formation and growth. The morphological, structural and electrochemical properties of Ni-based nanowalls are also presented. The optimized Ni-based nanowalls were transformed into the novel Ni nanofoam by a thermal annealing process in reducing atmosphere and applied for non-enzymatic glucose sensing, showing remarkable performances in terms of high sensitivity, selectivity, stability and low limit of detection (LoD);
- the third chapter reports an introduction to Contagious Agalactia (CA), an infectious disease which reduces the milk production in goats and sheep, caused by the bacterium *Mycoplasma*

agalactiae (Ma). To provide a cost and time-saving diagnosis method for CA other than conventional PCR-based approach, a novel impedimetric Ma DNA sensor is presented. The sensor consists of Au decorated NiO nanowalls obtained by gold electroless deposition onto NiO nanowalls, which were functionalised with Ma probe ssDNA and used to sense the hybridization with Ma complementary ssDNA;

- the fourth chapter introduces the urgent need for low-cost sensors of acetone and NO₂. Then, the acetone sensing performances of NiO nanowalls are presented. Moreover, a novel nanoporous NiO film with impressive sensitivity, selectivity, stability and low LoD to NO₂ at room temperature is presented. A model for the NO₂-NiO interaction mechanism is also proposed;
- the fifth chapter reports an introduction to nanostructures for hybrid supercapacitors. Then, novel Ni(OH)₂@Ni core-shell nanochains, prepared by CBD, thermal annealing and electrochemical oxidation, are presented. Due to this unique core-shell architecture, high-rate energy storage performances in terms of superior specific capacity, rate capability and stability are obtained.

Chapter 1

Introduction to nickel hydroxide and oxide nanostructures

Contents

1.1	Metal oxides nanostructures and their applications	16
1.2	Nickel (oxy)hydroxide and oxide: structure, properties and synthesis	20
1.2.1	Nickel (oxy)hydroxide	20
1.2.2	Nickel oxide	25
1.2.3	Synthesis methods	27
1.3	Nickel hydroxide and oxide thin films grown by chemical bath deposition . .	33
1.3.1	Historical overview	33
1.3.2	Film formation and growth	37
1.3.3	Film growth kinetics	41
1.4	Conclusions	43

This chapter is focused on nickel hydroxide [Ni(OH)₂] and oxide (NiO) nanostructures, that have recently emerged as important materials in many applications, including sensing and energy storage. First, the crystal structure and general properties of these materials are described. Then, a large number of common methods to synthesize Ni(OH)₂ and NiO nanostructures are presented. Finally, the chemical bath deposition (CBD) of Ni(OH)₂ and NiO thin films is reviewed.

1.1 Metal oxides nanostructures and their applications

Nanotechnology opened new opportunities in almost every scientific field due to the enhancement of physical and chemical properties of nanoscale materials at their unique size and shape. Among them, metal oxides nanostructures are considered to be one of the most fascinating research topic, playing a vital role in physics, chemistry, materials science and biotechnology. Figure 1.1 reports a collection of ZnO nanostructures, one of the most investigated metal oxides.

The various metallic elements can form a wide variety of oxides, such as ZnO, NiO, SnO₂, In₂O₃, CuO, Co₃O₄, MoO₃, WO₃, IrO₂, Fe₂O₃, TiO₂, V₂O₅ and RuO₂. The *d*-shells of transition metal oxides are partially filled, while the *s*-shells are always fully filled by electrons, determining their typical semiconducting behaviour with wide bandgaps and high dielectric constants [1.2].

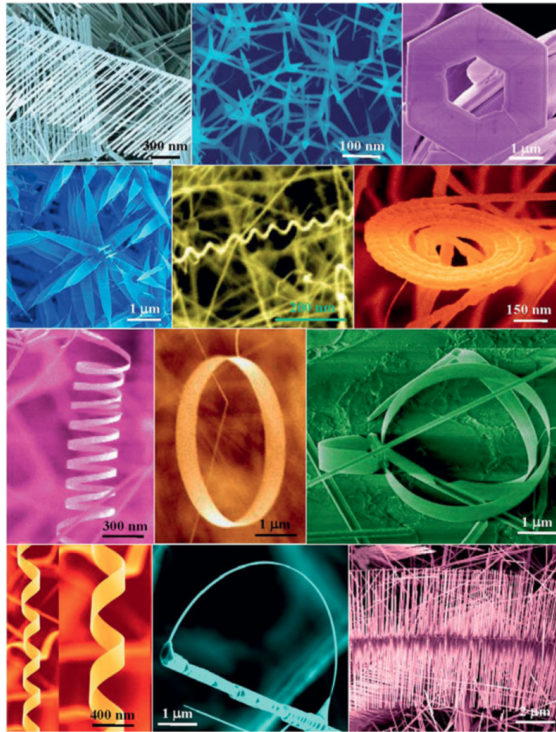


Figure 1.1: A collection of ZnO nanostructures, among which nanosprings, nanorings, nanobows and nanohelices [1.1].

Metal oxide nanostructures, having at least one dimension between 1 and 100 nm, can be classified as 0-D, 1-D and 2-D (Figure 1.2) [1.3]. Quantum wells (thin films) are 2-D nanostructures, where charges are confined only in one dimension and free to move in the remaining two dimensions. Quantum wires (nanowires, nanorods) are 1-D nanostructures, where charges are confined in two dimensions and free to move in the third dimension. Quantum dots (nanoparticles) are 0-D nanostructures, where charges are confined in all directions. Due to charges confinement in metal oxide nanostructures, the density of energy states is no longer continuous like bulk counterparts, but discrete, enabling new and enhanced properties. As a results, a

wide variety of metal oxides nanostructures with peculiar morphologies and properties have been developed, showing potential in many applications, such as sensing ((bio)molecules, heavy metals, pH, UV photons, gases, etc.), energy storage (batteries, supercapacitors, fuel cells), solar cells, energy harvesting (photovoltaic, piezoelectric, pyroelectric, thermoelectric, etc.), water splitting, water remediation, optics (LEDs, lasers, waveguides, etc.), microelectronics (transistors, memories, etc.) and so on [1.2].

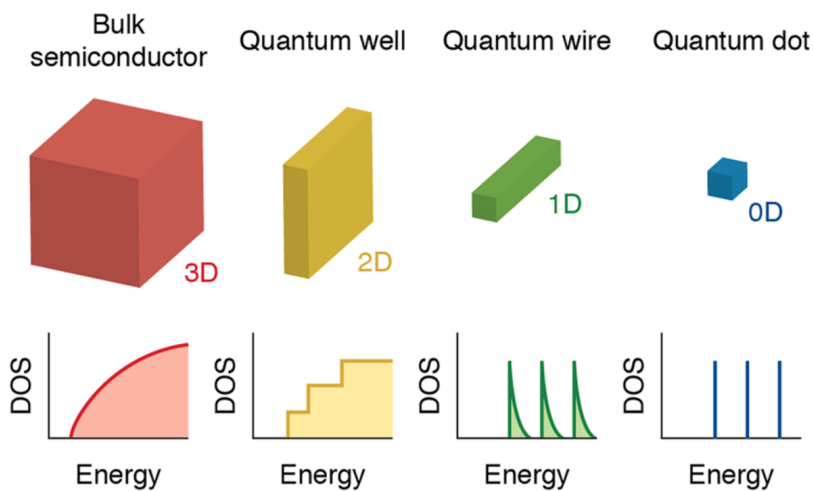


Figure 1.2: Schematic illustration of a bulk semiconductor and semiconductor nanostructures with reduced dimensionality, such as quantum well (thin film), quantum wire (nanowire, nanorod), quantum dot (nanoparticle), with the corresponding density of energy states (DOS) [1.3].

Nanostructured materials can be obtained by various synthesis methods, which are broadly classified as top-down or bottom-up (Figure 1.3) [1.4]. The top-down approach involves the orderly elimination of material from larger or bulk solids until nanostructures are obtained. Contrarily, in the bottom-up approach, nanostructures are built through self-assembling of ions, atoms or molecules.

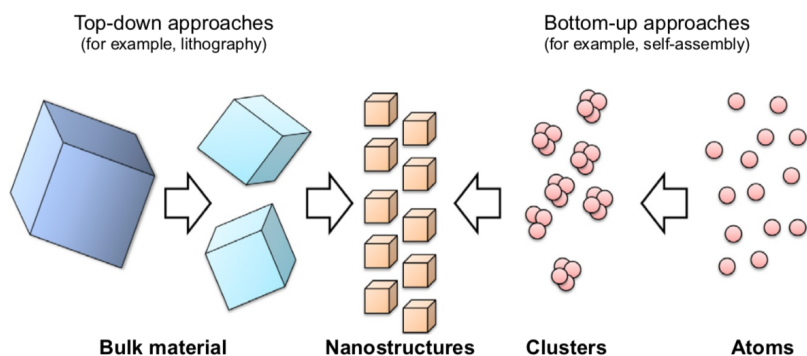


Figure 1.3: Schematic illustration of the top-down and bottom up approaches to obtain nanostructures [1.4].

The synthesis method of nanostructures represents a critical issue for practical applications. In fact, although several prototypes based on metal oxide nanostructures with outstanding performances have been reported, only few of them have been successfully transferred to commercial products due to their complex, costly and unreproducible fabrication. Therefore, simple, low-cost, reproducible, large-area and scalable synthesis methods are required to allow practical applications.

Among the various metal oxide nanostructures, $\text{Ni}(\text{OH})_2$ and NiO have recently emerged due to their excellent performances in many applications, such as sensing, energy storage and water splitting [1.5–8]. Moreover Ni is an abundant element in Earth (Figure 1.4) and, compared to the other metal oxides, $\text{Ni}(\text{OH})_2$ and NiO nanostructures with tunable properties can be synthesized by simple, low-cost, large area and scalable methods, which are particularly attracting for both academy and industries.

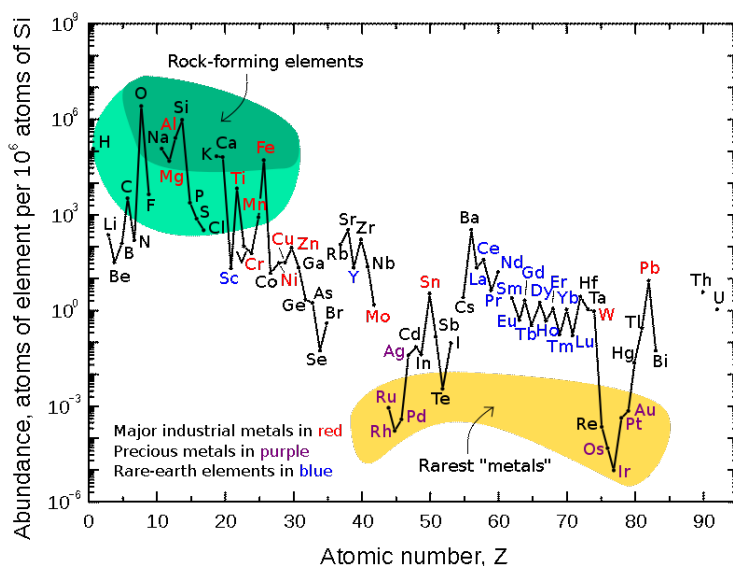


Figure 1.4: Abundance (atom fraction) of the chemical elements in Earth's upper continental crust as a function of atomic number [1.9].

In the following section, the structure, properties and common synthesis methods of $\text{Ni}(\text{OH})_2$ and NiO nanostructures are presented.

1.2 Nickel (oxy)hydroxide and oxide: structure, properties and synthesis

1.2.1 Nickel (oxy)hydroxide

In 1966, Bode et al. identified two polymorphs of $\text{Ni}(\text{OH})_2$, indicated as α and β [1.10]. β - $\text{Ni}(\text{OH})_2$ adopts a hexagonal close-packed structure of Ni^{2+} and OH^- ions, which is isostructural to brucite and naturally occurs as the mineral theophrastite (Figure 1.5) [1.5].

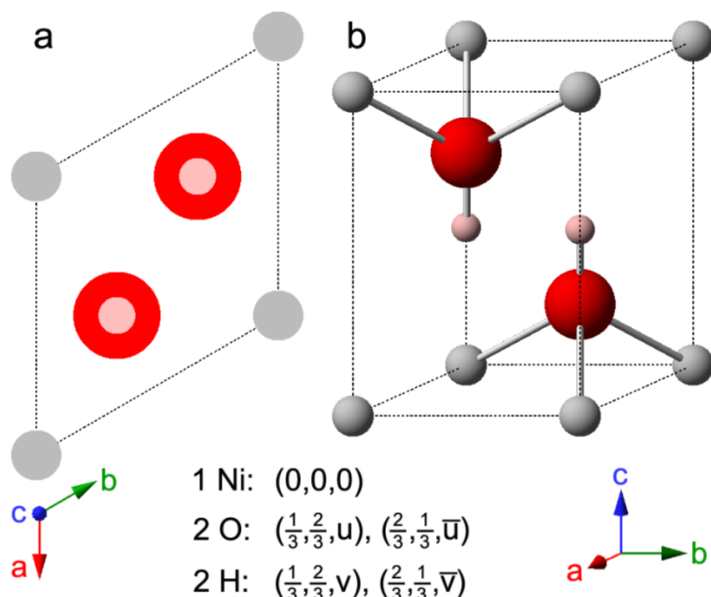


Figure 1.5: Crystal structure of β -Ni(OH)₂: (a) unit cell projection and (b) ball-and-stick unit cell ($u = 0.24$ and $v = 0.47$, or $u = 0.2221$ and $v = 0.4275$). Grey = Ni²⁺, red = O²⁻, pink = H⁺ [1.11].

α -Ni(OH)₂ consists of layers of β -Ni(OH)₂ intercalated by water molecules and cations (NO³⁻, CO₃²⁻, SO₄²⁻, Cl⁻, etc.), therefore is often denoted as α -Ni(OH)₂·xH₂O where x is the degree of hydration (typically, $0.41 \leq x \leq 0.7$) [1.5, 12]. The crystal structure of α -Ni(OH)₂ is illustrated in Figure 1.6, where intercalated water molecules appear to be fixed. Actually, it has been demonstrated that they have some freedom to rotate and translate within the ab plane, acting as a sort of “amorphous glue” that holds the β -Ni(OH)₂ layers together.

Ni(OH)₂ electrodes can be electrochemically oxidized (charge process) into nickel oxyhydroxide (NiOOH) and reduced back (discharge

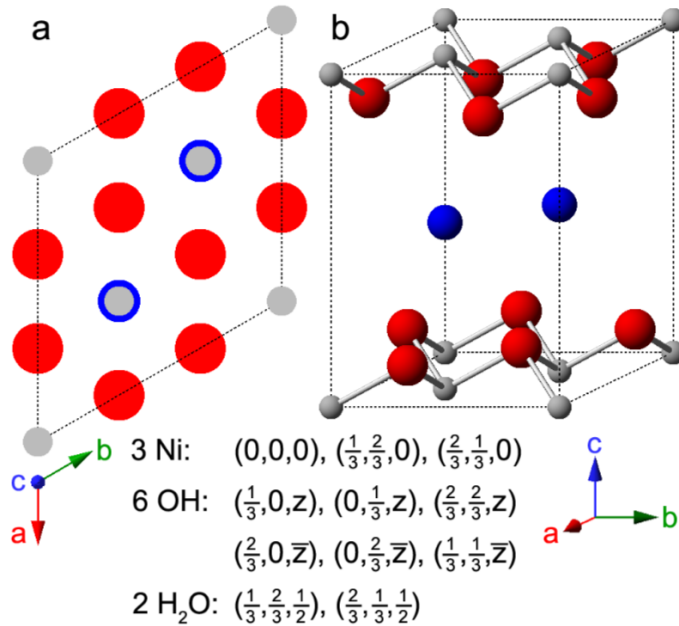
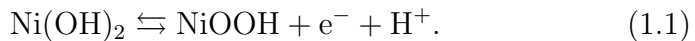


Figure 1.6: Crystal structure of α -Ni(OH)₂·xH₂O: (a) unit cell projection and (b) ball-and-stick unit cell for $x = 0.67$ (typically, $0.41 \leq x \leq 0.7$). Grey = Ni²⁺, red = OH⁻, blue = H₂O [1.11].

process) to Ni(OH)₂, as follows [1.13]:



NiOOH is a non-stoichiometric compound whose structure resembles that of Ni(OH)₂ with half as many hydrogen atoms. There are two phases of NiOOH, known as γ and β , associated to α and β -Ni(OH)₂, respectively. It is worth noting that the distance between NiOOH layers in γ -NiOOH (7 Å) is larger than β -NiOOH (4.85 Å), due to the intercalated water molecules and cations (Li⁺, Na⁺, K⁺, etc.) [1.12, 14]. This difference leads to a higher oxidation state in γ -NiOOH rather than β -NiOOH (3.5-3.67 versus 3) [1.15, 16]. As a consequence, the oxidation reaction to γ -NiOOH occurs at a lower

potential than β -NiOOH, resulting in a higher specific capacity (462-480 versus 289 mAh g⁻¹) [1.12, 14].

Bode et al. proposed a simple scheme (Figure 1.7) to explain the electrochemical oxidation and reduction processes involving the two phases of Ni(OH)₂ and NiOOH [1.10]. Although the complete picture could be more complicated, this scheme represents a good overall description of the processes that occur at Ni(OH)₂ electrodes, which are extensively described below.

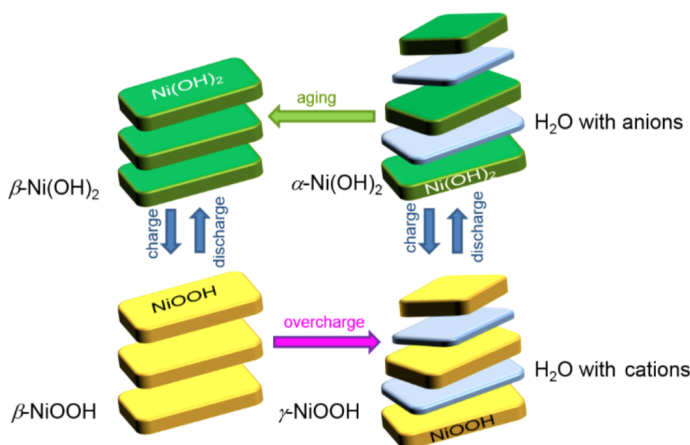


Figure 1.7: Bode's scheme illustrating the electrochemical processes between the various phases of Ni(OH)₂ and NiOOH [1.12].

Only a small variation of Ni(OH)₂ and NiOOH unit cell parameters has been observed after β -Ni(OH)₂ \rightleftharpoons β -NiOOH and α -Ni(OH)₂ \rightleftharpoons γ -NiOOH reactions [1.14]. However, internal mechanical stress occurs during the redox cycling because of the different density of Ni(OH)₂ and NiOOH [1.5].

High charge rates and prolonged overcharging of β -Ni(OH)₂ in KOH could favour the formation of γ -NiOOH [1.14]. The direct oxidation reaction β -Ni(OH)₂ \rightarrow γ -NiOOH has not been observed yet. In fact, while β -Ni(OH)₂ \rightleftharpoons β -NiOOH only implies the removal of

one proton and one electron, with no other structural changes except a slight variation of cell parameters, the oxidation to γ -NiOOH requires the intercalation of water molecules, the exchange of protons and alkali ions, and a layer movement [1.14]. Therefore, the energy barrier to form γ -NiOOH is higher than β -NiOOH. As a result, first β -Ni(OH)₂ \rightarrow β -NiOOH occurs, then γ -NiOOH is obtained by overcharging. Nevertheless, the reduction process γ -NiOOH \rightarrow β -Ni(OH)₂ is allowed.

α -Ni(OH)₂ spontaneously transforms into β -Ni(OH)₂ through prolonged redox cycling in alkaline solutions. This phenomenon, which has been widely observed in the field of rechargeable battery anodes, is typically referred to as “ageing” [1.5].

Using density functional theory, Hermet et al. predicted that β -Ni(OH)₂ is a semiconductor with a direct bandgap of ~ 2.9 eV, which is in agreement with the experimental value that they obtained from UV–Vis absorption spectrum, lying in the range $3.0 \div 3.5$ eV [1.17].

Hermet et al. studied also the dielectric response of β -Ni(OH)₂ [1.17]. The experiments were performed on an disc-shaped pellet made from pressed β -Ni(OH)₂ powder with gold electrodes in the frequency range $1 \div 10^6$ Hz and temperature range $150 \div 298$ K. A dielectric constant of 4.1 was obtained at 10^6 Hz and 150 K, while a value of 5.96 was expected by theoretical calculations. Hermet et al. have also calculated the two components of the dielectric permittivity tensor ϵ^∞ , which is related to the second derivative of the electronic energy with respect to an applied electric field, by using a linear response formalism. Then, the corresponding refractive indices of $n_\perp = 1.88$ and $n_\parallel = 1.82$ were obtained.

The electrical conductivity of Ni(OH)₂ electrode materials is an useful tool to evaluate their potential in energy storage applications [1.5]. The first measurements were carried out by Motori et al., who found that uncycled α -Ni(OH)₂ exhibited a low conductivity that ranged from 10^{-13} to 10^{-17} S cm⁻¹ depending on the temperature (298–423 K) and time (1–120 min) after the application of a step voltage [1.18]. Such a low conductivity was attributed to the ionic

conduction. After redox cycling, β -Ni(OH)₂ was obtained by ageing, showing higher conductivity than α phase. Moreover, the absorption of water in uncycled α -Ni(OH)₂ and cycled β -Ni(OH)₂ electrodes resulted in a very strong increase in the electrical conductivity of 10⁻⁴ S cm⁻¹ at 2% absorbed water content and 1 min after voltage application, which is consistent with the idea that some water inside the structure is necessary to activate these materials. Palencsaár and Scherson also observed that the conductivity of a Ni(OH)₂ microparticle (30 μ m in size) immersed in 9 M KOH, increased by a factor of \sim 50 upon oxidation to NiOOH [1.19].

1.2.2 Nickel oxide

NiO shows the same crystal structure of NaCl, having octahedral Ni²⁺ and O²⁻ ions (Figure 1.8) [1.20]. It can be found in nature as the rare mineral bunsenite. Stoichiometric NiO appears as a green powder. Also, as a binary metal oxide, NiO could be non-stoichiometric, appearing as a black powder.

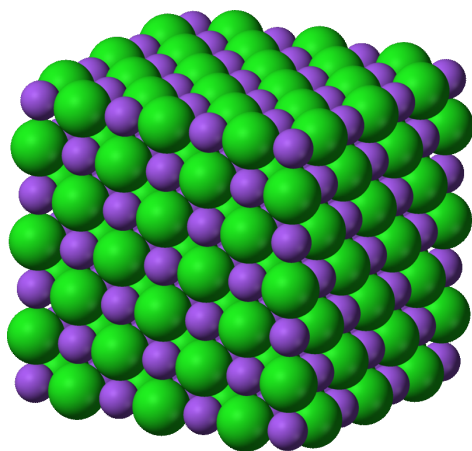
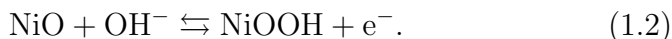


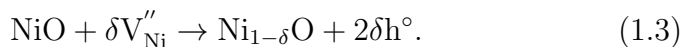
Figure 1.8: Crystal structure of NiO [1.20].

In alkaline solutions, NiO electrodes can be oxidized to NiOOH

and reduced back to NiO, as follows [1.6]:



NiO is a *p*-type semiconductor, with holes as the main carriers due to the vacancies of Ni in the crystal structure ($\text{Ni}_{1-\delta}\text{O}$) [1.21]:



Based on UV-Vis absorption spectra, a wide bandgap between 3.3 and 4.0 eV has been reported for NiO [1.22]. Moreover, Spear and Tannhauser prepared undoped NiO crystals by epitaxial deposition and measured a hole mobility of 20-50 $\text{cm}^2 \text{V}^{-1} \text{s}$ at room temperature [1.23], while Morin prepared various NiO samples by thermal decomposition of Ni precursors and measured a hole mobility of 0.1 $\text{cm}^2 \text{V}^{-1} \text{s}$ at 1000 K for all samples [1.24].

Rao et Smakula measured the dielectric constant of NiO crystals in the frequency range $10^2 \div 10^{10}$ Hz and temperature range $-273 \div 400^\circ\text{C}$ [1.25]. The dielectric constant increased exponentially with temperature, being 9.1 at 0 K and all frequencies, and 11.9 at 25°C in the frequency range $10^6 \div 10^{10}$ Hz.

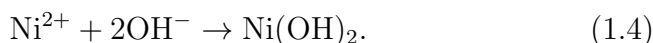
Stoichiometric NiO powders showed an electrical conductivity of $\sim 10^{-14} \text{ S cm}^{-1}$, which increased with non-stoichiometry, either due to a deficiency of Ni or an addition of Li, up to $10^{-7} \div 10^{-1} \text{ S cm}^{-1}$ [1.25]. Jlassi et al. reported NiO thin films by spray pyrolysis technique where the electrical conductivity varied from 10^{-1} to $1.7 \times 10^{-2} \text{ S cm}^{-1}$ by increasing film thickness from 240 to 620 nm [1.26].

Furthermore, NiO showed also electrochromism, i.e. the ability to change its optical properties (colour) by applying a voltage. This phenomenon has potential for the development of smart windows that increase the energy efficiency of building (for example by regulating the amount of energy entering through the window so that the need for air conditioning becomes lower) [1.27]. In particular, NiO is one of the most attractive electrochromic materials due to its high electrochromic efficiency, large dynamic range, good reversibility, and low-cost [1.28].

1.2.3 Synthesis methods

Several methods to synthesize Ni(OH)_2 and NiO materials with desired phase and morphology have been reported [1.5]. Typically, Ni(OH)_2 is deposited by bottom-up chemical methods. Then, NiO is obtained by thermal annealing of Ni(OH)_2 . NiO can be also directly obtained by bottom-up physical methods, which are less common in literature. Therefore, in the following pages, the synthesis methods of Ni(OH)_2 are first presented.

Ni(OH)_2 can be prepared by chemical precipitation (Figure 1.9(a)). Generally, a basic solution (NaOH , NH_3 , etc.) is added to a Ni^{2+} salt solution ($\text{Ni(NO}_3)_2$, NiCl_2 , etc.) or vice versa. Then, at sufficiently high pH, OH^- concentration exceeds the solubility limit and Ni(OH)_2 precipitates [1.5]:



The crystalline phase and morphology of Ni(OH)_2 are determined by the preparing conditions (precursors and their concentration, time, temperature and pH). For example, the precipitation at room temperature favours the formation of α - Ni(OH)_2 , while the precipitation at higher temperatures produces mixed-phase α/β or pure β - Ni(OH)_2 materials [1.29]. The challenge with this method is to precisely control the morphology and properties of Ni(OH)_2 due to its fast precipitation [1.6].

Chemical bath deposition (CBD) is similar to the chemical precipitation, and is considered to be the most advantageous method to synthesize Ni(OH)_2 and NiO thin films. It will be exhaustively discussed in the next section of this chapter.

The electrochemical precipitation method is based on electrochemical redox reactions which allow to deposit Ni(OH)_2 onto conductive substrates (Figure 1.9(b)). Typically, the substrates are placed in a Ni^{2+} salt solution and kept at a negative potential which

leads to a cathodic current from the reduction of water:



Then, reaction 1.4 occurs and $\text{Ni}(\text{OH})_2$ precipitates onto the surface of the substrate due to its low solubility [1.5]. The phase and morphology of $\text{Ni}(\text{OH})_2$ are determined by Ni salt counterion and concentration, pH and temperature of the solution, cathodic current and substrate. Typically, deposition currents of a few mA cm^{-2} yield α - $\text{Ni}(\text{OH})_2$, while larger currents produce the mixed-phase α/β [1.30, 31]. Although the electrochemical precipitation is a simple method to uniformly deposit $\text{Ni}(\text{OH})_2$, its small-scale production and the requirement of conductive substrates limit its use for practical applications [1.6].

The sol-gel is a simple and cheap synthesis method, which can be defined as the conversion of a precursor solution into an inorganic solid by a chemical route [1.6]. It always begins with the preparation of a sol, i.e. a colloidal suspension of very small particles (1 nm to 1 μm) through a surfactant, followed by a treatment of the sol to prepare a gel, i.e. an integrated network of discrete particles or polymers. For example, a $\text{Ni}(\text{OH})_2$ sol can be prepared from chemically precipitated powder by repeatedly washing it with water, while a gel can be further obtained by centrifuging the sol, forming arrays of discrete $\text{Ni}(\text{OH})_2$ colloidal particles (Figure 1.9(c)). In this method, surfactants, solvents, time and temperature are the main factors to tune the properties of the resulting materials.

Chemical ageing, the spontaneous α - $\text{Ni}(\text{OH})_2 \rightarrow \beta$ - $\text{Ni}(\text{OH})_2$ transformation in alkaline solutions, is also considered a β - $\text{Ni}(\text{OH})_2$ synthesis method (Figure 1.9(d)). It has been reported that this process is favoured at high temperatures (e.g. 70-80°C) in concentrated alkaline media (e.g. 5 M KOH) [1.5].

Hydrothermal and solvothermal methods are very similar, except for the solution being aqueous or non-aqueous, respectively. In a typical process (Figure 1.9(e)), precursors and solvent are placed in a pressure vessel (autoclave) and then heated above the boiling point

of water (typically, 150-200°C for $\text{Ni}(\text{OH})_2$). The vessel could be big enough to make hydrothermal and solvothermal methods useful for large-scale production, however its volume is fixed. Therefore, as the solution is heated, the pressure and boiling point increase. The solution remains liquid at such high temperatures that precursors fully dissolve. Then, the temperature is decreased, and $\text{Ni}(\text{OH})_2$ precipitates. Generally, β - $\text{Ni}(\text{OH})_2$ is formed at the high temperatures used in hydrothermal and solvothermal syntheses. However, it is possible to produce α - $\text{Ni}(\text{OH})_2$ materials, for example by introducing an intercalating agent into the reaction mixture, as reported by Dixit et al. [1.32].

Medway et al. showed that on first immersion of a single crystal Ni electrode in a KOH solution, a bilayer, i.e. $\text{Ni}(\text{OH})_2$ layer underlaid by a NiO layer, was formed on Ni surface (Figure 1.9(f)) [1.33]. Prolonged redox cycling increased the thickness of both $\text{Ni}(\text{OH})_2/\text{NiOOH}$ and NiO layers, due to the reaction between OH^- and Ni^{2+} ions and between O^{2-} and Ni^{2+} ions, respectively. After a number of redox cycles, the $\text{Ni}(\text{OH})_2/\text{NiOOH}$ layer growth was stopped as the compact NiO layer thickened. The final thickness of the $\text{Ni}(\text{OH})_2/\text{NiOOH}$ layer was ~ 5 nm. Later on, this method has been used to synthesize $\text{Ni}(\text{OH})_2$ on nanostructured Ni electrodes, often referred to as “electrochemical oxidation” [1.34].

Figure 1.10 reports the images of $\text{Ni}(\text{OH})_2$ samples prepared by the above mentioned methods, including (a) α - $\text{Ni}(\text{OH})_2$ film by chemical precipitation [1.35], (b) “nanoflower” composed of nanosheets by hydrothermal method [1.36], (c) “dandelion-like” hollow β - $\text{Ni}(\text{OH})_2$ microsphere by sol-gel method [1.37], (d) an “unusually” large β - $\text{Ni}(\text{OH})_2$ “pseudo-single crystal” by chemical precipitation [1.38], (e) α - $\text{Ni}(\text{OH})_2$ “nanoribbons” by hydrothermal method [1.39] and (f) β - $\text{Ni}(\text{OH})_2$ “nanoflowers” by microwave assisted hydrothermal method [1.40].

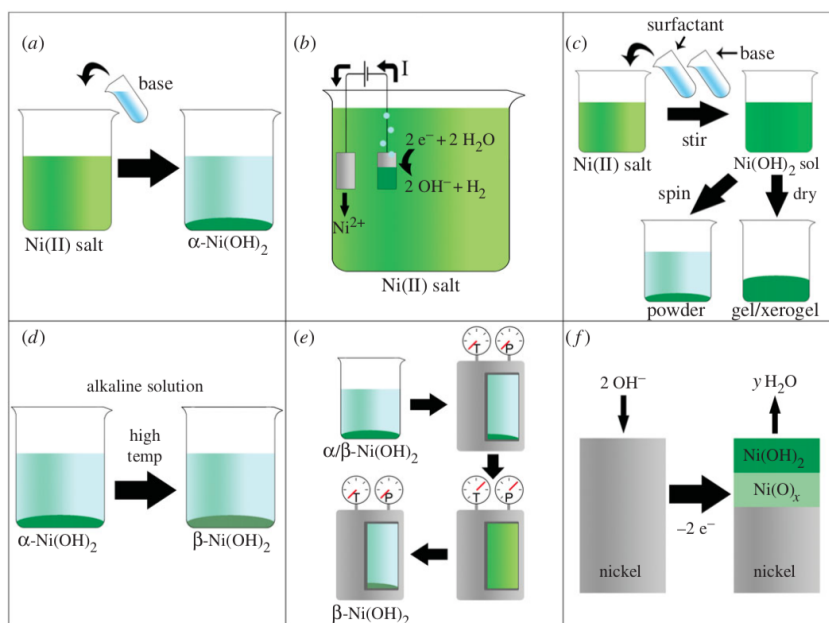


Figure 1.9: A collection of methods to prepare Ni(OH)₂. (a) Chemical precipitation: an aqueous solution of Ni²⁺ salt is basified, leading to supersaturation and Ni(OH)₂ precipitation. (b) Electrochemical precipitation onto a conductive substrate: the reduction of water produces OH⁻ ions at the cathode surface, which react with Ni²⁺ ions in solution. (c) Sol-gel methods: a solution of Ni²⁺ salt and a surfactant is basified to form a Ni(OH)₂ sol. The sol is treated (e.g. by centrifugation or drying) to produce a gel. (d) Chemical ageing: conversion of α-Ni(OH)₂ into β-Ni(OH)₂ in concentrated alkaline media at high temperatures or, slowly, at room temperature. (e) Hydrothermal method: Ni(OH)₂ precursors are fully dissolved in a pressure vessel at high temperatures, then temperature is decreased and β-Ni(OH)₂ precipitates. (f) Electrochemical oxidation of Ni electrodes: α/β-Ni(OH)₂ layer is formed on Ni surface, often underlaid by a non-stoichiometric NiO layer [1.5, 11].

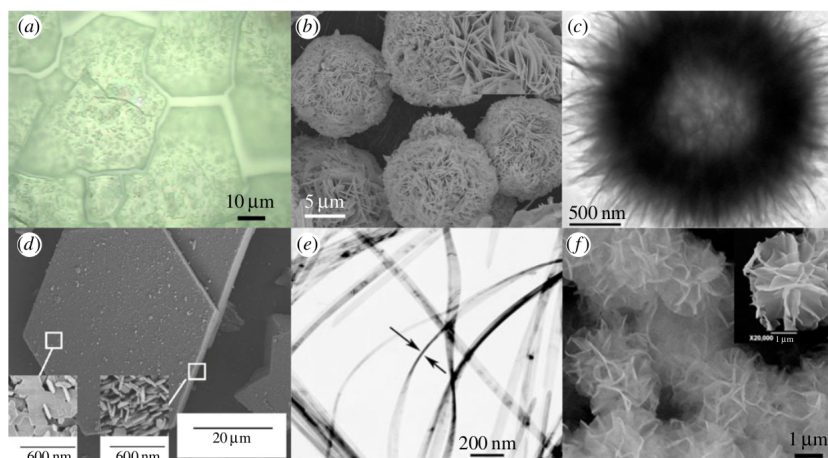


Figure 1.10: A collection of images of $\text{Ni}(\text{OH})_2$ samples prepared by various synthesis methods. (a) Light micrograph of an electrochemically precipitated $\alpha\text{-Ni}(\text{OH})_2$ film, cracked after drying [1.35]. (b) SEM image of $\beta\text{-Ni}(\text{OH})_2$ “nanoflowers” prepared by hydrothermal method (the inset is a high magnification image of a nanoflower, showing its nanosheets) [1.36]. (c) TEM image of a “dandelion-like” hollow $\beta\text{-Ni}(\text{OH})_2$ microsphere prepared by sol-gel method [1.37]. (d) SEM image of an “unusually” large $\beta\text{-Ni}(\text{OH})_2$ “pseudo-single crystal” prepared by chemical precipitation (insets are high magnification images of a particle basal plane and edge) [1.38]. (e) TEM image of $\alpha\text{-Ni}(\text{OH})_2$ “nanoribbons” (10-20 nm thick) prepared by hydrothermal method [1.39]. (f) SEM image of $\beta\text{-Ni}(\text{OH})_2$ “nanoflowers” prepared by microwave-assisted hydrothermal method (the inset is a high magnification image of a nanoflower) [1.5, 40].

Less common methods to synthesize $\text{Ni}(\text{OH})_2$ include microwave-assisted synthesis, sonochemical methods, electrophoretic deposition and spray pyrolysis. In the microwave-assisted synthesis, a microwave oven is used to heat a solution more homogeneously than conventional heating methods, producing nanoparticles with very uniform shape and narrow size distribution [1.5]. The sonochemical method is based on powerful ultrasound radiations (0.02-10 MHz) to drive $\text{Ni}(\text{OH})_2$ precipitation [1.5]. This method allows to obtain amorphous products, the insertion of nanoscale materials into mesoporous materials, the deposition of nanoparticles onto ceramic and polymeric surfaces, and the formation of proteinaceous micro and nanospheres. The electrophoretic deposition is based on charged powder particles, dispersed or suspended in a liquid medium, attracted and deposited onto a conductive substrate of opposite charge on application of a DC electric field [1.6]. By changing the deposition time and applied potential it is possible to tune the thickness and morphology of the deposited film. In spray pyrolysis a solution of the precursors is sprayed on a heated substrate, where they undergo thermal decomposition [1.20]. This method allows to easily control film thickness, density and porosity.

Concerning NiO preparation, typically it consists in a thermal annealing process of $\text{Ni}(\text{OH})_2$ materials synthesized by the above mentioned methods. Such a process has been performed for 1 h or more in air or inert atmosphere at 300-500°C [1.22, 36, 37, 41, 42]. It has been often reported that it preserves the morphology of $\text{Ni}(\text{OH})_2$ materials [1.22, 36, 41].

A few physical methods allow to directly obtain NiO, such as pulsed laser deposition, physical vapour deposition, molecular beam epitaxy, and magnetron sputtering [1.20]. However, these methods are considered expensive and thus are not frequently used.

1.3 Nickel hydroxide and oxide thin films grown by chemical bath deposition

1.3.1 Historical overview

CBD is one of the simplest and most effective methods to grow Ni(OH)₂ and NiO nanostructures. In fact, the only requirements for CBD are a vessel to contain a solution, typically an aqueous solution of precursors, and substrates on which the deposition is carried out [1.43]. Stirring and a thermostat that maintains a specific and constant temperature in the solution are often used. Compared to other methods, CBD offers different advantages. In particular, contrary to the hydrothermal method, CBD is performed at very low temperatures, and contrary to the electrochemical precipitation method, substrates for CBD can be either conductive or not. In addition, CBD is considered a low-cost method that is suitable for large-scale production. However, particular care is needed with the preparing conditions (reagents and their concentration, temperature, stirring, etc.) to ensure CBD effectiveness and reproducibility.

CBD of NiO thin films was reported for the very first time by Pramanik and Bhattacharya in 1990. A glass substrate was kept for 1 h in a solution of nickel sulfate (NiSO₄), potassium persulfate (K₂S₂O₈), ammonia (NH₃) and deionized water at room temperature [1.44]. In this way, a film was deposited onto the substrate, showing black appearance, 275 nm thickness, NiO polycrystalline nature, *p*-type semiconductive behaviour with 1.75 eV bandgap and $\sim 10^{-5}$ S cm⁻¹ electrical conductivity.

Since this pioneering work, several Ni(OH)₂ and NiO thin films were deposited by Pramanik's CBD, with the aim to understand and control their growth or to test them for various applications (Figure 1.11).

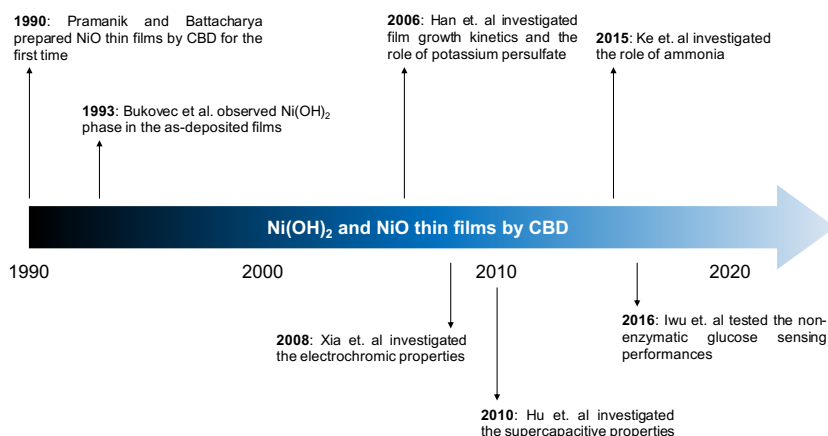


Figure 1.11: Temporal scale of research on Ni(OH)₂ and NiO thin films prepared by Pramanik’s CBD.

In 2006, Han et al. studied Pramanik’s CBD and reported the first SEM images of the as-deposited film (Figure 1.12) [1.22]. Han described film morphology as a uniform fine-grained, cellular-like structure with a final thickness of ~ 180 nm. Later on, this peculiar morphology has been referred to as “nanowalls”: an ideal 3D nanostructure with high surface-to-volume ratio composed of a tight network of nanosheets (10-20 nm thick) that are aligned on a substrate [1.45]. The morphology of nanowalls also occurs on the macroscale in nature, forming the inner structure of prickly pear pads (Figure 1.13).

Contrarily to Pramanik, the film deposited by Han contained Ni(OH)₂/NiOOH phase, while NiO phase was obtained only after a thermal annealing process for 1h in air at 500°C, which did not affect film morphology (Figure 1.12(a)) [1.22]. Also, a wide bandgap of 3.5 eV was estimated for the annealed film. Although this value is much larger than Pramanik’s one, it is in agreement with previous reports [1.47–52].

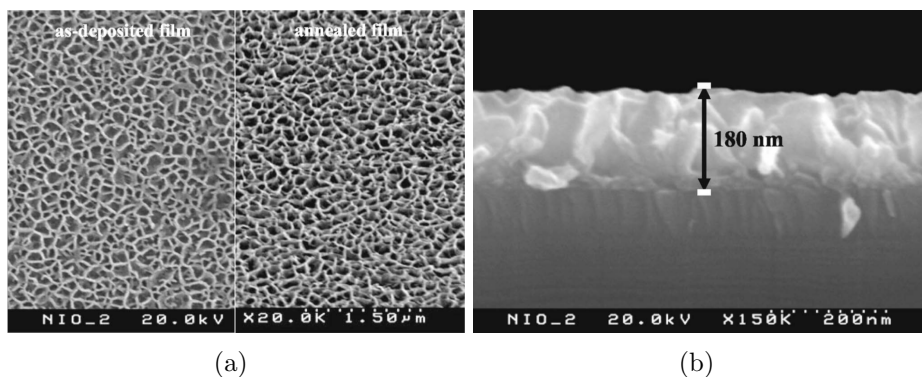


Figure 1.12: (a) SEM plan-view of the as-deposited film (left) and annealed film for 1 h in air at 500°C (right), and (b) SEM cross-sectional view of the as-deposited film on oxidized Si substrate [1.22].



Figure 1.13: (a) Prickly pear cactus, and (b) internal structure of its pads, resembling that of “nanowalls” [1.46].

In 2008, Xia et al. prepared NiO thin films on ITO glass substrates by CBD and thermal annealing in air at different temperatures (300, 350 and 400°C), studying their electrochromic properties [1.41]. Xia's NiO thin films were coloured by applying step voltages of 0.77 V (vs. Hg/HgO reference electrode) for coloration and 0 V for bleaching, which correspond respectively to the oxidation ($\text{NiO} + \text{OH}^- \rightarrow \text{NiOOH} + \text{e}^-$) and reduction ($\text{NiOOH} + \text{e}^- \rightarrow \text{NiO} + \text{OH}^-$) peak potentials of cyclic voltammetry curves recorded in 1 M KOH. NiO thin films colour changed from black in the coloured state to transparent in the bleached state (Figure 1.14(a)). The electrochromic efficiency increased with decreasing annealing temperature, leading to an impressive transmittance variation between coloured and bleached states (82% at 550 nm) for the NiO sample obtained at 300°C (Figure 1.14(a)).

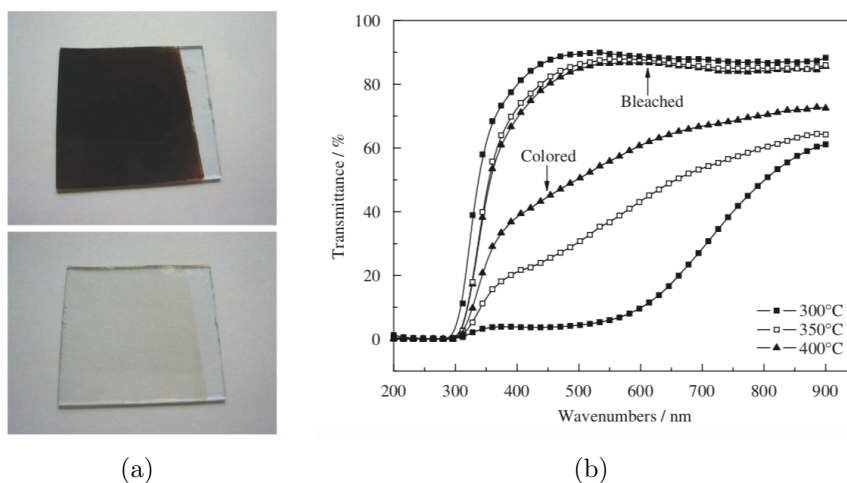


Figure 1.14: (a) Photographs of NiO thin films in the coloured (top) and bleached (bottom) states, and (b) optical transmittance spectra of NiO thin films annealed at different temperatures (300, 350 and 400°C) [1.41].

Since 2010, Ni-based nanostructures have attracted tremendous attention as supercapacitive electrode materials for energy storage applications. Due to its unique advantages, Pramanik's CBD has been widely used to deposit Ni(OH)₂ and NiO on various substrates, leading to remarkable energy storage performances [1.13, 15, 53–55]. Moreover, in 2016 Iwu et al. grew a Ni nanofoam by Pramanik's CBD and thermal annealing in reducing atmosphere, and applied it for non-enzymatic glucose sensing, demonstrating superior performances than other Ni(OH)₂ and NiO nanostructures reported in literature [1.42].

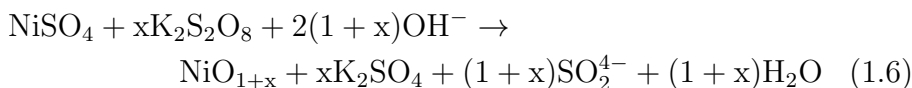
In all these applications areas, it is well known that the comprehension and prediction of crystal growth is a key element in improving the functionality of Ni(OH)₂ and NiO nanostructures [1.56]. This is particularly important in bottom-up approaches such as CBD, which are increasingly demanded for nanostructures production on a large scale at low cost [1.57]. Therefore, in the following part of this chapter, the models for film formation and growth kinetics by Pramanik's CBD are presented, while a review on sensing and energy storage applications of such films is reported in the following chapters.

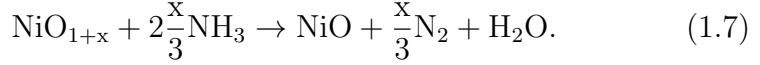
1.3.2 Film formation and growth

Film formation

Several attempts to describe the chemistry of film formation by Pramanik's CBD have been made, focusing on the role of a specific reagent: potassium persulfate and ammonia.

Initially, Pramanik proposed NiO phase formation via a two-step mechanism [1.44]:



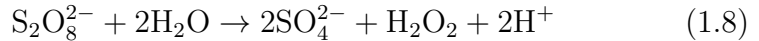


Reaction 1.6 involves NiO deposition where Ni has mixed valencies 2+ and 3+. Ni³⁺ is then reduced by ammonia to Ni²⁺ according to reaction 1.7.

Subsequently, Bukovec et al. performed XRD analysis of the as-deposited films, observing 4Ni(OH)₂·NiOOH·xH₂O mixed phase rather than NiO phase [1.58].

To clarify the role of potassium persulfate, Han et al. performed CBD with and without persulfate in solution [1.22]. No film formation was observed in the absence of persulfate. However, in both cases, particles formed by homogeneous nucleation in solution were found. XRD patterns of both types of particles were compatible with Ni(OH)₂·2H₂O or 4Ni(OH)₂·NiOOH·xH₂O phase, but the particles formed without persulfate showed worse crystallinity than those formed with persulfate. The as-deposited film with persulfate showed poor crystallinity and similar XRD pattern. Therefore, differently from what reported by Pramanik and in agreement with Bukovec, the as-deposited film did not contain NiO, which was further obtained by a thermal annealing process.

Based on the hydrolysis reaction suggested by Hodes et al. [1.59]



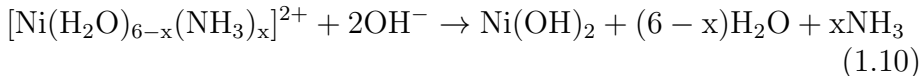
Han proposed the homogeneous nucleation and precipitation of Ni(OH)₂ nanoparticles in solution (reaction 1.4), which further react with S₂O₈²⁻ ions onto substrate surface through a molecular level heterogeneous reaction



This model explains why persulfate is necessary for film formation.

Later on, Xia et al. observed β-Ni(OH)₂ and γ-NiOOH phases by XRD analysis of the as-deposited film, attributing the divergence

from Han and Bukovec XRD results to the different preparing conditions (reaction time and temperature, ageing time, reagents concentrations) [1.41]. Therefore, Xia proposed a two-step model, where first Ni(OH)_2 is formed by the reaction of a nickel-water-ammonia complex with OH^- ions

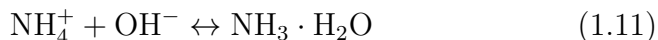


and then NiOOH is formed by reaction 1.9.

All these models attest the fundamental role of persulfate, which is required for film formation. Nevertheless, Pawar et al. demonstrated that at 80°C film formation occurs also in the absence of persulfate, despite the resulting film showed poorer electrical and electrochemical properties than film deposited with potassium persulfate under the same preparing conditions [1.60].

Concerning the role of ammonia, Ke et al. performed CBD onto TiO_2 nanowires using different ammonia concentrations (1.8, 2.4 and 3.4% NH_3 in H_2O) [1.13]. SEM analyses (Figure 1.15) revealed an increase of nanosheets thickness ($2 \rightarrow 23$ nm) with increasing NH_3 concentration (1.8 \rightarrow 3.4%). Moreover, differently from previous reports, XRD analyses indicated the presence of $\beta\text{-Ni(OH)}_2$ phase.

To explain these observations, Ke hypothesised that ammonia plays a dual role. One is that OH^- ions released by NH_3 molecules



react with Ni^{2+} ions to form Ni(OH)_2 nanocrystal seeds (reaction 1.4). The other is that H_2O and NH_3 molecules coordinate Ni^{2+} ions, forming the nickel-water-ammonia complex, which can be further hydrolysed into Ni(OH)_2 by additional OH^- ions, as suggested by Xia et al. (reaction 1.10).

Based on this model, Ni(OH)_2 formation was explained as follows. First, reaction 1.4 occurs, forming Ni(OH)_2 nanocrystal seeds which anchor on TiO_2 surface to reduce the surface energy via a

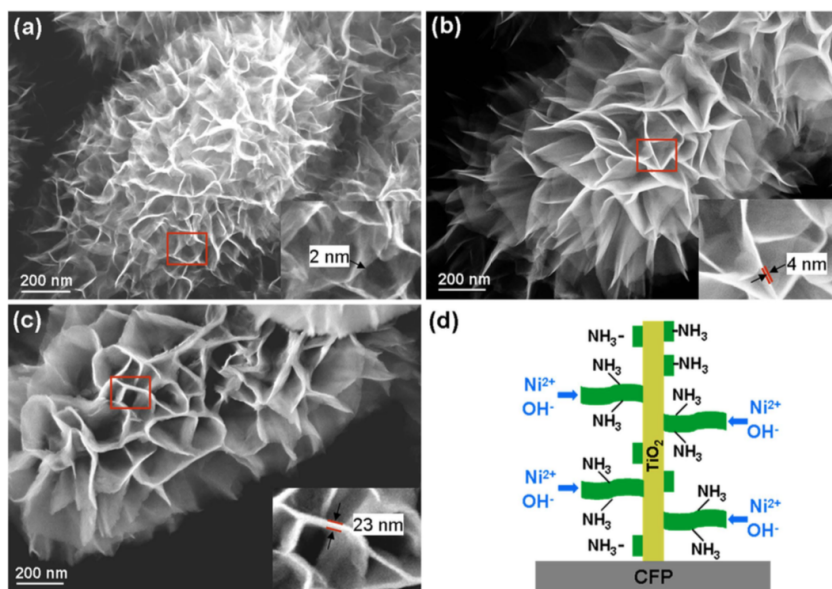


Figure 1.15: SEM images of $\text{Ni}(\text{OH})_2$ nanosheets on TiO_2 nanowires grown by CBD with different ammonia concentrations: (a) 1.8, (b) 2.4 and (c) 3.4% NH_3 in H_2O (the insets are high-magnification SEM images). (d) Schematic illustration of $\text{Ni}(\text{OH})_2$ nanosheets growth process [1.13].

heterogeneous nucleation process. Then, $\text{Ni}(\text{OH})_2$ nanosheets are formed because of ammonia. In fact, it has been reported that NH_3 molecules selectively adsorb onto (001) crystal faces of $\text{Ni}(\text{OH})_2$ by hydrogen bonds, existing between the nitrogen atom of ammonia and the hydrogen atom of the surface hydroxyl groups (N-H-O), as illustrated in Figure 1.16 [1.61]. Therefore, the (001) faces are passivated and $\text{Ni}(\text{OH})_2$ growth proceeds only along the [001] direction, forming nanosheets (Figure 1.15(d)). However, adsorbed NH_3 molecules can react with H_2O molecules and Ni^{2+} ions in solution, forming the nickel-water-ammonia complex, which can further lead to $\text{Ni}(\text{OH})_2$ precipitation upon reaction with OH^- ions (reaction 1.10). As a re-

sult, an increase in the ammonia concentration leads to an increase in OH^- ions concentration and thus nanosheets thickness based on reaction 1.10.

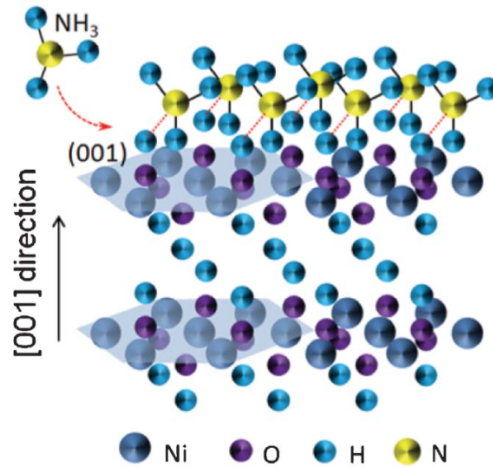


Figure 1.16: Schematic illustration of NH_3 molecules attached to (001) faces of $\beta\text{-Ni}(\text{OH})_2$ nanosheets [1.61].

Differently from persulfate-based models, potassium persulfate was not even included in this model, however Ke reported no film formation in the absence of persulfate, in agreement with Han.

1.3.3 Film growth kinetics

Han et al. studied also the growth mechanism of NiO thin films prepared by CBD, using a quartz crystal microbalance (QCM) and monitoring film thickness in real time during CBD (Figure 1.17(a)) [1.22].

Three different growth regimes were distinguished:

- an initial induction phase (I), a few seconds long, where no film growth is recorded;

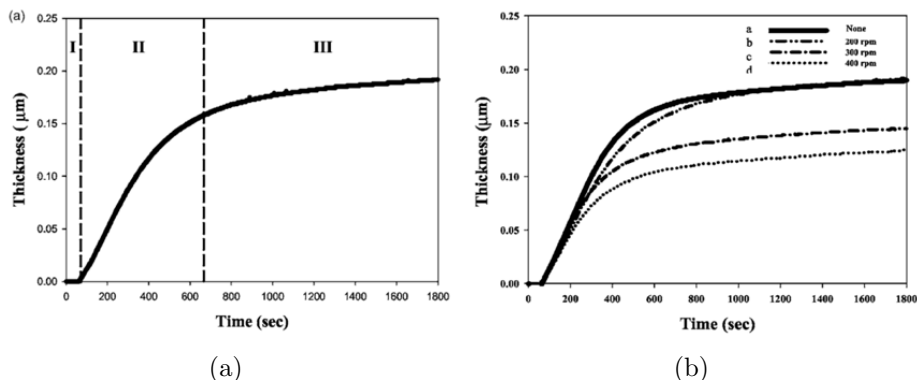


Figure 1.17: Film thickness versus time measured by QCM during CBD: (a) without solution stirring and (b) at different stirring speeds [1.22].

- a linear growth regime (II), ~ 10 min long, where film thickness increases proportionally with growth time;
- a depletion growth regime (III), where film growth rate drops quickly to zero and final film thickness is reached.

The effect of solution stirring was also investigated, finding that final film thickness was strongly dependent on the stirring speed (Figure 1.17(b)). In particular, while the induction phase and growth rate in the linear growth regime were almost unaffected by stirring, the duration of the linear growth regime shortened with increasing stirring speed. As a consequence, the depletion growth regime was reached in less time than without stirring, resulting in a lower final film thickness. This result was interpreted by the competition between heterogeneous nucleation and film growth on the substrate, and homogeneous nucleation and growth of particles in solution. Then, the resulting final thickness is determined by the relative rates of these processes. In fact, higher stirring speed can enhance particles aggregation and growth in solution at the expense of film growth and, thus, final film thickness.

1.4 Conclusions

In this chapter, the crystal structure and the physical and chemical properties of $\text{Ni}(\text{OH})_2$ and NiO nanostructures have been systematically outlined. Recent advancements on synthesis methods of $\text{Ni}(\text{OH})_2$ and NiO nanostructures have been also discussed. Typically $\text{Ni}(\text{OH})_2$ is first obtained by various methods, such as chemical and electrochemical precipitation, sol-gel, ageing, hydrothermal, electrochemical oxidation and CBD. Then, NiO is obtained by thermal annealing. In particular, CBD is considered to be the most advantageous method to synthesize $\text{Ni}(\text{OH})_2$ and NiO thin films, being simple, low-cost, large area and scalable. The deposited films display the peculiar morphology of “nanowalls”, i.e. a tight network of nanosheets (10-20 nm thick) aligned on a substrate, with high porosity and surface-to-volume ratio. Despite several attempts have been made to clarify film growth by CBD, a model that fully explains the mechanism of film formation and growth kinetics is still absent. The development of such a model is required to fully exploit the potential of $\text{Ni}(\text{OH})_2$ and NiO thin films, enabling improved performances in sensing and energy storage applications.

In the following chapter, film formation and growth kinetics by CBD have been investigated and successfully modelled. The improved growth opened the route towards enhanced performances in non-enzymatic glucose sensing, DNA sensing, gas sensing and energy storage.

References

- [1.1] Z. L. Wang, From nanogenerators to piezotronics—A decade-long study of ZnO nanostructures, *MRS Bulletin* **37**, 814 (2012).
- [1.2] U. P. M. Ashik, S. Kudo, and J. Hayashi, *Synthesis of Inorganic Nanomaterials* (Elsevier, 2018), pp. 19–57.

- [1.3] F. T. Rabouw and C. de Mello Donega, *Photoactive Semiconductor Nanocrystal Quantum Dots* (Springer, 2017), pp. 1–30.
- [1.4] R. Narayan, *Nanobiomaterials: Nanostructured Materials for Biomedical Applications* (Woodhead Publishing, 2017).
- [1.5] D. S. Hall, D. J. Lockwood, C. Bock, and B. R. MacDougall, Nickel hydroxides and related materials: a review of their structures, synthesis and properties, *Proceedings of the Royal Society A: Mathematical, Physical and Engineering Sciences* **471**, 20140792 (2015).
- [1.6] M. M. Sk, C. Y. Yue, K. Ghosh, and R. K. Jena, Review on advances in porous nanostructured nickel oxides and their composite electrodes for high-performance supercapacitors, *Journal of Power Sources* **308**, 121 (2016).
- [1.7] J. Zhang, X. Liu, G. Neri, and N. Pinna, Nanostructured Materials for Room-Temperature Gas Sensors, *Advanced Materials* **28**, 795 (2016).
- [1.8] A. Landman, H. Dotan, G. E Shter, M. Wullenkord, A. Houaijia, A. Maljusch, G. S Grader, and A. Rothschild, Photoelectrochemical water splitting in separate oxygen and hydrogen cells, *Nature Materials* **16**, 646 (2017).
- [1.9] <https://en.wikipedia.org>.
- [1.10] H. Bode, K. Dehmelt, and J. Witte, Zur kenntnis der nickelhydroxidelektrode—I. Über das nickel (II)-hydroxidhydrat, *Electrochimica Acta* **11**, 1079 (1966).
- [1.11] D. S. Hall, Ph.D. thesis, Université d'Ottawa/University of Ottawa, 2014.
- [1.12] K.-H. Young, L. Wang, S. Yan, X. Liao, T. Meng, H. Shen, and W. Mays, Fabrications of High-Capacity Alpha-Ni(OH)₂, *Batteries* **3**, 6 (2017).

- [1.13] Q. Ke, M. Zheng, H. Liu, C. Guan, L. Mao, and J. Wang, 3D $\text{TiO}_2@\text{Ni}(\text{OH})_2$ Core-Shell Arrays with Tunable Nanostructure for Hybrid Supercapacitor Application, *Scientific Reports* **5**, 13940 (2015).
- [1.14] P. Oliva, J. Leonardi, J. F. Laurent, C. Delmas, J. J. Braconnier, M. Figlarz, F. Fievet, and A. de Guibert, Review of the structure and the electrochemistry of nickel hydroxides and oxy-hydroxides, *Journal of Power Sources* **8**, 229 (1982).
- [1.15] G. Hu, C. Li, and H. Gong, Capacitance decay of nanoporous nickel hydroxide, *Journal of Power Sources* **195**, 6977 (2010).
- [1.16] O. Diaz-Morales, D. Ferrus-Suspedra, and M. T. M. Koper, The importance of nickel oxyhydroxide deprotonation on its activity towards electrochemical water oxidation, *Chemical Science* **7**, 2639 (2016).
- [1.17] P. Hermet, L. Gourrier, J.-L. Bantignies, D. Ravot, T. Michel, S. Deabate, P. Boulet, and F. Henn, Dielectric, magnetic, and phonon properties of nickel hydroxide, *Physical Review B* **84**, 235211 (2011).
- [1.18] A. Motori, F. Sandrolini, and G. Davolio, Electrical properties of nickel hydroxide for alkaline cell systems, *Journal of Power Sources* **48**, 361 (1994).
- [1.19] Attila Palencsár and Daniel A Scherson, In Situ Resistance Measurements of Single Particle Spherical $\text{Ni}(\text{OH})_2$ Microelectrodes as a Function of Their State of Charge, *Electrochemical and Solid-State Letters* **8**, A328 (2005).
- [1.20] K. O. Ukoba, A. C. Eloka-Eboka, and F. L. Inambao, Review of nanostructured NiO thin film deposition using the spray pyrolysis technique, *Renewable and Sustainable Energy Reviews* **82**, 2900 (2018).

- [1.21] N. D. Hoa and S. A. El-Safty, Synthesis of Mesoporous NiO Nanosheets for the Detection of Toxic NO₂ gas, *Chemistry–A European Journal* **17**, 12896 (2011).
- [1.22] S.-Y. Han, D.-H. Lee, Y.-J. Chang, S.-O. Ryu, T.-J. Lee, and C.-H. Chang, The Growth Mechanism of Nickel Oxide Thin Films by Room-Temperature Chemical Bath Deposition, *Journal of the Electrochemical Society* **153**, C382 (2006).
- [1.23] W. E. Spear and D. S. Tannhauser, Hole Transport in Pure NiO Crystals, *Physical Review B* **7**, 831 (1973).
- [1.24] F. J. Morin, Electrical Properties of NiO, *Physical Review* **93**, 1199 (1954).
- [1.25] K. V. Rao and A. Smakula, Dielectric Properties of Cobalt Oxide, Nickel Oxide, and Their Mixed Crystals, *Journal of Applied Physics* **36**, 2031 (1965).
- [1.26] M. Jlassi, I. Sta, M. Hajji, and H. Ezzaouia, Synthesis and characterization of nickel oxide thin films deposited on glass substrates using spray pyrolysis, *Applied Surface Science* **308**, 199 (2014).
- [1.27] C. G. Granqvist, Solar Energy Materials, *Advanced Materials* **15**, 1789 (2003).
- [1.28] E. Avendaño, L. Berggren, G. A. Niklasson, C. G. Granqvist, and A. Azens, Electrochromic materials and devices: Brief survey and new data on optical absorption in tungsten oxide and nickel oxide films, *Thin Solid Films* **496**, 30 (2006).
- [1.29] R. Barnard, C. F. Randell, and F. L. Tye, Studies concerning the ageing of α and β -Ni (OH)₂ in relation to nickel–cadmium cells, *Power Sources* **8**, 401 (1981).

- [1.30] R. S. McEwen, Crystallographic studies on nickel hydroxide and the higher nickel oxides, *The Journal of Physical Chemistry* **75**, 1782 (1971).
- [1.31] R. S. Jayashree and P. V. Kamath, Factors governing the electrochemical synthesis of α -nickel (II) hydroxide, *Journal of Applied Electrochemistry* **29**, 449 (1999).
- [1.32] M. Dixit, G. N. Subbanna, and P. V. Kamath, Homogeneous precipitation from solution by urea hydrolysis: a novel chemical route to the α -hydroxides of nickel and cobalt, *Journal of Materials Chemistry* **6**, 1429 (1996).
- [1.33] S. L. Medway, C. A. Lucas, A. Kowal, R. J. Nichols, and D. Johnson, In situ studies of the oxidation of nickel electrodes in alkaline solution, *Journal of Electroanalytical Chemistry* **587**, 172 (2006).
- [1.34] X. Dai, D. Chen, H. Fan, Y. Zhong, L. Chang, H. Shao, J. Wang, J. Zhang, and C.-N. Cao, Ni(OH)₂/NiO/Ni composite nanotube arrays for high-performance supercapacitors, *Electrochimica Acta* **154**, 128 (2015).
- [1.35] D. S. Hall, D. J. Lockwood, S. Poirier, C. Bock, and B. R. MacDougall, Raman and Infrared Spectroscopy of α and β Phases of Thin Nickel Hydroxide Films Electrochemically Formed on Nickel, *The Journal of Physical Chemistry A* **116**, 6771 (2012).
- [1.36] Y. Fan, Z. Yang, X. Cao, P. Liu, S. Chen, and Z. Cao, Hierarchical Macro-Mesoporous Ni(OH)₂ for Nonenzymatic Electrochemical Sensing of Glucose, *Journal of The Electrochemical Society* **161**, B201 (2014).
- [1.37] S. Zhang and H. C. Zeng, Self-Assembled Hollow Spheres of β -Ni(OH)₂ and Their Derived Nanomaterials, *Chemistry of Materials* **21**, 871 (2009).

- [1.38] L. Gourrier, S. Deabate, T. Michel, M. Paillet, P. Hermet, J.-L. Bantignies, and F. Henn, Characterization of Unusually Large Pseudo-Single Crystal” of β -Nickel Hydroxide, *The Journal of Physical Chemistry C* **115**, 15067 (2011).
- [1.39] L. Dong, Y. Chu, and W. Sun, Controllable Synthesis of Nickel Hydroxide and Porous Nickel Oxide Nanostructures with Different Morphologies, *Chemistry–A European Journal* **14**, 5064 (2008).
- [1.40] Z. Zhu, N. Wei, H. Liu, and Z. He, Microwave-assisted hydrothermal synthesis of $\text{Ni}(\text{OH})_2$ architectures and their in situ thermal convention to NiO, *Advanced Powder Technology* **22**, 422 (2011).
- [1.41] X. H. Xia, J. P. Tu, J. Zhang, X. L. Wang, W. K. Zhang, and H. Huang, Electrochromic properties of porous NiO thin films prepared by a chemical bath deposition, *Solar Energy Materials and Solar Cells* **92**, 628 (2008).
- [1.42] K. O. Iwu, A. Lombardo, R. Sanz, S. Scirè, and S. Mirabella, Facile synthesis of Ni nanofoam for flexible and low-cost non-enzymatic glucose sensing, *Sensors and Actuators B: Chemical* **224**, 764 (2016).
- [1.43] T. Schneller, R. Waser, M. Kosec, and D. Payne, *Chemical Solution Deposition of Functional Oxide Thin Films* (Springer, 2013).
- [1.44] P. Pramanik and S. Bhattacharya, A Chemical Method for the Deposition of Nickel Oxide Thin Films, *Journal of the Electrochemical Society* **137**, 3869 (1990).
- [1.45] G. Li, X. Wang, L. Liu, R. Liu, F. Shen, Z. Cui, W. Chen, and T. Zhang, Controllable Synthesis of 3D $\text{Ni}(\text{OH})_2$ and NiO Nanowalls on Various Substrates for High-Performance Nanosensors, *Small* **11**, 731 (2015).

- [1.46] <https://www.google.com>.
- [1.47] A. J. Varkey and A. F. Fort, Solution growth technique for deposition of nickel oxide thin films, *Thin Solid Films* **235**, 47 (1993).
- [1.48] P. S. Patil and L. D. Kadam, Preparation and characterization of spray pyrolyzed nickel oxide (NiO) thin films, *Applied Surface Science* **199**, 211 (2002).
- [1.49] B. Pejova, T. Kocareva, M. Najdoski, and I. Grozdanov, A solution growth route to nanocrystalline nickel oxide thin films, *Applied Surface Science* **165**, 271 (2000).
- [1.50] B. Sasi, K. G. Gopchandran, P. K. Manoj, P. Koshy, P. P. Rao, and V. K. Vaidyan, Preparation of transparent and semiconducting NiO films, *Vacuum* **68**, 149 (2002).
- [1.51] S. A. Mahmoud, A. A. Akl, H. Kamal, and K. Abdel-Hady, Opto-structural, electrical and electrochromic properties of crystalline nickel oxide thin films prepared by spray pyrolysis, *Physica B: Condensed Matter* **311**, 366 (2002).
- [1.52] K. Nakaoka, J. Ueyama, and K. Ogura, Semiconductor and electrochromic properties of electrochemically deposited nickel oxide films, *Journal of Electroanalytical Chemistry* **571**, 93 (2004).
- [1.53] Y. F. Yuan, X. H. Xia, J. B. Wu, J. L. Yang, Y. B. Chen, and S. Y. Guo, Nickel foam-supported porous Ni(OH)₂/NiOOH composite film as advanced pseudocapacitor material, *Electrochimica Acta* **56**, 2627 (2011).
- [1.54] X. Xia, J. Tu, Y. Zhang, X. Wang, C. Gu, X.-B. Zhao, and H. J. Fan, High-Quality Metal Oxide Core/Shell Nanowire Arrays on Conductive Substrates for Electrochemical Energy Storage, *ACS Nano* **6**, 5531 (2012).

- [1.55] N. A. Alhebshi, R. B. Rakhi, and H. N. Alshareef, Conformal coating of Ni(OH)₂ nanoflakes on carbon fibers by chemical bath deposition for efficient supercapacitor electrodes, *Journal of Materials Chemistry A* **1**, 14897 (2013).
- [1.56] M. W. Anderson, J. T. Gebbie-Rayet, A. R. Hill, N. Farida, M. P. Attfield, P. Cubillas, V. A. Blatov, D. M. Proserpio, D. Akporiaye, B. Arstad, and J. D. Gale, Predicting crystal growth via a unified kinetic three-dimensional partition model, *Nature* **544**, 456 (2017).
- [1.57] Y.-Z. Long, M. Yu, B. Sun, C.-Z. Gu, and Z. Fan, Recent advances in large-scale assembly of semiconducting inorganic nanowires and nanofibers for electronics, sensors and photovoltaics, *Chemical Society Reviews* **41**, 4560 (2012).
- [1.58] P. Bukovec, N. Bukovec, B. Orel, and K. S. Wisiak, Thermal analysis of nickel oxide films, *Journal of Thermal Analysis* **40**, 1193 (1993).
- [1.59] G. Hodes, *Chemical Solution Deposition of Semiconductor Films* (CRC press, 2002).
- [1.60] S. M. Pawar, A. I. Inamdar, K. V. Gurav, Y. Jo, H. Kim, J. H. Kim, and H. Im, Effect of oxidant on the structural, morphological and supercapacitive properties of nickel hydroxide nanoflakes electrode films, *Materials Letters* **141**, 336 (2015).
- [1.61] G. Li, X. Wang, H. Ding, and T. Zhang, A facile synthesis method for Ni(OH)₂ ultrathin nanosheets and their conversion to porous NiO nanosheets used for formaldehyde sensing, *RSC Advances* **2**, 13018 (2012).

Chapter 2

Ni-based nanowalls for non-enzymatic glucose sensing

Contents

2.1	Non-enzymatic glucose sensing	52
2.2	Materials and methods	57
2.2.1	Synthesis	57
2.2.2	Characterization	58
2.3	Ni-based nanowalls	59
2.3.1	Morphological, structural and chemical characterization . .	59
2.3.2	Growth model	67
2.3.3	Electrochemical properties	72
2.3.4	Glucose detection performances	74
2.4	Conclusions	79
	References	80

Non-enzymatic glucose sensing is a particularly active research field, given the growing number of diabetic patients and, consequently, the need to develop simple, low-cost and non-invasive devices that operate with physiological fluids (e.g. human tears and saliva) other than blood. However, due to the very low glucose concentration in these fluids, new materials with enhanced sensitivity towards sub-mM glucose concentrations are required. Ni-based nanostructures are attractive catalytic materials for many electrochemical applications, among which non-enzymatic glucose sensing. In this chapter, the growth kinetics of Ni-based nanowalls, a self-assembled network of nanosheets (10-20 nm thick, 0.1÷1 µm tall) grown by chemical bath deposition (CBD), is investigated and modelled. Using scanning electron microscopy (SEM), X-ray diffraction (XRD) and Rutherford backscattering spectrometry (RBS) two growth regimes have been identified for CBD at room temperature: first, the fast growth of disordered NiOOH·4Ni(OH)₂ nanosheets occurs, followed by a slower growth of well-aligned α-Ni(OH)₂ nanosheets. A higher growth temperature of 50°C, leading only to well-aligned nanosheets, demonstrated superior electrochemical properties in terms of charge storage and charge transfer, as confirmed by cyclic voltammetry (CV) and electrochemical impedance spectroscopy analyses (EIS). The improved growth kinetics was then applied to non-enzymatic glucose sensing, reaching the unprecedentedly high sensitivity of 31 mA mM⁻¹ cm⁻² on a linear range of 0.02÷0.4 mM, which matches the requirements for non-enzymatic glucose sensing in tears and saliva.

2.1 Non-enzymatic glucose sensing

In the last decades there has been an increasing interest of the scientific community for quantitative determination of different chemical species, which is often driven by practical and urgent needs as in the case of the diagnosis and care of diabetes.

Diabetes includes a series of metabolic disorders associated with a persistent hyperglycemic condition, i.e. an increase of sugars (glucose) concentration in blood, caused by a pathological reduction of insulin secretion by the pancreas. Among the complications of diabetes there are ketoacidosis (accumulation of altered metabolism products) and chronic diseases which involve different organs, including eyes, kidneys, heart, blood vessels and peripheral nerves [2.1].

According to the World Health Organization (WHO), there are more than 400 million people suffering from diabetes in the world (Figure 2.1). This number is continuously increasing and, based on current projections, diabetes will be the seventh cause of death in 2030.

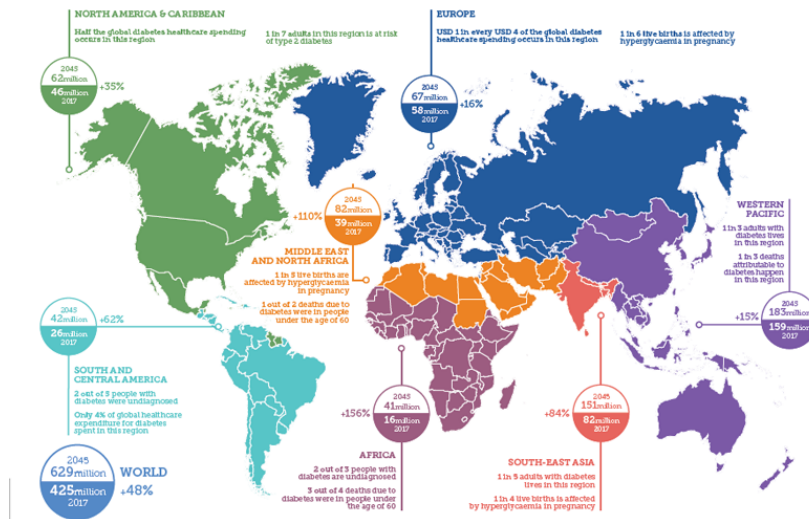


Figure 2.1: Estimated number of people with diabetes worldwide and per region in 2017, and predicted for 2045 [2.2].

Although it is not easy to accurately estimate the costs for diabetes, it is unquestionable that these affect heavily the finances of national health services in various countries. For example, according to data provided by the American Diabetes Association, the total

cost of diagnosed diabetes in the USA in 2018 was about 327 billion of dollars, 67.3% paid by the government [2.3].

The costs for diabetic patients are also particularly high due largely to glucose self-monitoring. In fact, for a diabetic patient it is vital to constantly monitor the level of glucose in the blood. This is typically done with enzymatic sensors, based on electrodes containing an enzyme (glucose oxidase) specific for glucose oxidation and capable of producing an electrical signal related to the concentration of glucose in the blood (3–8 mM for a healthy patient). The most common glucometer is reported in Figure 2.2(a). This device forces the patient to prick his finger to extract the blood drop to be examined.



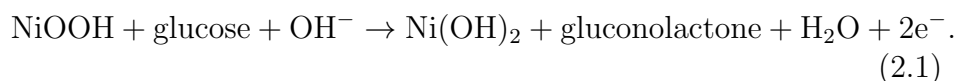
Figure 2.2: (a) A typical kit for glucose self-monitoring, consisting in an enzymatic glucometer and a lancing device, and (b) Google Contact Lens, formed by a miniaturized sensor and a wireless communication system [2.4].

The main disadvantage of enzymatic glucometers lies in the invasiveness of the measurement, which is typically repeated several times during the day without allowing to catch any anomalies between one measurement and another. Because of the invasiveness, children and adolescents are particularly reluctant to perform these measurements. Furthermore, because of the enzyme instability it

is necessary to replace the electrode after one or two weeks of use, increasing the cost for glucose self-monitoring [2.5, 6].

To overcome the limitations of enzymatic sensors, researchers are now focused on the development of “user-friendly” devices that can detect glucose in other physiological fluids such as human tears and saliva. For example, Google is working on “smart” contact lenses, based on a miniaturized sensor connected to an antenna, that could measure and communicate glucose levels in tears via wireless (Figure 2.2(b)). However, the glucose concentration in tears and saliva is orders of magnitude lower than blood (0.02-0.07 and 0.02-0.4 mM, respectively). Therefore, non-enzymatic glucose sensors with excellent sensing performances to such low glucose concentrations are required.

The best strategy for non-enzymatic glucose sensing is represented by the combination of materials that can directly oxidize glucose and nanostructures, which thanks to their high surface-to-volume ratio offer a larger area for glucose detection, reaching high sensitivity and decreasing the limit of detection (LoD) without the complications due to the enzyme. Different nanomaterials have been tested for non enzymatic glucose sensing, including metals (Pt, Au, Cu, Ni, Ag) [2.1, 7], alloys (Cu-Ag, Pt-Pd) [2.8, 9] and metal oxides (CuO, NiO) [2.10–13]. Among them, Ni-based nanostructures are considered the best ones due to their typical high sensitivity and low-cost, especially if compared to Au and Pt [2.5]. Direct glucose oxidation in Ni-based nanostructures is enabled by the $\text{Ni}^{2+}/\text{Ni}^{3+}$ redox couple, as in the case of $\text{Ni}(\text{OH})_2/\text{NiOOH}$ [2.5]:



Unfortunately, non-enzymatic glucose sensors suffer from poor selectivity if compared to enzymatic ones, limiting the development of commercial products.

Typically, the non-enzymatic glucose sensing performances of materials are tested by using a potentiostat and a three electrode setup (a Pt counter electrode, a reference electrode and the sensing ma-

terial as working electrode) in 0.1 M NaOH (pH \sim 12) as supporting electrolyte. Then, chronoamperometric measurements (current vs time) are performed by applying a constant potential equal to the oxidation potential of the sensing material (for example Ni(OH) $_2 \rightarrow$ NiOOH). Each glucose addition, according to equation 2.1, induces a current increase, while the applied potential allows the catalytic effect through a continuous regeneration of the oxidizing species (NiOOH). Figure 2.3 reports a characteristic chronoamperometric curve for different additions of glucose. Glucose sensitivity is further obtained by the linear fit of the calibration curve, as shown in the inset in Figure 2.3.

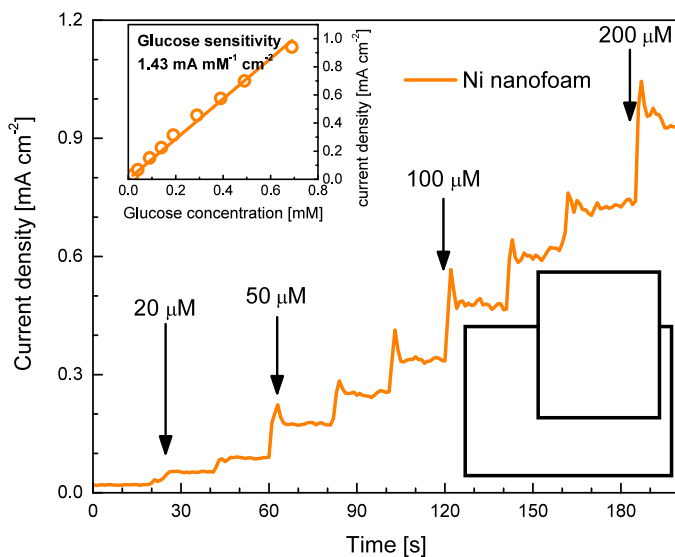


Figure 2.3: Amperometric response of the Ni nanofoam with successive additions of glucose at 20 s time intervals in 0.1 M NaOH. The inset is the calibration curve (adapted from ref. [2.14]).

Among the more recent Ni-based nanostructures reported for non-enzymatic glucose sensing, Ni nanofoam, an ensemble of Ni nanoparticles (20-30 nm in size) obtained upon annealing in reducing atmosphere of Ni-based nanowalls grown by CBD, is the most promising one. In fact, Ni nanofoam showed excellent non-enzymatic glucose sensing performances in terms of high sensitivity of $2.37 \text{ mA mM}^{-1} \text{ cm}^{-2}$ in the range $0.01 \div 0.7 \text{ mM}$, low LoD of $5 \mu\text{M}$, quick response time (1 s), high selectivity against common interfering species ($200 \mu\text{M}$ glucose versus $20 \mu\text{M}$ uric acid, $10 \mu\text{M}$ ascorbic acid and $10 \mu\text{M}$ acetaminophen) and long-term stability (4% response loss after 64 days) [2.14]. Nevertheless, the sensitivity of Ni nanofoam is strongly dependent on electrolyte pH, decreasing significantly by reducing the pH from 12 to 7.4, which is close to the pH value of physiological fluids [2.15]. To further improve the sensitivity of Ni nanofoam, the simplest approach is to optimize the CBD deposition of Ni-based nanowalls. In fact, a full comprehension of the growth mechanism during CBD could lead to an effective improvement of the catalytic properties of Ni-based nanowalls, and thus Ni nanofoam.

2.2 Materials and methods

2.2.1 Synthesis

Ni-based nanowalls were grown by CBD on c-Si substrates ($1 \times 2 \text{ cm}^2$ samples, cut from *n*-type, 6' Czochralski wafers), or on commercial indium-doped tin oxide (ITO) substrates (working area $1 \times 1 \text{ cm}^2$) or on Ni foam (Goodfellow, thickness 1.6 mm, porosity 95%, 20 pores cm^{-1}) substrates, after rinsing with isopropanol and deionized water (MilliQ, $18 \text{ M}\Omega \text{ cm}$), and drying in N_2 gas flow. Solution for CBD was prepared by mixing $0.42 \text{ M NiSO}_4 \cdot 6\text{H}_2\text{O}$ (Sigma-Aldrich, 99%), $0.07 \text{ M K}_2\text{S}_2\text{O}_8$ (Sigma-Aldrich, 99%) and 3.5 wt% ammonia (Sigma-Aldrich, 28–30 wt% NH_3 in H_2O). Particular care was taken to prepare the solution by adding the reagents in the above-mentioned order, while performing mechanical agitation ($\sim 20 \text{ s}$) to facilitate

their dissolution. Just after solution preparation, substrates were immersed vertically in it and kept at room temperature for varying durations (60-7200 s) in order to study the growth kinetics. Then, samples were rinsed several times with deionized water to remove unwanted microparticulate, if any, and dried under N_2 gas flow. To investigate the effect of growth temperature on the film growth, the very same procedure was repeated by maintaining the temperature at 50°C through a bain-marie configuration. All samples were labelled with growth temperature and time (e.g., RT-480 indicates the film deposited at room temperature for 480 s).

Some films grown on ITO or on Ni foam substrates were also annealed at 350°C for 60 min in Ar followed by 60 min in forming gas (Ar:H₂ 95:5 mixture) to obtain Ni nanofoam electrodes useful for glucose sensing tests [2.14].

2.2.2 Characterization

Si substrates were used to conduct morphological analysis of Ni-based nanowalls. The surface morphology and thickness of samples were characterized by a scanning electron microscope (Gemini field emission SEM Carl Zeiss SUPRA 25) combined with energy dispersive X-ray spectroscopy (EDX). The crystalline phases of samples were identified by XRD in glancing incidence mode (0.2°) using a Smartlab Rigaku diffractometer, equipped with a rotating anode of Cu K_α radiation, operating at 45 kV and 200 mA. RBS (2.0 MeV He⁺ beam at normal incidence) with a 165° backscattering angle was performed by a 3.5 MV HVEE Singletron accelerator system. RBS spectra were analyzed using XRump software to study the elemental composition of samples [2.16].

Electrochemical analyses were performed using a potentiost (VersaSTAT 4, Princeton Applied Research, USA) and a three-electrode setup with a Pt counter electrode, a saturated calomel electrode (SCE) as reference electrode, and working electrodes ($1 \times 1 \text{ cm}^2$ immersed area). All measurements were performed at room temper-

ature in 0.1 M sodium hydroxide (NaOH, ACS reagent, $\geq 97\%$) supporting electrolyte. CV curves were recorded at 50 mV s^{-1} scan rate in the potential range $-0.1\div 0.9\text{ V}$. EIS was performed at the oxidation potential with a 20 mV superimposed sinusoidal voltage in the frequency range $10^2\text{-}10^{-2}\text{ Hz}$. CA analysis was employed to study the non-enzymatic glucose sensing performances of samples. CA measurements were performed under continuous stirring, in order to promptly homogenize the glucose in the solution and to help the out-diffusion of the oxidation products, by applying a constant potential equal to the oxidation peak.

2.3 Ni-based nanowalls

2.3.1 Morphological, structural and chemical characterization

The as-deposited films were uniform in appearance and exhibited a black/grey colour to the naked eye. The SEM images reported in Figure 2.4 show the plan view (top panels) and cross-sectional view (bottom panels) of RT-2700 (Figure 2.4(a)), RT-480 (Figure 2.4(b)) and 50–480 (Figure 2.4(c)). All samples are characterized by an open nanoporous structure formed by interconnected nanosheets, each with a thickness of $10\text{--}20\text{ nm}$. Comparing Figure 2.4(a) and (b), it seems that the size of these pores increases with growth time, while for fixed growth time, the growth temperature produce a shrinkage of the pores size distribution (Figure 2.4(b) and (c)).

The cross-sectional image of RT-480 (Figure 2.4(b)) shows that the film has a thickness of $\sim 350\text{ nm}$ and is composed of randomly oriented sheets with irregular shapes. RT-2700 (Figure 2.4(a)) is thicker ($\sim 1100\text{ nm}$), as expected, and its profile reveals a messy structure (similar to RT-480) up to a thickness of $400\text{--}500\text{ nm}$, on top of which a more loose-fitting feature is present. These considerations agree with the plane views (Figure 2.4(a) and (b)) and suggest

complex kinetics with at least two different regimes: an early stage (random regime) producing disordered nanosheets, and a subsequent phase (self-ordered regime) giving an ordered structure with vertical nanosheets. The cross-sectional image of 50-480 (Figure 2.4(c)) shows that the film is slightly thinner (~ 250 nm) than that grown at room temperature and same growth time. In addition, it is formed by nanosheets that are nearly perpendicular to the substrate plane, resembling the profile observed in the top part of RT-2700 (Figure 2.4(a)). Therefore, the growth temperature significantly affects the morphology of Ni-based nanowalls.

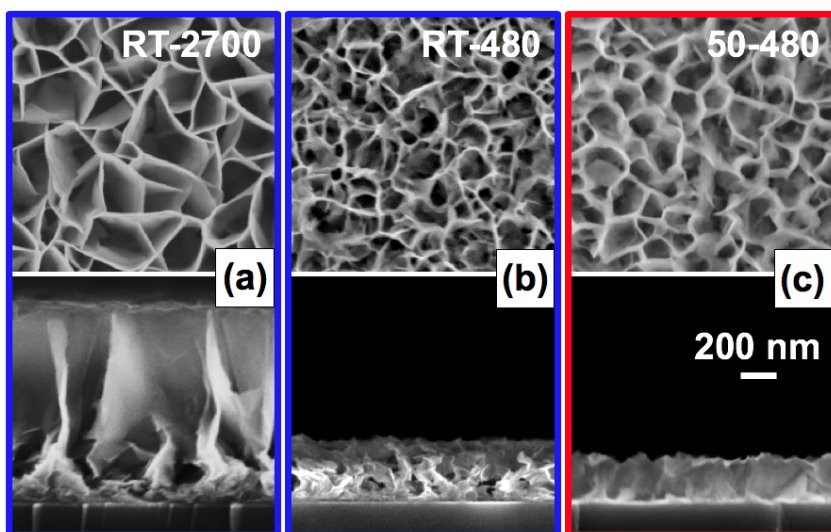


Figure 2.4: SEM images (plane views in top panels, cross-sectional views in bottom panels) of RT-2700 (a), RT-480 (b) and 50-480 (c). The scale bar is for all images [2.17].

To investigate the growth kinetics, the thickness of as-deposited films was measured by cross view SEM images as function of growth time and temperature. Figure 2.5 reports the results. The 50°C kinetics shows a fairly constant growth rate of 0.160 nm s^{-1} in the full growth time range (260-2700 s). The room temperature kinetics

supports the idea of two regimes: first a random regime (260-720 s) with a fast growth rate is observed, followed by a self-ordered regime (720÷7200 s) with a slower growth rate of 0.145 nm s^{-1} (close to that of the 50°C kinetics). Contrary to what was reported by Han and co-workers [2.18], no depletion regime stopping film thickness growth was observed, at least for growth durations up to 7200 s. Our results on the growth kinetics at the two temperatures supports the observation that nanosheets grown at 50°C for shorter times appear very similar to those formed at room temperature for longer growth times.

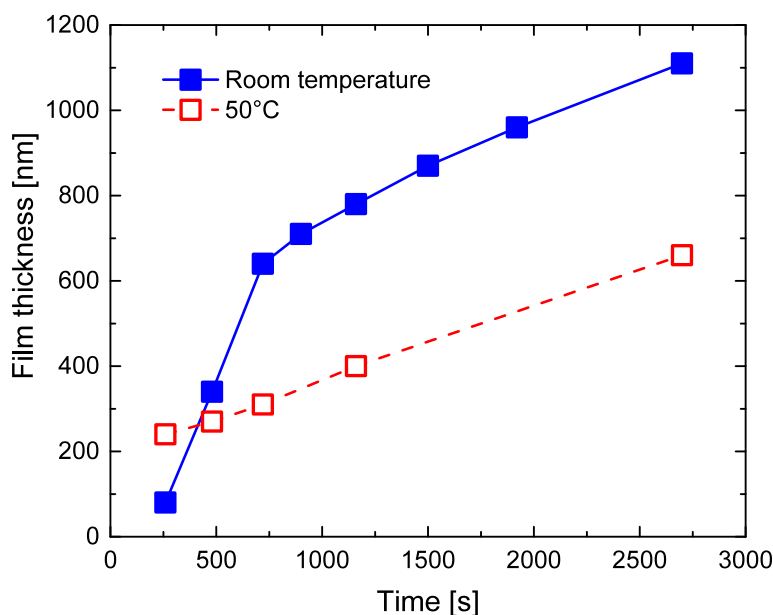


Figure 2.5: Film thickness versus growth time for samples grown at room temperature (blue closed squares) and 50°C (red open squares). The error bars are of the same size as the symbols [2.17].

Based on these observations, it can be assumed that during the random regime the fast precipitation rate causes the growth of randomly oriented and irregular nanosheets, while during the self-ordered regime the slower precipitation rate allows the growth of well-aligned nanosheets. Above 400 s, the Ni-based nanowalls at 50°C have a film thickness smaller than room temperature, probably because at higher temperatures the random regime is much shorter.

To understand the very early stage of film formation, a few samples were prepared at room temperature for less than 300 s (Figure 2.6). A heterogeneous nucleation occurs onto substrate surface, forming small nuclei that can be already observed after 60 s. Nuclei grow until they merge together and a compact film is formed at ~ 180 s. Then, film growth proceeds vertically.

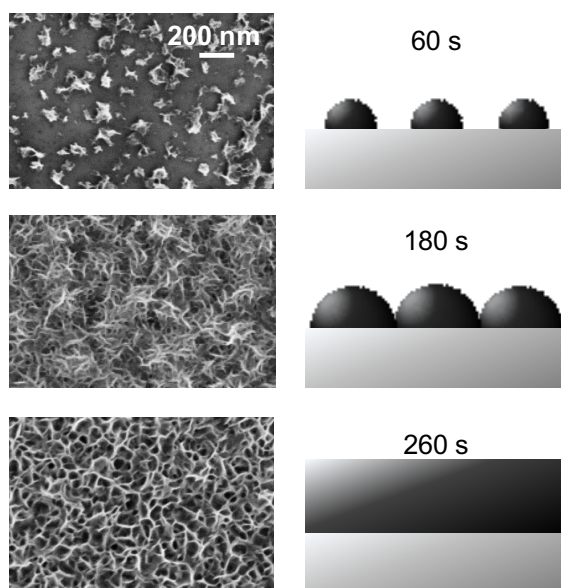


Figure 2.6: SEM images and corresponding schematic illustrations of early stage film formation at room temperature. The scale bar is for all images [2.17].

Han et al. observed no film formation in the absence of $K_2S_2O_8$

[2.18]. In this work, the role of $K_2S_2O_8$ on the growth kinetics was investigated as follows. During a room temperature growth, some $K_2S_2O_8$ was added 1200 s after solution preparation, in such a way as to double its original concentration ($0.07 \rightarrow 0.14$ M). No effect on the growth kinetics was observed at all for samples extracted after the extra addition of $K_2S_2O_8$, as their thicknesses resembled those presented in Figure 2.5 at room temperature. Another test was conducted at room temperature by immersing some substrates much later solution preparation (1200 s). No traces of Ni-based nanowalls were found. Therefore, it is clear that $K_2S_2O_8$ plays a key role in driving the CBD. Moreover, it works only immediately after solution preparation and any further addition does not affect the growth kinetics.

Figure 2.7 reports the glancing incidence XRD patterns of RT-260 and RT-1160, which belong respectively to the random regime and to the self-ordered one. In both patterns, the two sharp peaks (50.8 and 53.4°) are due to the sample holder. RT-260 shows a broad signal at $\sim 55^\circ$, related to the mixed phase $NiOOH \cdot 4Ni(OH)_2$ (PDF 06-0044). RT-1160 shows instead two clear peaks at 34 and 39° , which could be related to either $NiOOH \cdot 4Ni(OH)_2$ or $\alpha-Ni(OH)_2$ phase (JCPDS 22-04444). However, the peak at 34° has a shoulder at $\sim 33.5^\circ$, where the (110) peak of $\alpha-Ni(OH)_2$ phase is expected. RT-1160 shows also a broad signal at 55° , due to residual traces of $NiOOH \cdot 4Ni(OH)_2$ phase. Thus, XRD analysis clarified the presence of crystallites in room temperature grown Ni-based nanowalls, and showed that the random regime starts with the precipitation of $NiOOH \cdot 4Ni(OH)_2$, while $\alpha-Ni(OH)_2$ phase is formed only during the self-ordered regime.

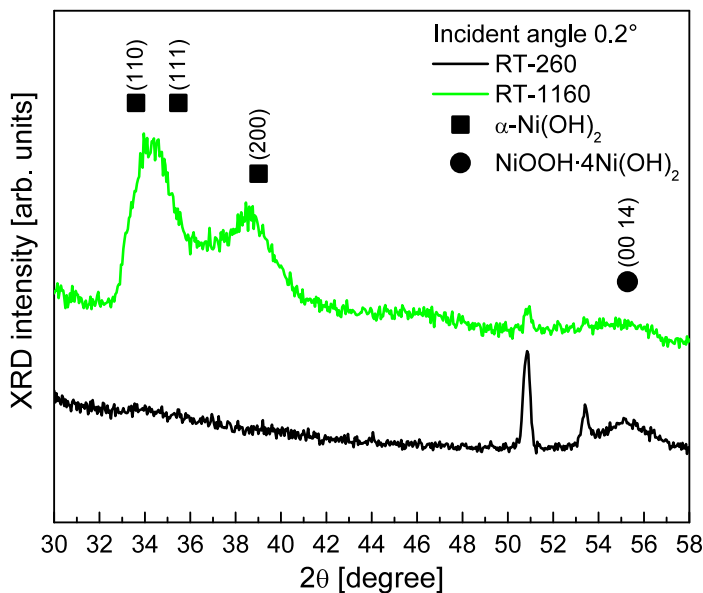


Figure 2.7: XRD patterns of RT-260 (black line) and RT-1160 (green line) [2.17].

A chemical composition analysis was conducted by RBS technique and some RBS spectra of samples grown at room temperature are shown in Figure 2.8). From right to left, a peak at ~ 1.5 MeV can be observed, attributed to Ni, the most common heavy element in the samples. At lower energies (~ 1.25 MeV), a second peak can be barely identified in the RBS spectra of RT-260 and RT-480, which could be ascribed to sulphur (S) coming from CBD reagents. Then, at ~ 0.7 MeV, a peak due to O can be further recognized on top of the broad signal of the Si substrate.

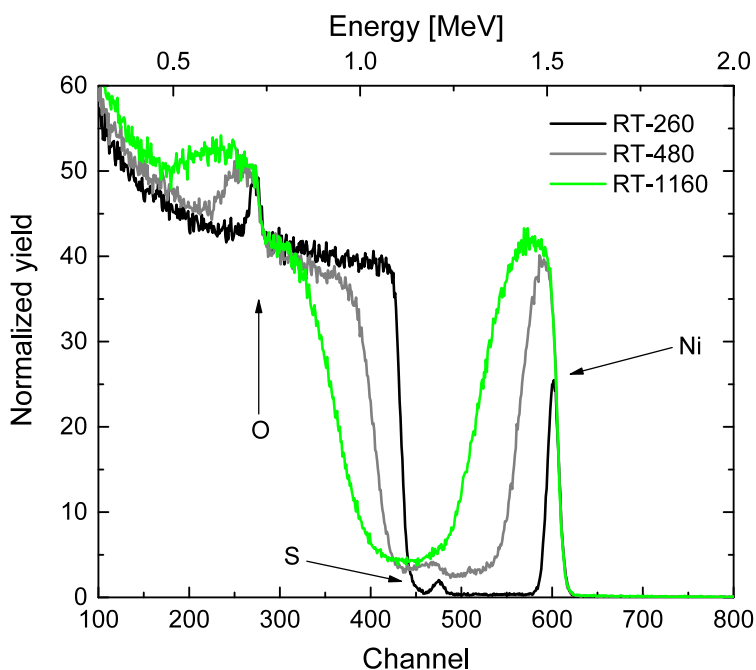
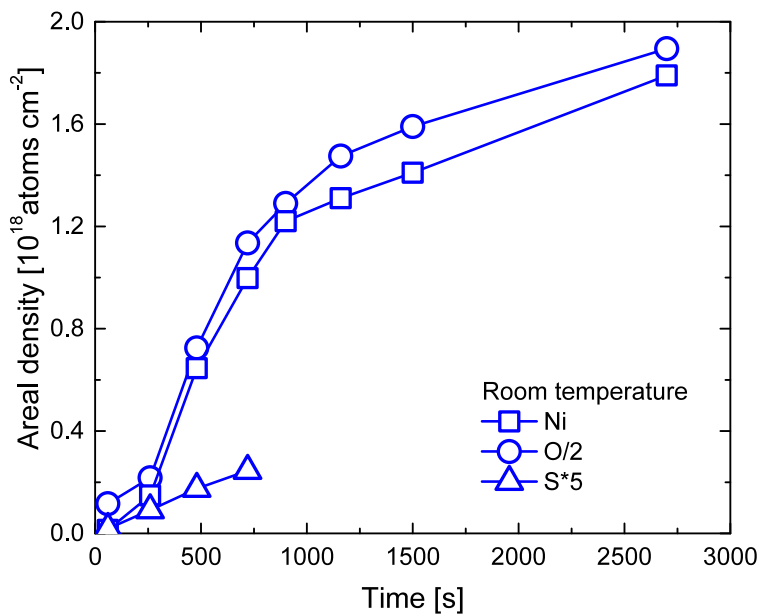
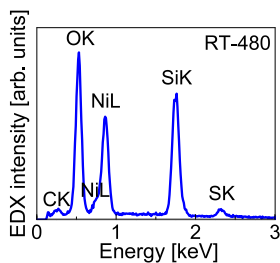


Figure 2.8: RBS spectra of RT-260 (black line), RT-480 (grey line) and RT-1160 (green line) [2.17].

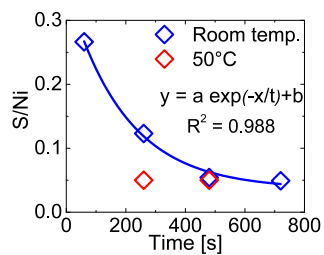
Figure 2.9(a) reports the time evolution of Ni and O areal densities in Ni-based nanowalls, as obtained by integrating the various peaks in the RBS spectra through a proper simulation code [2.16]. Ni curve follows a trend which resembles the one previously observed for film thickness measurements (Figure 2.5), suggesting that Ni precipitation flux is proportional to film growth rate during the whole deposition process. O/2 curve is close to the Ni one, pointing out a stoichiometric ratio $O/Ni \sim 2$, in agreement with $Ni(OH)_2/NiOOH$ species identified by XRD.



(a)



(b)



(c)

Figure 2.9: (a) Areal density of Ni (open squares), O/2 (open circles) and S*5 (open triangles) versus growth time obtained from the RBS spectra of samples grown at room temperature, (b) EDX spectrum of RT-480, and (c) S/Ni versus growth time at room temperature (blue open diamonds) and 50°C (red open diamonds) [2.17].

To evaluate the filling factor, i.e. the fraction of volume occupied by Ni-based nanowalls, Ni areal density, film thickness measurements and Ni concentration in $\text{Ni}(\text{OH})_2$ were joined [2.19]. As reported in Figure A1, the filling factor decreases with growth time (70% \rightarrow 60%), confirming the SEM observation that porosity increases with time.

EDX analysis of RT-480 (Figure 2.9(b)) confirmed the presence of S, which has never been observed before in Ni-based nanowalls. Figure 2.9(a) reports also the areal density of S*5 and it is interesting to note that S/Ni ratio decreases exponentially with time (Figure 2.9(c)). Due to the similar time extension, S/Ni trend seems to be correlated with the random regime and with the $\text{K}_2\text{S}_2\text{O}_8$ role observed above.

The results reported so far evidence the key roles of growth temperature and $\text{K}_2\text{S}_2\text{O}_8$ in the CBD of Ni-based nanowalls. Indeed, two clear growth regimes are attested, during which a random precipitation of $\text{NiOOH}\cdot 4\text{Ni}(\text{OH})_2$ nanosheets precedes that of self-ordered $\alpha\text{-Ni}(\text{OH})_2$ nanosheets.

2.3.2 Growth model

To understand the precipitation mechanism of Ni-based nanowalls it can be useful to separately focus on the two growth regimes. In the random regime a transient role of the persulfate ion ($\text{S}_2\text{O}_8^{2-}$) is expected, while a steady kinetics is hypothesised in the self-ordered regime.

The dissolution of $\text{NiSO}_4\cdot 6\text{H}_2\text{O}$ in the ammonia solution produces the typical blue colour, due to the formation of the nickel-water-ammonia complex. This complex is in equilibrium with the free forms of the ligands and $\text{Ni}(\text{OH})_2$ colloidal nanoparticles, as indicated by Xia et al. (reaction 1.10) [2.20]. With the addition of $\text{K}_2\text{S}_2\text{O}_8$, a chromatic variation towards a deep blue/black colour is observed in the solution, as a consequence of the reaction between $\text{S}_2\text{O}_8^{2-}$ ions and $\text{Ni}(\text{OH})_2$, leading to the formation of NiOOH through reaction

1.10 [2.20]. As a Ni^{3+} species, NiOOH is unstable in solution and precipitates [2.21]. Therefore, $\text{Ni}(\text{OH})_2$ and NiOOH are the building blocks of the random regime. Traces of S are thus incorporated into the film, as indicated by RBS analyses, and a random precipitation occurs, leading to a disordered structure (Figure 2.4(b)). Such a process gradually stops as the ammonia complexation goes on and the role of the $\text{S}_2\text{O}_8^{2-}$ ions is progressively reduced. Then, Ni precipitation proceeds with the formation of a well-organized $\alpha\text{-Ni}(\text{OH})_2$ phase in the so-called self-ordered regime, through the reaction between Ni^{2+} and OH^- ions (reaction 1.4) [2.22]. $\alpha\text{-Ni}(\text{OH})_2$ growth is sustained by the release of OH^- ions by ammonia, which also plays a key role in shaping Ni-based nanowalls [2.23].

One can assume that $\alpha\text{-Ni}(\text{OH})_2$ phase is continuously produced, while NiOOH phase precipitates only in the first regime. Taking into account the exponential decay of the S/Ni ratio (Figure 2.9(c)), the random growth regime was modelled by the following equation

$$ds = k \exp(-t/\tau) \quad (2.2)$$

where s [nm] is the film thickness, t [s] is the growth time, k [nm s^{-1}] is the initial rate of reaction 1.10, and τ [s] is the time constant of the random growth regime.

When the oxidizing action of $\text{S}_2\text{O}_8^{2-}$ ions stops, film growth proceeds via the self-ordered regime. Since the growth kinetics curves in Figure 2.5 show a constant growth rate for the self-ordered regime, it was modelled by the following equation

$$ds = \beta dt \quad (2.3)$$

where β [nm s^{-1}] is a parameter related to the availability of free Ni^{2+} ions in solution. Combining equation 2.2 and 2.3, given that $s = 0$ at $t = 0$, it follows that the full growth kinetics can be described by the following equation

$$s(t) = \alpha (1 - \exp(t/\tau)) + \beta t \quad (2.4)$$

where $\alpha = kt$ [nm]. Figure 2.10 reports the film thickness measurements versus growth time at room temperature and 50°C and fits of data based on equation 2.4. Since the proposed model does not include the nucleation phase (0-260 s at room temperature), the fit of room temperature data starts at $t = 260$ s (i.e., room temperature data are shifted so that the point at 260 s becomes the (0,0) point).

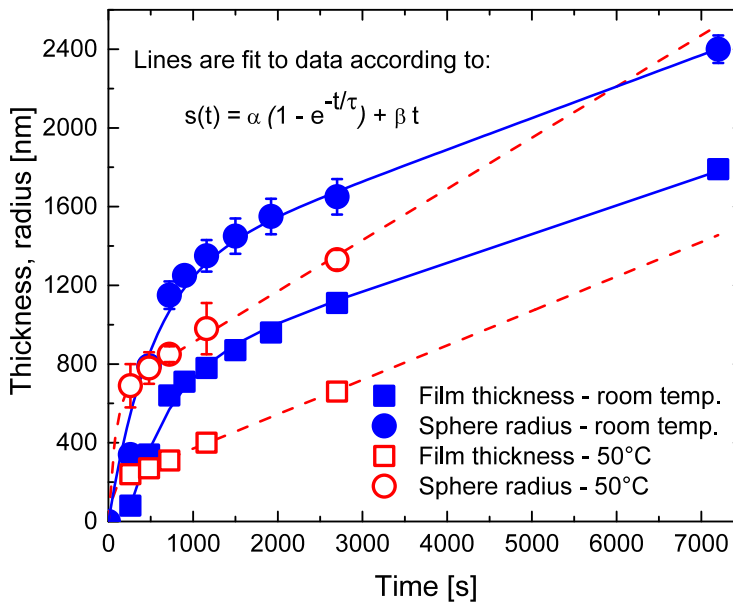


Figure 2.10: Film thickness (squares) and sphere radius (circles) versus growth time for the samples grown at room temperature (blue closed symbols) and 50°C (red open symbols). The lines represent the fits of data based on equation 2.4 [2.17].

As a matter of fact, the film surface as extracted from the bath is decorated with porous spheres resembling the same morphological

features of the film (Figure 2.11). Such spheres are a byproduct of the CBD, as they come from a homogenous nucleation in the bulk of the CBD solution, followed by a random landing on the film [2.14]. Figure 2.10 also reports the radius of the porous spheres versus growth time at room temperature and 50°C (growth kinetics curves were obtained by measuring the average radius of the spheres found onto film surface). The same model is able to describe spheres growth at the two temperatures. Actually, the growth of film or sphere is essentially a 1D or a 3D expression of the same process, which occurs in one direction for the film, or in all directions for the spheres. Still, these data help to understand the growth process.

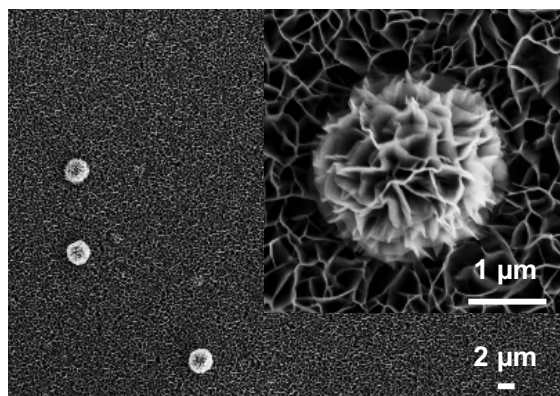


Figure 2.11: SEM images at different magnifications of RT-900, showing some porous spheres [2.17].

Table 2.1 reports the fit parameters of the four series of data. Focusing on film cases, the duration of the random regime is influenced by growth temperature. In fact, τ drops from 490 s at room temperature to 60 s or lower at 50°C. Instead, k , calculated as the ratio α/t , increases with growth temperature (1.42 nm s⁻¹ at room temperature and 3.25 nm s⁻¹ at 50°C), indicating that reaction 1.10 is much faster at higher temperature. On the other hand, the random regime lasts for shorter times at higher temperature, so its overall effect is less

Data	α [nm]	β [nm s ⁻¹]	τ [s]
Film thickness - Room temperature	695	0.145	490
Spheres radius - Room temperature	1250	0.160	500
Film thickness - 50°C	195	0.175	<60
Spheres radius - 50°C	650	0.260	<80

Table 2.1: Growth model parameters obtained from the fits of the data reported in Figure 2.10 based on equation 2.4 [2.17].

pronounced than at room temperature. Also, β , that is the rate of reaction 1.4, increases from 0.145 nm s⁻¹ at room temperature up to 0.175 nm s⁻¹ at 50°C, suggesting that Ni(OH)₂ self-ordered precipitation becomes faster with increasing temperature. When spheres growth is considered, β changes from 0.160 nm s⁻¹ at room temperature to 0.260 nm s⁻¹ at 50°C, with a thermal increase more pronounced than for the film. Actually, Ni precipitation mechanism is limited by the diffusion and reaction processes, both thermally activated. The values of β obtained for film growth at room temperature are quite similar to those found for spheres growth at the same temperature. Since the diffusion extent for the spheres is always larger than for the film (where reactants come only in one direction), this indicates that the self-ordered regime should be reaction-limited at room temperature. At 50°C the value of β for the spheres growth is much higher than that for the film growth. Therefore, at higher temperatures, the self-ordered regime seems to be diffusion-limited. Such a conclusion indicates that a self-ordered growth at higher temperatures should produce better material in terms of chemical bonds and surroundings. In the following, the electrochemical properties of Ni-based nanowalls grown at different temperatures are investigated and then applied for the non-enzymatic glucose sensing.

2.3.3 Electrochemical properties

The relationship between Ni-based nanowalls morphology and electrochemical properties was investigated by using RT-480 and 50-480, both ~ 300 nm thick and grown on ITO substrates. Indeed, RT-480 is made of random oriented nanosheets, while 50-480 is made of vertically ordered nanosheets (Figures 2.4(b) and (c)). Therefore, these samples allow to distinguish of the effect of the nanosheets shape on the electrochemical properties. CV was performed until stable curves were obtained (~ 30 CV cycles for both samples). Figure 2.12(a) compares the CV curves of RT-480 and 50-480. In both cases a pair of

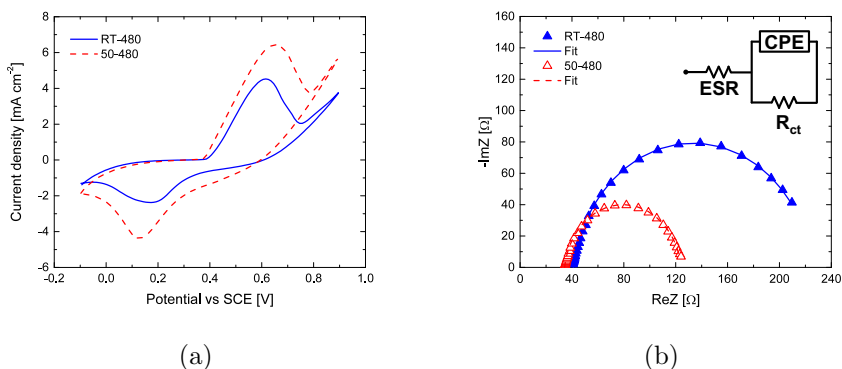


Figure 2.12: (a) CV curves of RT-480 (blue solid line) and 50-480 (red dashed line) recorded at 50 mV s^{-1} scan rate in the potential range $-0.1 \div 0.9 \text{ V}$ in 0.1 M NaOH . (b) Nyquist plots of RT-480 (blue closed triangles) and 50-480 (red open triangles) recorded at the oxidation potential with a 20 mV superimposed sinusoidal voltage in the frequency range $10^2 \div 10^{-2} \text{ Hz}$ in 0.1 M NaOH . Lines are fits of Nyquist plots based on the reported equivalent circuit model [2.17].

redox peaks can be observed at $\sim 0.17 \text{ V}$ (reduction peak) and $\sim 0.62 \text{ V}$ (oxidation peak), caused by the reversible redox reaction $\text{Ni}^{2+}/\text{Ni}^{3+}$ in alkaline solution (equation 1.1). Moreover, it can be seen that the

Sample	ESR [Ω]	R_{ct} [Ω]	CPE [$F s^{(n-1)}$]	n [s]
RT-480	185	0.0056	490	0.90
50-480	34	90	0.0127	0.93
RT-480 NF	34	1780	0.0016	0.87
50-480 NF	38	840	0.0031	0.86
50-1200 NF_Ni_foam	18	36	0.0382	0.77

Table 2.2: Circuit parameters obtained from the fits of samples Nyquist plots [2.17].

area enclosed by the CV of 50-480 is larger than RT-480. Given their similar thicknesses, such a datum suggests a better charge storage capability for the film grown at higher temperature [2.22].

EIS was carried out to investigate the impedance behaviour of the random and self-ordered nanosheets. The Nyquist plots (imaginary versus real part of the impedance) of RT-480 and 50-480 are compared in Figure 2.12(b). Both curves show a semicircular shape, which can be described by the Randles circuit reported in Figure 2.12(b). This model includes an equivalent series resistance (ESR), which is the combined resistance of electrolyte and internal resistance of the sample, connected in series with the double layer capacitance in parallel with the charge-transfer resistance of the electrode (R_{ct}) [2.24]. To account for the non-ideal capacitive behaviour of the sample, the double layer capacitor was replaced by a constant phase element (CPE), with n being an ideality factor. The experimental data were successfully fitted with this model to obtain the circuit parameters reported in Table 2.2 (note that the data of RT-480 NF, 50-480 NF and 50-1200 NF_Ni_foam samples will be discussed later). The value of ESR is almost the same for the two samples, as expected. R_{ct} decreases from 185 Ω (RT-480) to 90 Ω (50-480). Since

film thickness is almost the same for the two samples, this result suggests that the self-ordered nanosheets (50-480) are able to sustain a charge transfer rate about twice that of the random nanosheets (RT-480). This datum agrees with the above observation that the higher growth temperature should produce better material.

2.3.4 Glucose detection performances

RT-480 and 50-480 grown on ITO substrates were then employed for non-enzymatic glucose sensing, to test if the improved growth kinetics can affect some real applications. Iwu et al. showed that Ni-based nanowalls can be converted to Ni nanofoam upon annealing in reducing atmosphere, leading to a more stable electrode and higher glucose sensitivity [2.14]. Therefore, RT-480 and 50-480 were annealed to obtain Ni nanofoam samples (RT-480 NF and 50-480 NF), finding that film thickness reduces, as already reported by Iwu, and the random and/or self-ordered configuration are preserved. In addition, to investigate the effect of the substrate on the glucose sensing performances, the Ni nanofoam was realized also on Ni foam substrate by CBD at 50°C for 1200 s, followed by reducing annealing. The resulting sample, labelled 50-1200 NF_Ni-foam, is shown in Figure 2.13.

All Ni nanofoam samples were conditioned for glucose sensing by CV, until stable curves were obtained. In this way, a very thin outer layer of the active $\text{Ni}(\text{OH})_2/\text{NiOOH}$ species is formed. CV curves of RT-480 NF and 50-480 NF (Figure A2(a)) show that the oxidation potential is the same (~ 0.55 V) and lower than before annealing (Figure 2.12(a)). The peak current density reduces, too. However, CV curve of 50-480 NF still encloses the largest area.

By comparing the Nyquist plots of the two samples, still 50-480 NF exhibits a lower impedance than RT-480 NF (Figure A2(b)). In particular, R_{ct} of 50-480 NF is still half than RT-480 NF (Table 2.2), as it occurs before annealing. However, R_{ct} values are one order of magnitude greater than Ni-based nanowalls. This result could be explained by the detrimental effect of the reducing annealing on

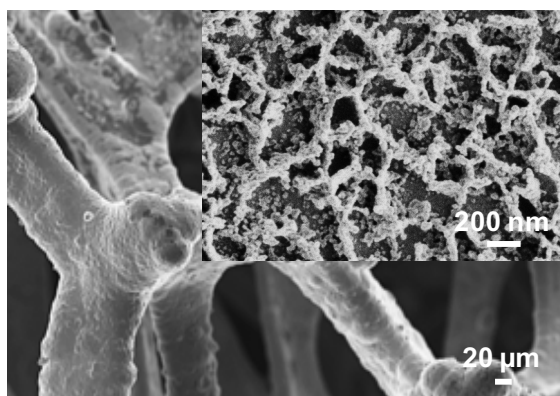


Figure 2.13: SEM images at different magnification of 50-1200 NF_Ni_foam [2.17].

ITO substrates. Instead, R_{ct} of 50-1200 NF_Ni-foam (Nyquist plot in Figure A3) is ~ 20 times smaller than 50-480 NF. This improvement could be ascribed to the larger area of the Ni foam substrate (1×1 cm² Ni foam is ~ 3 times larger than 1×1 cm² flat substrate), to the better electrical contact and to the prolonged CBD at 50°C, leading to a thicker film.

CA analysis was employed to test the non-enzymatic glucose sensing performances of Ni nanofoam samples. The calibration curves of RT-480 NF and 50-480 NF (Figure A4) indicated that the sensitivity of 50-480 NF ($1.03 \text{ mA mM}^{-1} \text{ cm}^{-2}$) is almost double than RT-480 NF ($0.64 \text{ mA mM}^{-1} \text{ cm}^{-2}$). This result can be attributed to the superior electrochemical properties of the self-ordered nanosheets evidenced by CV and EIS analyses.

Figure 2.14 reports the amperometric response and calibration curve of 50-1200 NF_Ni-foam, showing an unprecedentedly high glucose sensitivity of $31 \text{ mA mM}^{-1} \text{ cm}^{-2} \text{ mM}^{-1}$ in the glucose concentration range $0.02 \div 0.4 \text{ mM}$. To evaluate the contribution of the Ni foam substrate, the inset in Figure 2.14 reports also the calibration curve of a bare Ni foam substrate whose surface was activated by CV. The sensitivity is much smaller ($2.3 \text{ mA mM}^{-1} \text{ cm}^{-2}$) than 50-1200

NF_Ni-foam, demonstrating the dominant role of the Ni nanofoam. Moreover, 50-1200 NF_Ni-foam showed a $5 \mu\text{M}$ LoD, calculated by assuming $S/N = 3$, and a quick response to glucose (1-2 s).

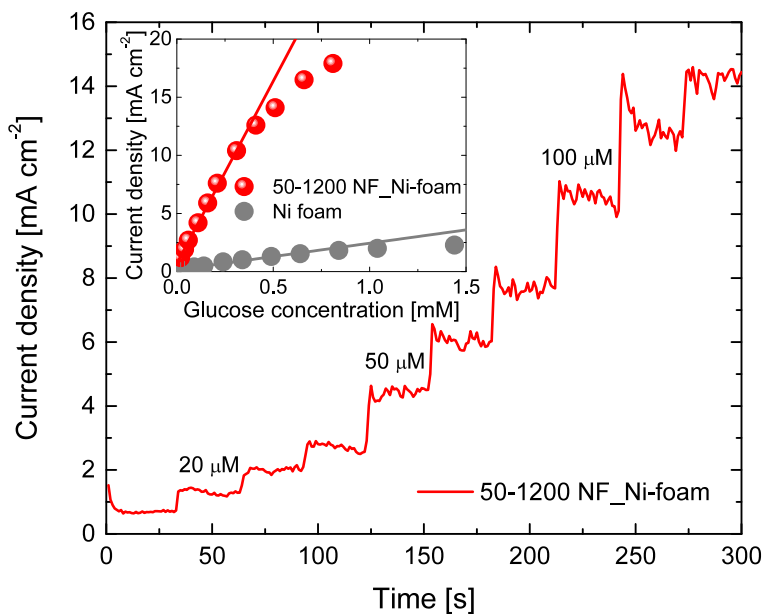


Figure 2.14: Amperometric response of 50-1200 NF_Ni-foam with successive glucose additions at 30 s time intervals in 0.1 M NaOH. The inset compares the calibration curves of 50-1200 NF_Ni-foam (red spheres) and a bare Ni foam substrate activated by CV (grey circles). The error bars are of the same size as the symbols [2.17].

Table 2.3 compares the performances of recent non-enzymatic glucose sensors based on Ni nanostructures deposited onto Ni foam substrate. The sensitivity of 50-1200 NF_Ni-foam is much higher than those previously obtained with NiO nanostructures on Ni foam (6.7

$\text{mA mM}^{-1} \text{ cm}^{-2}$ in [2.12], $3.2 \text{ mA mM}^{-1} \text{ cm}^{-2}$ in [2.13]). Despite the Ni foam presence (which still contributes to the glucose oxidation), the much higher sensitivity reported here is attributed to the optimization of the nanostructure shaping obtained through the 50°C CBD and to the nanowalls \rightarrow nanofoam transformation. The linear response range is sufficiently wide for the detection of glucose in concentrations as low as those present in human saliva and tears.

Year	Electrode material	Fabrication	Sensitivity [$\text{mA cm}^{-2} \text{mM}^{-1}$]	Linear range [mM]	Response time [s]	LoD [μM]	Ref.
2013	NiO on Ni foam	Electrodeposition + annealing	6.7	0.005÷5.5	3	0.46	[2.12]
2016	NiO on RGO coated Ni foam	Electrodeposition + aqueous deposition + annealing	3.2	0.01÷0.2	2	0.1	[2.13]
2018	Ni nanofoam on Ni foam	CBD + annealing + CV	31	0.02÷0.4	1-2	5	[2.17]

Table 2.3: Non-enzymatic glucose sensing performances of recent Ni-based nanostructures on Ni foam [2.17].

2.4 Conclusions

In this chapter, the growth mechanism of Ni-based nanowalls obtained by chemical bath deposition was investigated as function of growth time (60-7200) and temperature (room temperature and 50°C). Two growth regimes were observed: (i) a random regime with a fast precipitation of random oriented and irregular NiOOH·Ni(OH)₂ nanosheets, followed by (ii) a self-ordered regime with a slower precipitation of vertically-aligned and self-ordered α -Ni(OH)₂ nanosheets. While the self-ordered regime seems endless, the random regime has a time duration which reduces with increasing temperature. During the first regime a S incorporation occurs and a key role is played by the K₂S₂O₈ at the very early stage of the CBD, being a fundamental precursor for the precipitation of Ni-based nanowalls. The growth kinetics was satisfactorily modelled assuming the above two regimes, with the results that at 50°C the growth seems to be diffusion-limited, leading to a better material in terms of chemical bonds and surroundings. The redox transition Ni²⁺/Ni³⁺ of Ni-based nanowalls was tested on proper electrodes by using CV and EIS analyses. It was found that the samples obtained at higher growth temperature ensure better charge storage capability and higher charge transfer rate, confirming the superior growth method. Ni-based nanowalls were also applied to non-enzymatic glucose detection after a proper thermal treatment at 350°C in reducing atmosphere, leading to a porous structure formed by Ni nanoparticles (20-30 nm in size), called Ni nanofoam. The higher growth temperature still affects the electrochemical performances as the glucose sensitivity is doubled in the sample fabricated by CDB at 50°C. After such an optimization, Ni nanofoam was grown on Ni foam substrate, reaching an unprecedentedly high glucose sensitivity of 31 mA cm⁻² mM⁻¹ in the linear range 0.02÷0.4 mM, a very low limit of detection of 5 μ M and a quick response to glucose (1-2 s). Moreover, as previously reported, Ni nanofoam ensures high selectivity to glucose against common interfering species (200 μ M glucose versus 20 μ M uric acid, 10 μ M ascorbic

acid and 10 μM acetaminophen) as well as high stability (4% response loss after 64 days). These impressive performances open the route towards non-invasive glucose detection in human saliva and tears.

References

- [2.1] K. Tian, M. Prestgard, and A. Tiwari, A review of recent advances in nonenzymatic glucose sensors, *Materials Science and Engineering: C* **41**, 100 (2014).
- [2.2] <https://www.idf.org>.
- [2.3] www.diabetes.org.
- [2.4] <https://www.google.com>.
- [2.5] K. E. Toghill and R. G. Compton, Electrochemical Non-Enzymatic Glucose Sensors: A Perspective and an Evaluation, *International Journal of Electrochemical Science* **5**, 1246 (2010).
- [2.6] X. Strakosas, J. Selberg, P. Pansodtee, N. Yonas, P. Manapongpun, M. Teodorescu, and M. Rolandi, A non-enzymatic glucose sensor enabled by bioelectronic pH control, *Scientific Reports* **9**, 10844 (2019).
- [2.7] C.-W. Kung, Y.-H. Cheng, and K.-C. Ho, Single layer of nickel hydroxide nanoparticles covered on a porous Ni foam and its application for highly sensitive non-enzymatic glucose sensor, *Sensors and Actuators B: Chemical* **204**, 159 (2014).
- [2.8] H. Li, C.-Y. Guo, and C.-L. Xu, A highly sensitive non-enzymatic glucose sensor based on bimetallic Cu–Ag superstructures, *Biosensors and Bioelectronics* **63**, 339 (2015).

- [2.9] M. Li, X. Bo, Y. Zhang, C. Han, and L. Guo, One-pot ionic liquid-assisted synthesis of highly dispersed PtPd nanoparticles/reduced graphene oxide composites for nonenzymatic glucose detection, *Biosensors and Bioelectronics* **56**, 223 (2014).
- [2.10] Z. Ibupoto, K. Khun, V. Beni, X. Liu, and M. Willander, Synthesis of Novel CuO Nanosheets and Their Non-Enzymatic Glucose Sensing Applications, *Sensors* **13**, 7926 (2013).
- [2.11] R. A. Soomro, Z. H. Ibupoto, M. I. Abro, and M. Willander, Electrochemical sensing of glucose based on novel hedgehog-like NiO nanostructures, *Sensors and Actuators B: Chemical* **209**, 966 (2015).
- [2.12] C. Guo, Y. Wang, Y. Zhao, and C. Xu, Non-enzymatic glucose sensor based on three dimensional nickel oxide for enhanced sensitivity, *Analytical Methods* **5**, 1644 (2013).
- [2.13] B. Zhao, T. Wang, L. Jiang, K. Zhang, M. M. F. Yuen, J.-B. Xu, X.-Z. Fu, R. Sun, and C.-P. Wong, NiO mesoporous nanowalls grown on RGO coated nickel foam as high performance electrodes for supercapacitors and biosensors, *Electrochimica Acta* **192**, 205 (2016).
- [2.14] K. O. Iwu, A. Lombardo, R. Sanz, S. Scirè, and S. Mirabella, Facile synthesis of Ni nanofoam for flexible and low-cost non-enzymatic glucose sensing, *Sensors and Actuators B: Chemical* **224**, 764 (2016).
- [2.15] S. Petralia, S. Mirabella, V. Strano, and S. Conoci, A Miniaturized Electrochemical System Based on Nickel Oxide Species for Glucose Sensing Applications, *Bionanoscience* **7**, 58 (2017).
- [2.16] G. Impellizzeri, S. Mirabella, and M. G. Grimaldi, Ion implantation damage and crystalline-amorphous transition in Ge, *Applied Physics A* **103**, 323 (2011).

- [2.17] M. Urso, G. Pellegrino, V. Strano, E. Bruno, F. Priolo, and S. Mirabella, Enhanced sensitivity in non-enzymatic glucose detection by improved growth kinetics of Ni-based nanostructures, *Nanotechnology* **29**, 165601 (2018).
- [2.18] S.-Y. Han, D.-H. Lee, Y.-J. Chang, S.-O. Ryu, T.-J. Lee, and C.-H. Chang, The Growth Mechanism of Nickel Oxide Thin Films by Room-Temperature Chemical Bath Deposition, *Journal of the Electrochemical Society* **153**, C382 (2006).
- [2.19] C. G. Morales-Guio, M. T. Mayer, A. Yella, S. D. Tilley, M. Grätzel, and X. Hu, An Optically Transparent Iron Nickel Oxide Catalyst for Solar Water Splitting, *Journal of the American Chemical Society* **137**, 9927 (2015).
- [2.20] X. H. Xia, J. P. Tu, J. Zhang, X. L. Wang, W. K. Zhang, and H. Huang, Electrochromic properties of porous NiO thin films prepared by a chemical bath deposition, *Solar Energy Materials and Solar Cells* **92**, 628 (2008).
- [2.21] G. Meyer, D. Naumann, and L. Wesemann, *Inorganic Chemistry in Focus III* (Wiley, 2006).
- [2.22] Q. Ke, M. Zheng, H. Liu, C. Guan, L. Mao, and J. Wang, 3D TiO₂@Ni(OH)₂ Core-Shell Arrays with Tunable Nanostructure for Hybrid Supercapacitor Application, *Scientific Reports* **5**, 13940 (2015).
- [2.23] G. Li, X. Wang, L. Liu, R. Liu, F. Shen, Z. Cui, W. Chen, and T. Zhang, Controllable Synthesis of 3D Ni(OH)₂ and NiO Nanowalls on Various Substrates for High-Performance Nanosensors, *Small* **11**, 731 (2015).
- [2.24] J. E. B. Randles, Kinetics of rapid electrode reactions, *Discussions of the Faraday Society* **1**, 11 (1947).

Chapter 3

Au decorated NiO nanowalls for PCR-free *Mycoplasma agalactiae* sensing

Contents

3.1	Contagious Agalactia	84
3.2	Materials and methods	89
3.2.1	Synthesis	89
3.2.2	Characterization	91
3.3	Au decorated NiO nanowalls	92
3.3.1	Morphological and chemical characteriza- tion	92
3.3.2	<i>Mycoplasma agalactiae</i> DNA sensing . . .	94
3.4	Conclusions	99
	References	100

Contagious Agalactia (CA) is an infectious disease of small ruminants (goats and sheep), endemic in the Mediterranean countries,

caused by the *Mycoplasma agalactiae* (*Ma*). *Ma* is responsible for a severe reduction and even suppression of the milk production, and occasionally can lead to abortion and death of lambs or kids. Due to its morbidity, CA can rapidly spread in the whole flock, causing serious economic losses for farmers. Therefore, a rapid diagnosis of CA is very important. Routinary diagnostics is mainly based on isolation of the pathogen in selective media, on serological tests and on direct identification of the pathogen DNA using Polymerase Chain Reaction (PCR)-based methods. However, these methods represent time consuming, costly and complex procedures because of the slow *Ma* growth, the risk of cross-contamination with other species of *Mycoplasma*, the presence of inhibitors in milk samples which interfere with the reaction, and the low detection limit levels. Recently, PCR-free DNA biosensors have attracted increasing attention due to their rapid, simple and economical testing. In this chapter, a low-cost electrochemical *Ma* DNA sensor based on Au decorated NiO nanowalls is reported. Au decoration was conducted by Au electroless deposition on NiO nanowalls grown by chemical bath deposition and thermal annealing, and characterized by scanning electron microscopy (SEM), energy-dispersive X-ray spectroscopy (EDX) and electrochemical impedance spectroscopy (EIS). *Ma* probe ssDNA, functionalized with a fluorescent dye (Cy3), was successfully immobilized onto Au decorated NiO nanowalls surface, as confirmed by fluorescent microscopy. Then, the complementary *Ma* ssDNA ($1.7\text{-}48.5\text{ ng }\mu\text{l}^{-1}$) was detected upon DNA hybridization by monitoring the impedance of Au decorated NiO nanowalls. The reported synthesis method as well as the promising performances of Au decorated NiO nanowalls open the route towards cheap and fast PCR-free detection of *Ma*.

3.1 Contagious Agalactia

Contagious Agalactia (CA) is an infectious disease of small ruminants, such as goats and sheep, characterized by mastitis, arthritis

Mycoplasma agalactiae (Ma) is the principal aetiological agent of CA in sheep, while other mycoplasmas are pathogenic in goats. Mycoplasmas are one of the smallest self-replicating bacteria [3.7]. They have a small genome (0.58-1.4 Mbp), which codes for proteins involved in metabolic and enzymatic activities, and also phase-variable lipoproteins allowing them to evade the host immune system and persist for long periods [3.8]. The principal sources of Ma infection are the ingestion of contaminated feed, water or milk. Then, Ma easily propagates in the flock by contact between infected and healthy animals [3.5].

The primary diagnosis of CA is based on the observation of clinical signs, however the presence of many other diseases in endemic areas typically makes it more complicate [3.9]. The timely identification of CA is essential to prevent its diffusion. Therefore, there is an urgent need for sensitive, selective and rapid diagnostic methods for CA early detection.

The routine analysis method for isolating and identifying Ma in clinical samples involves Ma culture in liquid or solid media. However, this is a very complicate and time consuming method (7-10 days) because of the slow Ma growth [3.7]. Various serological tests have been used to identify Ma, but they have poor selectivity [3.9].

Recently, sensitive, selective and rapid tests for Ma identification have been developed, driven by the great advances in molecular biology and biotechnology. Among them, those based on Ma DNA amplification by Polymerase Chain Reaction (PCR) are the most reliable and used ones [3.9].

PCR-based methods allow to exponentially amplify a specific DNA segment (gene), generating from thousands to millions of copies by several cycles (Figure 3.2). PCR products are subjected to electrophoresis and/or filtered by an appropriate membrane and exposed to a solution containing a probe DNA for hybridization, which is chemically or enzymatically labelled with radioactive and chemiluminescent materials or ligands, since the DNA itself is not able to provide any signal [3.10]. The selectivity of PCR strongly depends

on the gene to be amplified, which has to be carefully chosen (typically Ma 16S rRNA gene) [3.9].

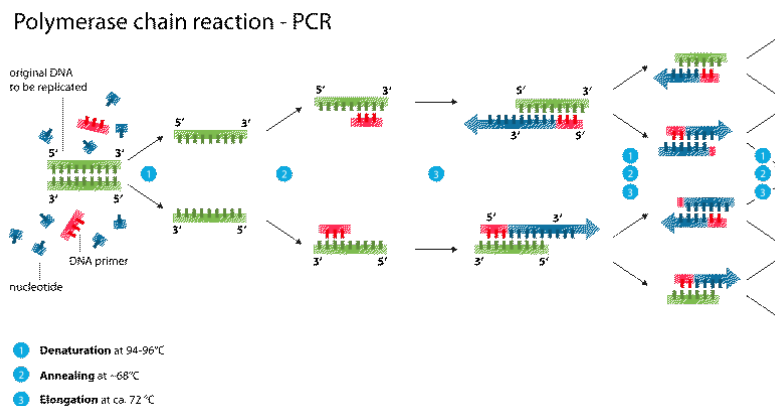


Figure 3.2: Schematic illustration of a complete PCR cycle [3.11]

Among the PCR-based methods, real-time PCR, i.e. the monitoring of gene amplification during PCR rather than at the end of PCR, is the most sensitive and quick method, being also automated [3.9]. For example, Oravcová et al. performed the real-time PCR of Ma p40 gene [3.5]. Nevertheless, all PCR-based methods are limited by their high cost, use of carcinogenic agents, contamination of the laboratory by nucleic acids and strong dependence on probe DNA, hybridization conditions, type of membrane, labelling, and environment [3.12]. Therefore, simple, rapid, low-cost, sensitive and selective PCR-free methods for Ma detection are needed. Such a way could also replace the analysis into a specialized laboratory with a quick test in farm.

The detection of DNA hybridization ensures high selectivity because of the intrinsic specificity of DNA base pairing [3.13]. As a result, a wide variety of DNA hybridization sensors have been reported, based on optical, electrochemical and piezoelectric transducers. Among them, electrochemical sensors are the most advantageous

ones as a rapid, sensitive, selective, and cost/energy-saving technology [3.14]. Typically, electrochemical sensors consist of a solid electrode, where probe ssDNA is immobilized via physical absorption, self-assembly or covalent conjugation. Upon hybridization of probe ssDNA and complementary ssDNA [3.10], a signal is generated whose amplitude determines the sensitivity of the electrochemical sensor [3.13]. Therefore, various electrochemical techniques have been used to enhance the hybridization signal, leading to a further classification of electrochemical sensors in voltammetric, amperometric, coulometric and impedimetric sensors [3.15]. In particular, electrochemical impedance spectroscopy (EIS) allows to detect the variations of the impedance at the electrode/electrolyte interface during both probe ssDNA immobilization and hybridization with complementary ssDNA [3.16]. The impedance can be measured at several frequencies or at a single frequency by using a very small amplitude sinusoidal voltage without significantly disturbing the properties being measured [3.15, 17].

The probe ssDNA immobilization represents a fundamental step of the sensor fabrication. In fact, it has been demonstrated that the sensing performances (sensitivity, selectivity, stability, etc.) depend mainly on the immobilized probe ssDNA (binding method, conformation, orientation, surface density, etc.) [3.18]. Probe DNA can be immobilized through various approach, such as adsorption, avidin (or streptavidin)-biotin interactions and covalent bonds. In particular, the most used approach is based on the strong covalent bond between Au and S, which easily allows to bind thiolated (SH terminal group) probe ssDNA onto the surface of Au-based electrodes, forming a self-assembled monolayer (SAM) of ssDNA with high stability, compactness and orderliness. This approach is typically performed in buffer solutions where the electrostatic repulsions between a ssDNA fragment (which is negatively charged due to DNA phosphate groups) and the other ssDNA fragments and cations push the ssDNA onto the surface of the electrode [3.19, 20].

Au decoration of nanostructured thin films by electroless deposi-

tion (ELD) represents a simple and low-cost method to fabricate high surface area Au electrodes for probe ssDNA immobilization. ELD is based on reduction reactions which occur in aqueous solution without external electrical power, leading to the conformal deposition of metals on various substrates, including insulating materials [3.21]. In particular, Au decoration of NiO nanowalls grown by chemical bath deposition (CBD) and thermal annealing represents a promising approach to fabricate a low-cost impedimetric sensor to detect Ma DNA hybridization.

3.2 Materials and methods

Ma DNA sensor fabrication and sensing experiments were performed at the Tel Aviv University (Tel Aviv, Israel) under the supervision of prof. Yosi Shacham-Diamand and prof. Adi Avni.

3.2.1 Synthesis

Au coated substrates ($1 \times 1.5 \text{ cm}^2$, consisting of 50 nm thick Au layer on 15 nm thick Ti adhesion layer deposited by evaporation onto 100 nm thick SiO_2 layer on Si substrate, cut from Czochralski wafer) and Ni foam substrates ($1 \times 1.5 \text{ cm}^2$, Goodfellow, thickness 1.6 mm, porosity 95%, 20 pores cm^{-1}) were rinsed with acetone, isopropanol and deionized water (MilliQ, 18 $\text{M}\Omega \text{ cm}$), and dried under N_2 gas flow. Ni(OH)_2 nanowalls were grown on cleaned substrates by CBD. Solution composition for CBD was 0.42 M $\text{NiSO}_4 \cdot 6\text{H}_2\text{O}$ (Alfa Aesar, 98%), 0.07 M $\text{K}_2\text{S}_2\text{O}_8$ (Alfa Aesar, 97%) and 3.5 wt% ammonia (Merck, 30-33 wt% NH_3 in H_2O). The solution was heated up to 50°C and kept at this temperature through a bain-marie configuration [3.22]. Substrates were immersed ($1 \times 1 \text{ cm}^2$ area) in the solution for 20 min, and then rinsed with deionized water to remove unwanted microparticulate and dried under N_2 gas flow. Ni(OH)_2 nanowalls were further annealed at 350°C for 60 min in vacuum to obtain NiO nanowalls.

Prior to Au ELD, NiO nanowalls were immersed for 10 min in 7.5% v/v% hydrazine hydrate (Sigma-Aldrich, 50-60 v/v% N₂H₄ in H₂O) at room temperature, and rinsed with deionized water. Solution composition for Au ELD was 2 g l⁻¹ potassium dicyanoaurate (KAu(CN)₂, Sigma-Aldrich, 98%), 45 g l⁻¹ trisodium citrate dihydrate (Na₃C₆H₅O₇·2H₂O, Sigma-Aldrich), 70 g l⁻¹ ammonium chloride (NH₄Cl, Sigma-Aldrich, ≥99.5 %), 8 g l⁻¹ sodium hypophosphite monohydrate (NaH₂PO₂·H₂O, Merck, ≥99 %). Solution pH was adjusted to 7.5, then the solution was heated up to 80°C and kept at this temperature through a bain-marie configuration. NiO nanowalls were immersed in the solution for different durations (15 s, 1 and 3 min) to obtain Au decorated NiO nanowalls samples, and then rinsed with deionized water and dried under N₂ gas flow.

Ma thiolated probe ssDNA had the 25-base sequence Thiol-C6-TGT GAT AAG AAC GAA AAT TCA CAA A (Hylabs, HPLC, 8990 Da molecular weight), eventually modified with a cyanine (Cy3) on 3' end (Hylabs, HPLC, 9577 Da molecular weight). Solution composition for probe ssDNA immobilization was 1X TE buffer, consisting of 10 mM Tris (tris(hydroxymethyl)aminomethane, C₄H₁₁NO₃, Sigma-Aldrich, ≥99.8%) and 1 mM EDTA (ethylenediaminetetraacetic acid, C₁₀H₁₆N₂O₈, Sigma-Aldrich, ≥99%), 40 mM sodium chloride (NaCl, Sigma-Aldrich, ≥99.5 %), 5 mM magnesium chloride (MgCl₂, Sigma-Aldrich, ≥98%), 4.5 μM Ma thiolated probe ssDNA and 0.5 μM Cy3-modified Ma thiolated probe ssDNA. The DNA immobilization was performed by keeping Au decorated NiO nanowalls in the solution for 5 h at room temperature under stirring (100 rpm). Samples were then rinsed with deionized water and dried under N₂ gas flow.

Non-complementary ssDNA for prehybridization had the 30-base sequence ATG GTC TCA CTG CTC TGC ACC AGC GGG GAA (Hylabs, 9168 Da molecular weight). Prehybridization was performed by keeping the samples (Au decorated NiO nanowalls with immobilized Ma probe ssDNA) for 1-5 h at 40°C in phosphate buffer solution (PBS, pH 7) containing 12 μM non-complementary ssDNA.

Ma complementary ssDNA for hybridization had the 25-base se-

quence TTT GTG AAT TTT CGT TCT TAT CAC A (Hylabs, desalted, 8510 Da molecular weight). Hybridization was performed by keeping the samples (Au decorated NiO nanowalls with immobilized Ma probe ssDNA and 5 h prehybridization) for 1 h at 40°C in PBS (pH 7) containing different concentrations ($\sim 1.7, 4.3, 12.8, 21.3 \text{ ng } \mu\text{l}^{-1}$) of Ma complementary ssDNA. Note that the Ma dsDNA formed by the hybridization of Ma thiolated probe ssDNA and Ma complementary ssDNA was not denatured after each experiments, therefore the sensor response was evaluated for $\sim 1.7, 6, 14.5, 27.2, 48.5 \text{ ng } \mu\text{l}^{-1}$ Ma complementary ssDNA.

3.2.2 Characterization

The surface morphology of samples was characterized by a scanning electron microscope (Gemini field emission SEM Carl Zeiss SUPRA 25) combined with energy dispersive X-ray spectroscopy (EDX). Cy3 fluorescence was observed by a confocal microscope with a $\sim 510 \text{ nm}$ excitation wavelength.

EIS was performed using a potentiostat (BioLogic VSP) and a three-electrode setup with a Pt counter electrode, a commercial silver chloride reference electrode (Ag/AgCl), and the samples as working electrodes ($1 \times 1 \text{ cm}^2$ immersed area). All measurements were performed at room temperature in PBS (pH 7) containing 10 mM ferri-ferrocyanide ($[\text{Fe}(\text{CN})_6]^{3-/4-}$, Sigma-Aldrich, $\geq 99\%$) as supporting electrolyte. EIS measurements were carried out at 0 V versus open circuit potential with 10 mV superimposed sinusoidal voltage in the frequency range $10^6 \div 10^{-1} \text{ Hz}$. EIS measurements were repeated at least 3 times for each experiment.

3.3 Au decorated NiO nanowalls

3.3.1 Morphological and chemical characterization

Figure 3.3 shows the schematic illustration of the different steps to fabricate the Ma DNA sensor.

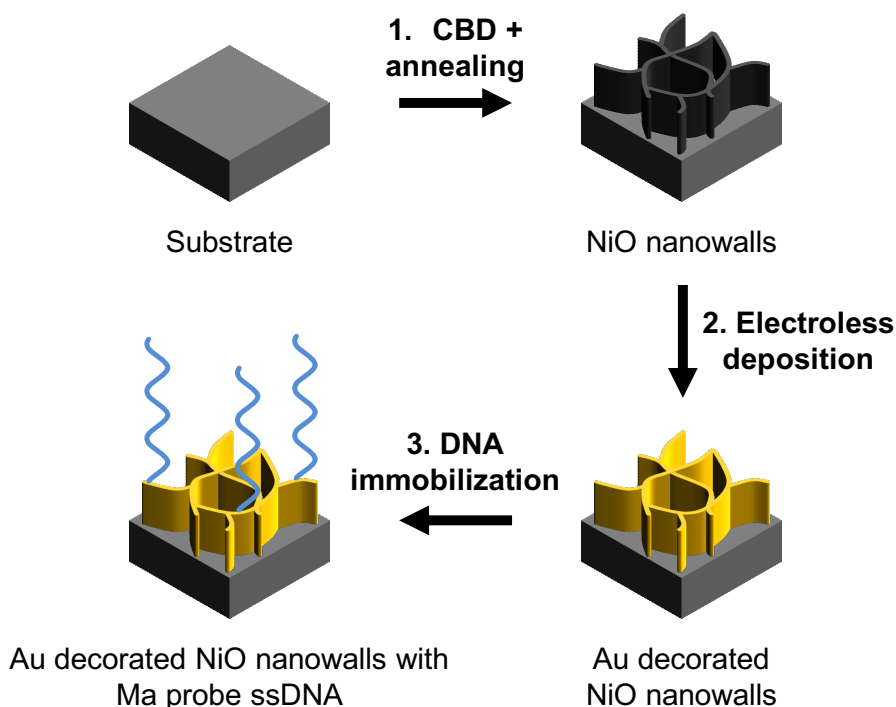


Figure 3.3: Schematic illustration of the various fabrication steps of the Ma DNA sensor based on Au decorated NiO nanowalls.

First, NiO nanowalls were grown by CBD and thermal annealing in vacuum. No variations in nanowalls morphology were observed by using SEM after the annealing process.

Then, Au ELD was carried out for different durations: 15 s, 1 and 3 min. Despite the colour of NiO nanowalls turned from brown/black to yellow/gold after only 15 s, suggesting Au deposition, SEM analysis did not evidence any appreciable change in nanowalls morphology even after 3 min of Au ELD (Figure 3.4(a)). Nevertheless, Au presence was unambiguously proved in the EDX spectrum of NiO nanowalls sample prepared on Ni foam substrate and subjected to 3 min Au ELD (Figure 3.4(b)).

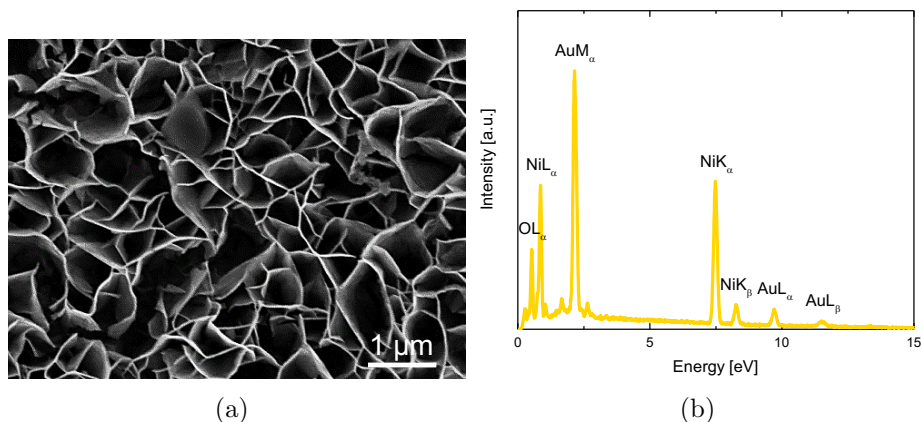


Figure 3.4: (a) Plan-view SEM image and (b) EDX spectrum of Au decorated NiO nanowalls (3 min ELD) on Ni foam substrate.

Finally, Ma thiolated probe ssDNA was immobilized on Au decorated NiO nanowalls samples grown on Au substrates, and Cy3 fluorescence was checked by using a confocal microscope to attest the DNA immobilization. The same procedure was also applied for a bare NiO nanowalls sample. No Cy3 fluorescence was observed in NiO nanowalls and Au decorated NiO nanowalls obtained by 15 s and 1 min ELD. Instead, Au decorated NiO nanowalls obtained by 3 min ELD showed a bright and uniform fluorescence over the entire area covered by the nanowalls (Figure 3.5(a)). In particular, Figure 3.5(a) shows the plan-view micrograph of the interface between the region with and without Au decorated NiO nanowalls.

The fluorescence in Au decorated NiO nanowalls is so bright that the Au substrate appears black, suggesting no DNA immobilization. Actually, this results demonstrates that having a high surface area Au nanostructure rather than a flat Au surface allows to immobilize much more DNA. The successful DNA immobilization was also confirmed by the uniform presence of bubble-like structures (10-20 nm in size) onto both sides of Au decorated NiO nanowalls (Figure 3.5(b)). This result is in agreement with Guler et al. who immobilized ssDNA on polypyrrole-coated electrospun poly(ϵ -caprolactone) nanofibers, observing an increase in nanofibers surface roughness and diameter after ssDNA immobilization process [3.17].

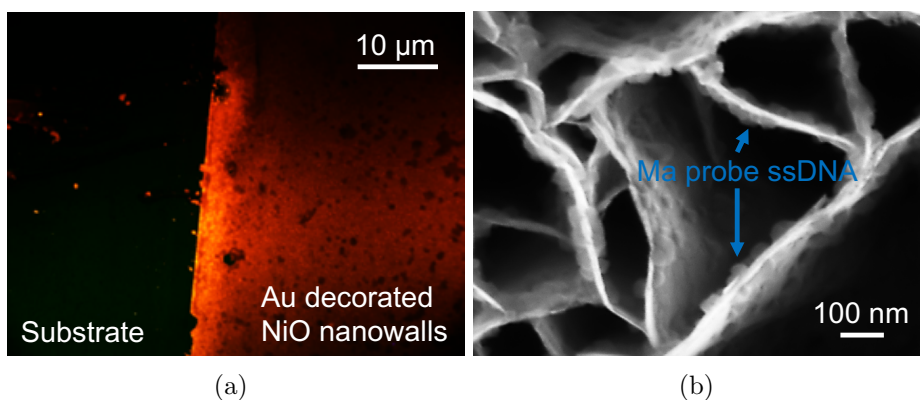


Figure 3.5: (a) Confocal microscopy and (b) SEM image of Au decorated NiO nanowalls (3 min ELD) on Au substrate after Cy3-functionalized Ma thiolated probe ssDNA immobilization.

3.3.2 Mycoplasma agalactiae DNA sensing

EIS was carried out at the end of each sensor fabrication step (CBD, Au ELD and Ma thiolated probe ssDNA immobilization), and Figure 3.6 shows the recorded Bode plots of NiO nanowalls, Au decorated NiO nanowalls and Au decorated NiO nanowalls with Ma probe ss-

DNA. In particular, Figure 3.6(a) reports impedance modulus $|Z|$ [Ω] versus frequency, while Figure 3.6(b) reports impedance phase $[\circ]$ versus frequency). Bode plots were preferred to Nyquist plot since they show the frequency response of the system. The largest variations in both impedance modulus and phase were registered at 0.1 Hz (Table A1). In fact, Au ELD caused a decrease in both $|Z|$ ($\sim 369 \rightarrow \sim 149 \Omega$) and $\text{Phase}(Z)$ ($\sim -71 \rightarrow -51^\circ$). The lower impedance after ELD can be attributed to the formation of a Schottky junction at the Au/NiO interface. Then, Ma thiolated probe ssDNA immobilization increased both $|Z|$ ($\sim 149 \rightarrow \sim 194 \Omega$) and $\text{Phase}(Z)$ ($\sim -36 \rightarrow -51^\circ$).

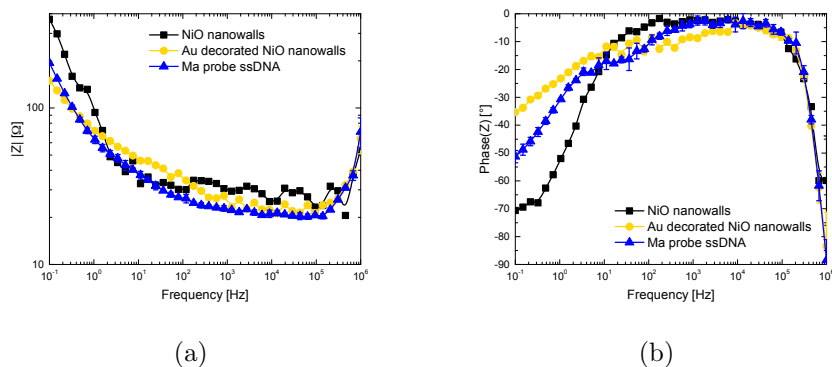


Figure 3.6: Bode plots ((a) impedance modulus versus frequency and (b) impedance phase versus frequency) of NiO nanowalls (black squares), Au decorated NiO nanowalls (yellow circles) and Au decorated NiO nanowalls with Ma probe ssDNA (blue triangles) as obtained by EIS experiments at 0 V versus open circuit potential with 10 mV superimposed sinusoidal voltage in the frequency range $10^6 \div 10^{-1}$ Hz in PBS (pH 7) containing 10 mM $[\text{Fe}(\text{CN})_6]^{3-/4-}$.

Prior to sensing experiments with Ma complementary ssDNA, prehybridization with a high concentration of non-complementary ssDNA was performed. In this way, the surface of the Au decorated NiO nanowalls was completely covered with DNA to obtain a stable

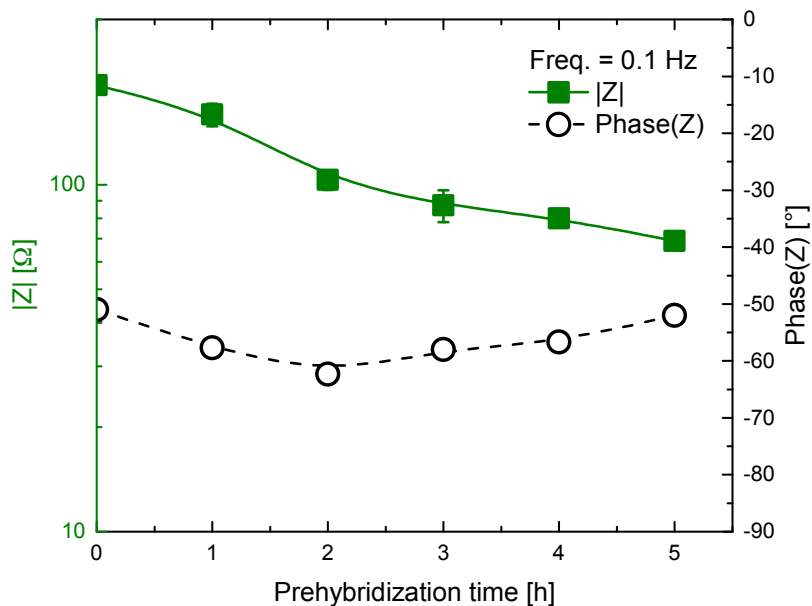


Figure 3.7: Impedance modulus (green closed squares) and phase (black open circles) at 0.1 Hz as function of prehybridization time with non-complementary ssDNA.

impedimetric behaviour. Therefore, it can be reasonably assumed that any further impedance variation after exposure to Ma complementary ssDNA can be ascribed only to its successful hybridization with the immobilized Ma thiolated probe ssDNA. Sensor impedance was monitored as function of prehybridization time (1, 2, 3, 4 and 5 h) and the recorded Bode plots are shown in Figure A5, while the values of impedance modulus and phase at 0.1 Hz are reported in Figure 3.7. $|Z|$ decreased with prehybridization time, and a nearly stable value (~ 69) was obtained only after 5 h. On the contrary,

Phase(Z) was almost constant with prehybridization time and after 5 h it was -52° .

EIS was conducted also after hybridization with different concentrations of Ma complementary ssDNA (1.7, 6, 14.5, 27.2 and 48.5 ng μl^{-1}). The recorded Bode plots are shown in Figure A6, while the values of impedance modulus and phase at 0.1 Hz are reported in Table A1. $|Z|$ increased with increasing Ma complementary ssDNA concentration up to 104 Ω for 48.5 ng μl^{-1} , while Phase(Z) was almost constant and equal to -51° for 48.5 ng μl^{-1} .

These results can be summarized in the Phasor diagram shown in Figure 3.8, where the impedance at 0.1 Hz is represented by a vector with modulus $|Z|$ [Ω] and phase given by the angle with Re Z axis. It is worth noting that Re Z did not change after Au ELD and Ma thiolated probe ssDNA immobilization, while Im Z changed leading to the above aforementioned impedance variations during sensor fabrication process. Prehybridization and hybridization processes did not affect Phase(Z) but only $|Z|$, which, in particular, decreased upon prehybridization with non-complementary ssDNA and increased upon hybridization with Ma complementary ssDNA.

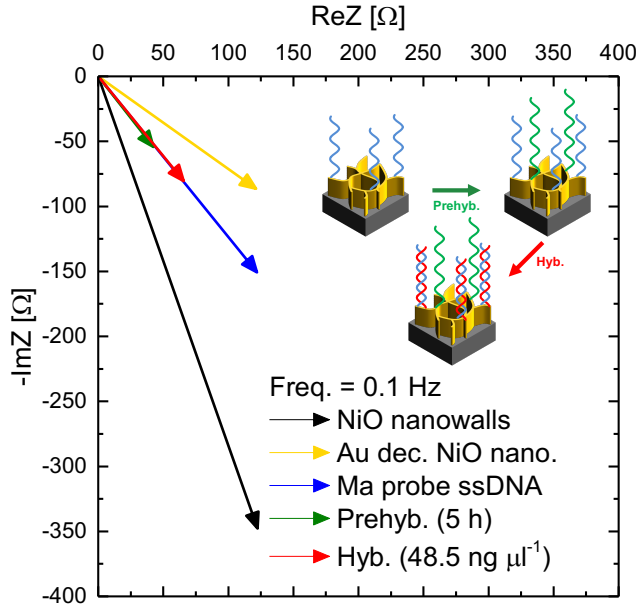


Figure 3.8: Phasor diagram of sensor impedance at 0.1 Hz at the end of each fabrication and sensing steps. The inset is the schematic illustration of the various steps of Ma DNA sensing [3.?.].

Sensor response to Ma complementary ssDNA was evaluated as

$$Response = \frac{|Z_{hyb.}| - |Z_{prehyb.}|}{|Z_{prehyb.}|} * 100 \quad (3.1)$$

where $|Z_{hyb.}|$ [Ω] and $|Z_{prehyb.}|$ [Ω] are the modulus of the impedance after hybridization and 5 h prehybridization, respectively. Figure 3.9 reports the calibration curve of the sensor, showing a high response in the Ma complementary ssDNA concentration range $1.7 \div 6 \text{ ng } \mu\text{l}^{-1}$, and then a saturation in the range $14.5 \div 48.5 \text{ ng } \mu\text{l}^{-1}$. Therefore, the

sensor is able to detect Ma DNA at very low concentrations.

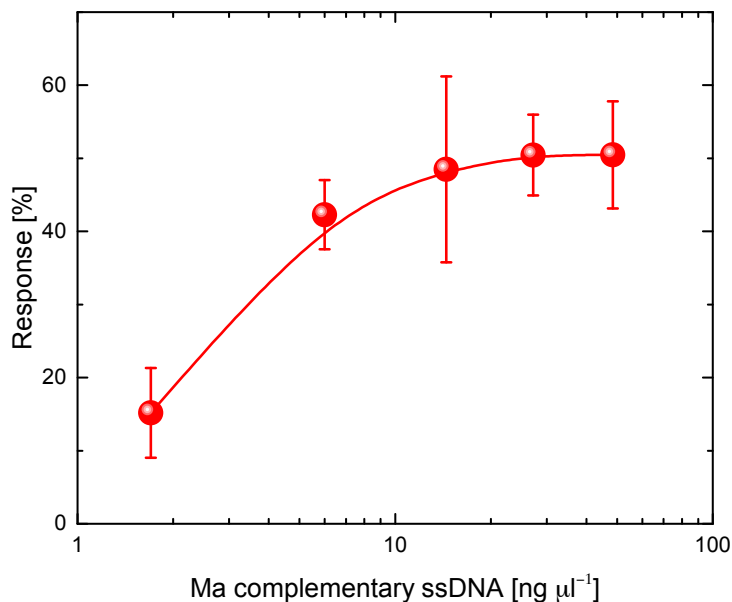


Figure 3.9: Calibration curve of the Ma DNA sensor based on Au decorated NiO nanowalls.

3.4 Conclusions

Novel Au decorated NiO nanowalls were obtained by Au ELD onto NiO nanowalls grown by CBD and thermal annealing. The Au decorated NiO nanowalls represent a low-cost and high surface area platform for thiolated DNA immobilization. In particular, Ma thiolated probe ssDNA was successfully immobilized onto Au decorated NiO

nanowalls and used as an imdedimetric sensor for Ma complementary ssDNA sensing. The sensor demonstrated the ability to detect Ma DNA even at the very low concentration of $1.7 \text{ ng } \mu\text{l}^{-1}$, having also the advantages of cheaper and quicker analysis than conventional PCR-based approach, and also the high selectivity ensured by the intrinsic specificity of DNA hybridization. Moreover, the sensor could be reused, as it is possible to denature the hybridized dsDNA by heating the sensor. These results open the route towards PCR-free Ma detection for the early diagnosis of CA, and allow similar application into other DNA detection.

References

- [3.1] M. Lambert, Contagious agalactia of sheep and goats, *Revue Scientifique et Technique-Office International des Epizooties* **6**, 699 (1987).
- [3.2] G. R. Loria, R. Puleio, and R. A. J. Nicholas, Contagious Agalactia: Economic Losses and Good Practice, *Journal of Bacteriology and Mycology* **5**, 1076 (2018).
- [3.3] D. Bergonier, X. Berthelot, and F. Poumarat, Contagious agalactia of small ruminants: current knowledge concerning epidemiology, diagnosis and control, *Revue Scientifique et Technique-Office International des Epizooties* **16**, 848 (1997).
- [3.4] M. Tolone, A. M. Sutura, S. Borrello, S. Tumino, M. L. Scatassa, B. Portolano, R. Puleio, R. A. J. Nicholas, and G. R. Loria, Effect of *Mycoplasma agalactiae* mastitis on milk production and composition in Valle dell Belice dairy sheep, *Italian Journal of Animal Science* **18**, 1067 (2019).
- [3.5] K. Oravcová, L. López-Enríquez, D. Rodríguez-Lázaro, and M. Hernández, *Mycoplasma Agalactiae* p40 Gene, a Novel Marker for Diagnosis of Contagious Agalactia in Sheep by

Real-Time PCR: Assessment of Analytical Performance and In-House Validation Using Naturally Contaminated Milk Samples, *Journal of Clinical Microbiology* **47**, 445 (2009).

- [3.6] <https://www.oie.int>.
- [3.7] A. M. Parker, J. K. House, M. S. Hazelton, K. L. Bosward, and P. A. Sheehy, Comparison of culture and a multiplex probe PCR for identifying *Mycoplasma* species in bovine milk, semen and swab samples, *PLOS ONE* **12**, e0173422 (2017).
- [3.8] R. Chopra-Dewasthaly, J. Spersger, M. Zimmermann, C. Citti, W. Jechlinger, and R. Rosengarten, *Vpma* phase variation is important for survival and persistence of *Mycoplasma agalactiae* in the immunocompetent host, *PLOS Pathogens* **13**, e1006656 (2017).
- [3.9] A. Kumar, A. Rahal, S. Chakraborty, A. K. Verma, and K. Dhama, *Mycoplasma agalactiae*, an Etiological Agent of Contagious Agalactia in Small Ruminants: A Review, *Veterinary Medicine International* **2014**, (2014).
- [3.10] V. Kavita, DNA Biosensors—A Review, *Journal of Bioengineering and Biomedical Science* **7**, 222 (2017).
- [3.11] <https://en.wikipedia.org>.
- [3.12] M. Kaushik, S. Khurana, K. Mehra, N. Yadav, S. Mishra, and S. Kukreti, Emerging Trends in Advanced Nanomaterials Based Electrochemical Genosensors, *Current Pharmaceutical Design* **24**, 3697 (2018).
- [3.13] J. Zhang, S. Song, L. Zhang, L. Wang, H. Wu, D. Pan, and C. Fan, Sequence-Specific Detection of Femtomolar DNA via a Chronocoulometric DNA Sensor (CDS): Effects of Nanoparticle-Mediated Amplification and Nanoscale Control

- of DNA Assembly at Electrodes, *Journal of the American Chemical Society* **128**, 8575 (2006).
- [3.14] J. Zhang, S. Song, L. Wang, D. Pan, and C. Fan, A gold nanoparticle-based chronocoulometric DNA sensor for amplified detection of DNA, *Nature Protocols* **2**, 2888 (2007).
- [3.15] J. S. Daniels and N. Pourmand, Label-Free Impedance Biosensors: Opportunities and Challenges, *Electroanalysis* **19**, 1239 (2007).
- [3.16] M. Le, C. Jimenez, E. Chainet, and V. Stambouli, A Label-Free Impedimetric DNA Sensor Based on a Nanoporous SnO₂ Film: Fabrication and Detection Performance, *Sensors* **15**, 10686 (2015).
- [3.17] Z. Guler, P. Erkoç, and A. S. Sarac, Electrochemical impedance spectroscopic study of single-stranded DNA-immobilized electroactive polypyrrole-coated electrospun poly (ϵ -caprolactone) nanofibers, *Materials Express* **5**, 269 (2015).
- [3.18] Z. F. Gao, J. B. Gao, L. Y. Zhou, Y. Zhang, J. C. Si, H. Q. Luo, and N. B. Li, Rapid assembly of ssDNA on gold electrode surfaces at low pH and high salt concentration conditions, *RSC Advances* **3**, 12334 (2013).
- [3.19] X. Zhang, M. R. Servos, and J. Liu, Instantaneous and Quantitative Functionalization of Gold Nanoparticles with Thiolated DNA Using a pH-Assisted and Surfactant-Free Route, *Journal of the American Chemical Society* **134**, 7266 (2012).
- [3.20] J. Deka, R. Mëch, L. Ianeselli, H. Amenitsch, F. Cacho-Nerin, P. Parisse, and L. Casalis, Surface Passivation Improves the Synthesis of Highly Stable and Specific DNA-Functionalized Gold Nanoparticles with Variable DNA Density, *ACS Applied Materials & Interfaces* **7**, 7033 (2015).

- [3.21] Y. Shacham-Diamand, T. Osaka, Y. Okinaka, A. Sugiyama, and V. Dubin, 30 years of electroless plating for semiconductor and polymer micro-systems, *Microelectronic Engineering* **132**, 35 (2015).
- [3.22] M. Urso, G. Pellegrino, V. Strano, E. Bruno, F. Priolo, and S. Mirabella, Enhanced sensitivity in non-enzymatic glucose detection by improved growth kinetics of Ni-based nanostructures, *Nanotechnology* **29**, 165601 (2018).

3. Au DECORATED NiO
NANOWALLS FOR
PCR-FREE MYCOPLASMA
AGALACTIAE SENSING

Chapter 4

NiO nanostructures for gas sensing

Contents

4.1	The need of gas sensors	107
4.2	Materials and methods	109
4.2.1	Synthesis	109
4.2.2	Characterization	110
4.3	Acetone sensor based on NiO nanowalls .	110
4.3.1	Overview of acetone sensors based on NiO	110
4.3.2	Morphological and electrical characteriza- tion	112
4.3.3	Acetone sensing performances	113
4.4	NO₂ sensor based on nanoporous NiO film	118
4.4.1	Overview of NO ₂ sensors based on NiO .	118
4.4.2	Morphological and electrical characteriza- tion	120
4.4.3	NO ₂ sensing performances	121
4.4.4	NO ₂ sensing mechanism	132

4.5 Conclusions	136
References	137

Gas sensors based on NiO nanostructures are attracting a great attention, combining the high stability and low-cost of NiO with the high sensitivity of nanostructured materials. Specifically, NiO nanostructures have shown remarkable performances for acetone sensing and NO₂ sensing at room temperature, which are important targets for non-invasive diagnosis of diabetes and environmental monitoring, respectively. However, NiO-based acetone sensors are typically based on composite structures to improve NiO sensitivity, increasing also the cost and complexity of the fabrication process, while no NiO-based NO₂ sensor at room temperature showed high sensitivity, selectivity and stability, and limit of detection (LoD) in the sub-ppm concentration range, as required by applications. In this chapter, NiO nanostructures were fabricated by a low-cost chemical bath deposition (CBD) of Ni(OH)₂ nanowalls and various post-growth thermal annealing processes at 350° C. In particular, NiO nanowalls were obtained upon annealing in inert atmosphere and applied for acetone sensing. The response to acetone at various temperatures was recorded and successfully modelled by two adsorption sites. Both sites are active below 250° C, while only the quicker one is active above 250° C. At the optimal temperature of 250° C, NiO nanowalls showed high sensitivity, good selectivity and low LoD (~200 ppb). Furthermore, a novel nanoporous NiO film, a porous thin film formed by NiO nanoparticles (30-50 nm), was obtained upon annealing in reducing atmosphere followed by annealing in oxidizing atmosphere, and then applied for NO₂ sensing at room temperature, demonstrating high sensitivity to sub-ppm concentrations (140÷700 ppb), excellent selectivity and stability, and an extremely low LoD of 20 ppb. The NO₂ sensing mechanism by NiO was investigated and satisfactorily modelled by two energetically different and independent adsorption sites. Both of them are active at room temperature above a NO₂ concentra-

tion threshold, while only one site is active at higher temperatures. The reported simple and low-cost fabrication methods, and the superior sensing performances of NiO nanowalls and nanoporous NiO film make them promising materials for the development of cheap and reliable sensors of acetone and NO₂ at room temperature.

4.1 The need of gas sensors

In recent years, air pollution has become an issue of major concern all over the world due to the increasing emissions of toxic and harmful gases into the atmosphere [4.1]. Common pollutants include volatile organic compounds (VOCs), CO, SO₂, H₂S, NH₃, O₃ and NO₂ emitted mostly from vehicles and factories (Figure 4.1), which are harmful for the environment and human health and, therefore, need to be continuously monitored by gas sensors [4.2, 3].

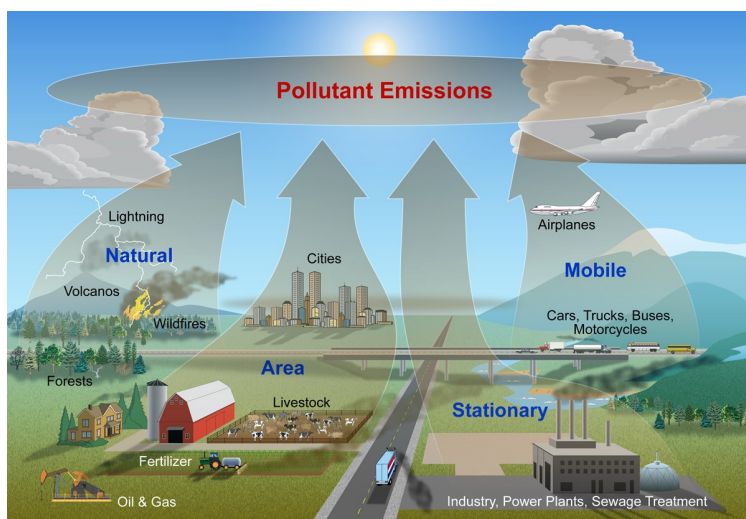


Figure 4.1: Schematic illustration of the air pollutants sources [4.4].

Moreover, several VOCs present in human breath have been directly related to diseases. In fact, it has been demonstrated that

some diseases, such as lung cancer, asthma, diabetes and cystic fibrosis, induce variations of the concentration of specific gases in human breath. The standard analysis of the exhaled breath is done by gas chromatography and mass spectrometry. However, this approach is expensive, complex and time-consuming, especially for early-stage clinical diagnosis. Gas sensors represent a promising alternative to detect VOCs in human breath, however meeting the requirement of fast, accurate and low-cost sensors for early diagnosis of diseases is still challenging [4.1].

Among the different gas sensors, chemoresistive gas sensors based on metal oxide semiconductors sensitive to the surrounding environment are considered the most attracting ones due to their simple operation, fabrication and miniaturization (Figure 4.2) [4.5]. Since the pioneering sensor of Taguchi in 1950, significant progresses were achieved in this field driven by the recent development of nanotechnology [4.1]. In fact, nanostructured metal oxides with high surface-to-volume ratio, high specific surface area and crystal facets with higher surface reactivity have considerably improved the performances of chemoresistive gas sensors [4.5].

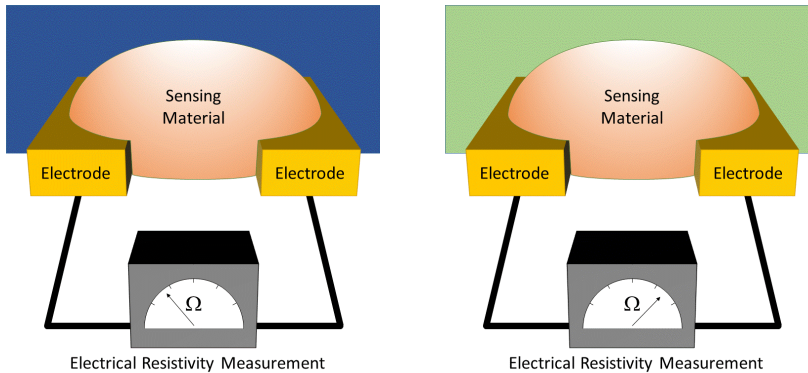


Figure 4.2: Schematic illustration of a chemoresistive gas sensors exposed to two different environments that affect its electrical resistivity [4.6].

NiO, a *p*-type semiconductor, is considered one of the most promising candidate for the development of chemoresistive gas sensors due to its relatively wide bandgap (3.3-4.0 eV), high chemical and thermal stability, measurable resistance variations associated to chemical reactions on the surface, negligible dependence from humidity and low-cost [4.7–10]. As a result, several NiO nanostructures for gas sensors have been reported, showing remarkable sensing performances to various gases, including ethanol, acetone, benzaldehyde, formaldehyde, NO₂, H₂ and H₂S [4.11].

Nowadays, the research on NiO nanostructures for gas sensors is focused on approaching as many as possible of the ideal requirements of a sensor, i.e. high sensitivity, high selectivity, high stability, low LoD and quick response. To achieve them there are two main strategies: 1) developing new NiO nanostructures with unique size and shape-dependent properties, and 2) understanding the microscopic sensing mechanism.

4.2 Materials and methods

4.2.1 Synthesis

Conductometric gas sensors were fabricated onto ceramic platforms, consisting in alumina substrates (6×3 mm²) with Pt interdigitated electrodes on front-side and a Pt heater on backside. The ceramic platforms were cleaned with deionized water (MilliQ, 18 MΩ cm) and dried under N₂ gas flow. Kapton tape was used to prevent deposition onto the Pt heater. Ni(OH)₂ nanowalls were directly deposited onto Pt interdigitated electrodes by a 50°C CBD [4.12]. Solution for CBD was obtained by mixing 0.42 M NiSO₄·6H₂O (Alfa Aesar, 98%), 0.07 M K₂S₂O₈ (Alfa Aesar, 97%) and 3.5 wt% ammonia (Merck, 30-33 wt% NH₃ in H₂O). The solution was heated up to 50°C and maintained at this temperature through a bain-marie configuration. The ceramic platforms were placed vertically in the solution for 8 min, and then rinsed with deionized water to remove unwanted micro-

precipitates and dried under NO_2 gas flow.

Some $\text{Ni}(\text{OH})_2$ nanowalls samples were annealed for 1 h in Ar at 350°C to obtain NiO nanowalls, while the others were annealed for 1 h in Ar, followed by 1 h in forming gas (Ar:H₂ 95:5 mixture) at 350°C to obtain porous thin films formed by Ni nanoparticles (20-30 nm), as widely shown in previous reports [4.13, 14], which were further annealed for 1 h in synthetic dry air (20% O₂, 80% N₂, RH <3%) at 400°C to obtain nanoporous NiO films.

4.2.2 Characterization

The surface morphology of the NiO nanostructures was characterized by a scanning electron microscope (Gemini field emission SEM Carl Zeiss SUPRA 25). SEM images were analysed by Gatan Microscopy Suite Software.

Gas sensing tests were performed in a stainless-steel test chamber which allowed measurements in controlled atmosphere. Gases coming from certified bottles were used and further diluted in synthetic dry air (RH <3%) at a given concentration by mass flow controllers. The sensors were heated from room temperature up to 400°C under a dry air total stream of 100 sccm by using a dual-channel power supplier instrument Agilent E3632A to bias the built-in heater. The response of the sensors to pulses (~ 180 s long) of the gases was evaluated by recording the resistance (or conductance) of the sensitive film at an applied voltage of 1.0 V through a Keithley 6487 picoammeter.

4.3 Acetone sensor based on NiO nanowalls

4.3.1 Overview of acetone sensors based on NiO

Acetone ($\text{C}_3\text{H}_6\text{O}$) is a VOC and appears as a colorless liquid with a characteristic pungent smell and boiling point of 56.5°C , which is widely used in industries, laboratories and also in pharmaceuticals [4.8].

In natural environments, acetone is flammable and explosive. Moreover, acetone is harmful to human health, causing irritation to eyes, nose and throat [4.15]. Furthermore, acetone has recently attracted increasing attentions as a potential biomarker for non-invasive diagnosis of diabetes, since the breath of diabetic patients shows higher acetone concentrations (>1.8 ppm) than healthy people (<0.9 ppm) (Figure 4.3) [4.10]. Therefore, the development of acetone sensors with high sensitivity and selectivity, and low LoD is necessary to ensure safety in workplace and to enable non-invasive diagnosis of diabetes.

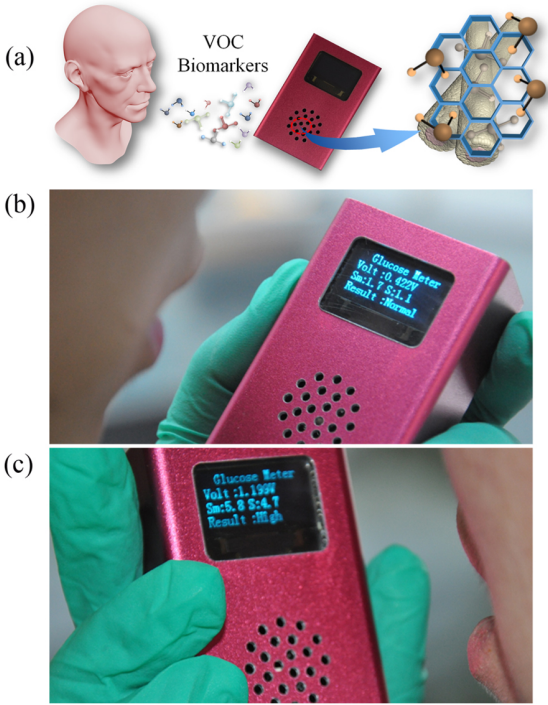


Figure 4.3: (a) Schematic illustration of a portable acetone sensor based on Pt@In₂O₃ core-shell nanowires prepared by electrospinning, and response of the device to the exhaled breath from healthy (b) and diabetic (c) volunteers [4.16].

To improve the sensitivity to acetone, NiO nanostructures have been doped [4.17] or combined with other semiconductor [4.8, 10, 18–21] or metal nanostructures [4.22], demonstrating remarkable response to acetone (0.8–2000 ppm) at relatively high operating temperature (169–400°C). However, the cost and poor scalability of these nanostructures could limit their practical application.

4.3.2 Morphological and electrical characterization

NiO nanowalls were obtained upon thermal annealing in inert atmosphere of Ni(OH)₂ nanowalls grown by CBD. As previously demonstrated by XRD, the annealing process induced a chemical transformation (Ni(OH)₂ → NiO) [4.13]. Moreover, no morphological changes were observed by SEM analysis, in agreement with previous reports. In fact, Figure 4.4(a) shows the plan-view SEM image of NiO nanowalls grown on c-Si substrate, consisting of the well-known porous and high surface area network of ~20 nm thick and ~270 nm tall nanosheets. The thickness was measured from the grey value profile along a line perpendicular to the nanosheets. For example, Figure 4.4(b) reports the measurement along the line perpendicular to the nanosheet marked with the red circle in Figure 4.4(a). The height of the nanosheets was measured by the cross-view SEM image shown in Figure 4.4(c). A high BET surface area of 38 m² g⁻¹ was previously measured for a NiO nanowalls sample prepared under similar conditions [4.13].

NiO nanowalls resistance as function of temperature was measured to determine the activation energy for conduction (Figure A7). By using the Arrhenius equation, an activation energy of 0.35 eV was found (more details in the Appendix). According to the wide bandgap expected for NiO (3.3–4.0 eV) [4.7, 9], this result suggests the presence of defect levels very close to the valence band of NiO, as previously observed for a microwave-synthesized NiO thin film [4.24].

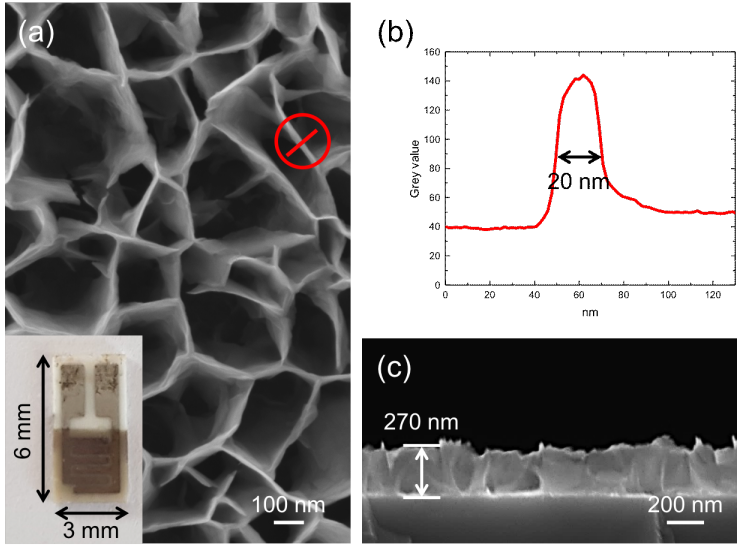


Figure 4.4: (a) Plan-view SEM image of NiO nanowalls (the inset shows the sensor), (b) grey value profile along the line perpendicular to the nanosheet marked with the red circle, and (c) cross-view SEM image of NiO nanowalls [4.23].

4.3.3 Acetone sensing performances

NiO nanowalls grown on interdigitated electrodes (inset in Figure 4.4(a)) were applied for acetone sensing. NiO is a *p*-type semiconductor where holes are the majority carriers. Upon exposure to a reducing gas such as acetone, electrons are injected into NiO and recombine with holes, increasing NiO resistance. Therefore, the response of the NiO-based sensor to acetone [%] was defined as follows

$$Response = \frac{R_{gas} - R_{air}}{R_{air}} * 100 \quad (4.1)$$

where R_{gas} is the resistance under acetone flow [Ω] and R_{air} is the baseline resistance in synthetic dry air [Ω].

It is well known that the gas sensing performances of metal ox-

ides strongly depend on the operating temperature. To identify the optimal temperature for acetone sensing, the response of the sensor to a 10 ppm acetone pulse was recorded at various temperatures (150÷350°C), and the obtained results are compared in Figure 4.5(a). Both the response and signal shape vary significantly with temperature. In particular, the response reaches a maximum at 250°C (Figure 4.5(b)). The signal shape is related to the response kinetics, which can be studied from the fit of the response transient using Langmuir adsorption theory. A single site isotherm was used to fit the response transients at 300 and 350°C, as follows [4.25]

$$Response(t) = R_1 [1 - exp(-t/\tau_1)] \quad (4.2)$$

where R_1 is a pre-exponential factor and τ_1 is the response time [s]. The response transients at 150, 200 and 250°C were fitted only by using a two-site isotherm, as follows [4.25]

$$Response(t) = R_1 w_1 [1 - exp(-t/\tau_1)] + R_2 w_2 [1 - exp(-t/\tau_2)] \quad (4.3)$$

where R_1 and R_2 are pre-exponential factors, τ_1 and τ_2 are the response times of site 1 and 2 [s], w_1 and w_2 are the weight of site 1 and 2 in the response (being $w_1 + w_2 = 1$). Figure 4.5(c) compares the fits for 250°C (left panel) and 350°C (right panel), showing the specific contribution of each site in the response. Similar impressive fits were obtained also for the other temperatures (Figure A8), and the obtained results are shown in Figure 4.5(d). Both sites are active below 250°C, where site 1 is always faster than site 2. Indeed, both sites show quicker kinetics for increasing temperature. By increasing the temperature above 250°C, w_1 increases so that only site 1 is active. Due to the very small response and recovery times above 250°C, a rectangular signal shape is observed in Figure 4.5(a) for 300 and 350°C. Still, at 250°C both sites are equally involved in the response to acetone ($w_1 \approx w_2 \approx 50\%$), resulting in the maximum response in Figure 4.5. Because of the higher and quick enough response at 250°C, further experiments were performed at this temperature.

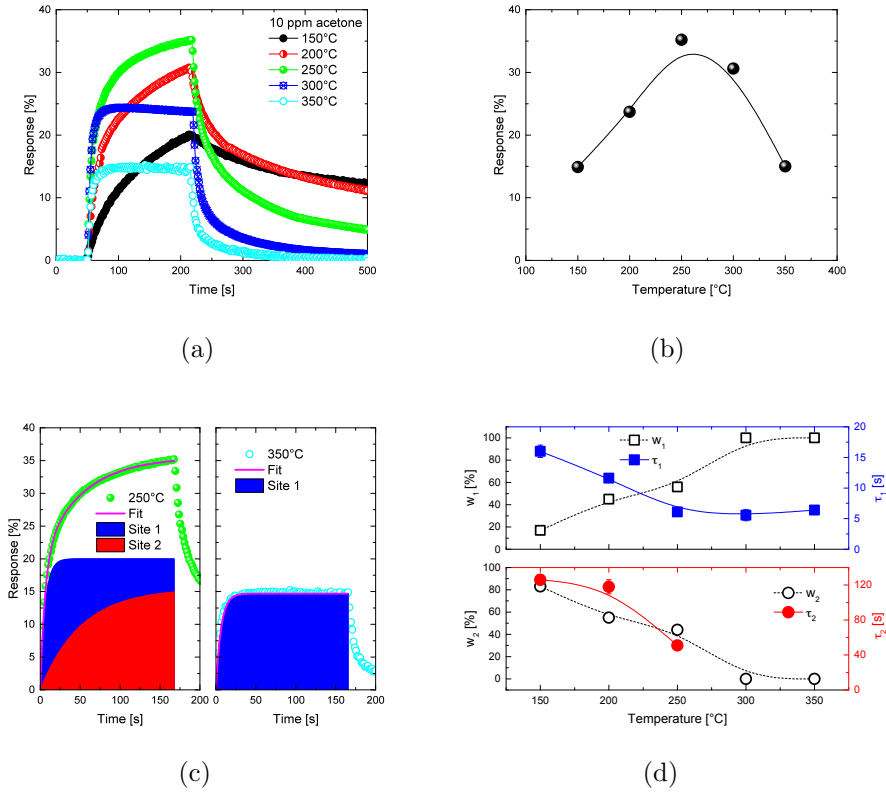
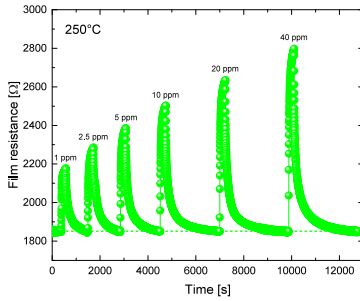


Figure 4.5: (a) Dynamic responses of sensor to a 10 ppm acetone pulse at various temperatures, (b) response as function of temperature, (c) fits of the response transients of 250°C (left panel) and 350°C (right panel) based on a two-site isotherm (equation 4.3) and a single site isotherm (equation 4.2), respectively, and (d) results of the fits of the response transients at various temperatures [4.23].

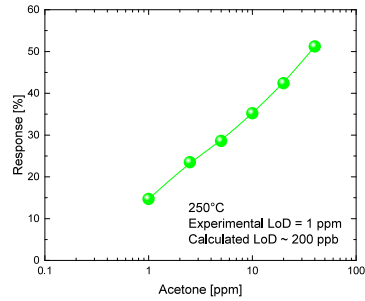
Figure 4.6(a) reports sensor resistance upon exposure to various pulses of acetone in the concentration range 1÷40 ppm at 250°C. Figure 4.6(b) shows the calibration curve at 250°C. By considering $S/N = 3$, a low LoD of ~ 200 ppb was calculated, which is lower than those reported for other NiO-based sensors [4.17, 18]. Figure 4.6(c) reports the results of the fits of the response transients by a two-site isotherm (Figure A9). $w_1 \approx w_2 \approx 50\%$ for all acetone concentrations, while τ_1 and τ_2 show only a small decrease from 2.5 to 5 ppm and then are almost constant, as expected by Langmuir theory for low gas partial pressure. Still, τ_1 is always shorter than τ_2 .

Finally, the selectivity to acetone at 250°C was tested with 10 ppm acetone, ethanol and H_2 , 20 ppm NH_3 , 5 ppm NO_2 and CO pulses (Figure 4.6(d)). The sensor showed comparable responses to acetone and ethanol, as frequently reported for acetone sensors [4.8, 17–20], and much lower responses to the other gases. Such a good selectivity can be further improved by increasing the temperature up to 300°C (Figure A10).

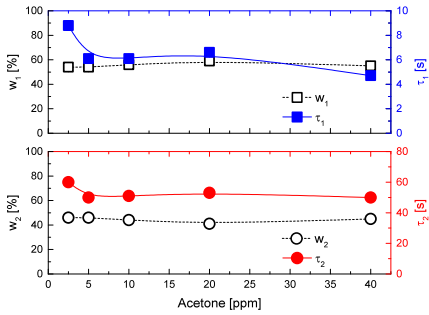
In conclusion, the NiO nanowalls-based sensor demonstrated remarkable acetone sensing performances in terms of high response, good selectivity and low LoD, which make it a promising cheap and efficient acetone sensor for non-invasive diagnosis of diabetes.



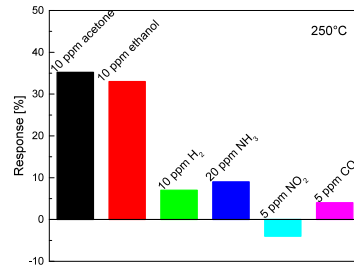
(a)



(b)



(c)



(d)

Figure 4.6: (a) Dynamic responses of the sensor to acetone pulses in the concentration range 1÷40 ppm at 250°C, (b) calibration curve at 250°C, (c) results of the fits of the response transients for various acetone concentrations at 250°C based on a two-site isotherm (equation 4.3), and (d) selectivity test at 250°C [4.23].

4.4 NO₂ sensor based on nanoporous NiO film

4.4.1 Overview of NO₂ sensors based on NiO

Nitrogen dioxide (NO₂) is considered the most dangerous air pollutant since it causes photochemical smog, acid rains, ground-level ozone formation and detrimental effects on plants growth [4.26, 27]. Moreover, NO₂ is irritating to eyes and it can lead to infections in human respiratory system and asthma [4.28]. Due to its harmfulness, in 2010 the United States Environment Protection Agency (USEPA) office fixed the air quality standards for NO₂ to 100 ppb for one hour exposure and 30 ppb for one year exposure (EPA-456/F-11-003) [4.29, 30]. Actually, in 2016 nineteen of the European Union (EU) Member States recorded NO₂ concentrations above the annual limit value of 40 $\mu\text{g m}^{-3}$ (40 ppb) fixed by the EU and World Health Organization (WHO), as shown in Figure 4.7. Therefore, there is a serious need for the decrease of NO₂ emissions as well as the development of NO₂ sensors at sub-ppm concentrations for environmental monitoring.

Despite a wide variety of metal oxides nanostructures with different morphologies has been successfully investigated for NO₂ detection, most materials often require high operating temperatures, leading to higher power consumption, and increased device complexity and cost due to the presence of the heating element [4.32]. In addition, the high operating temperature affects sensor stability and life time due to the thermally induced growth of metal oxide grains, increasing also the risk of ignition upon exposure to flammable or explosive gases [4.5]. To overcome these issues, the development of cost and energy-saving gas sensors at room temperature is required.

Owing to their unique properties, several NiO-based nanostructures have been accurately engineered and tested for NO₂ sensing at room temperature, such as thin films [4.24], nanosheets [4.33, 34], doped structures [4.35], core-shell architectures [4.9], and nanocom-

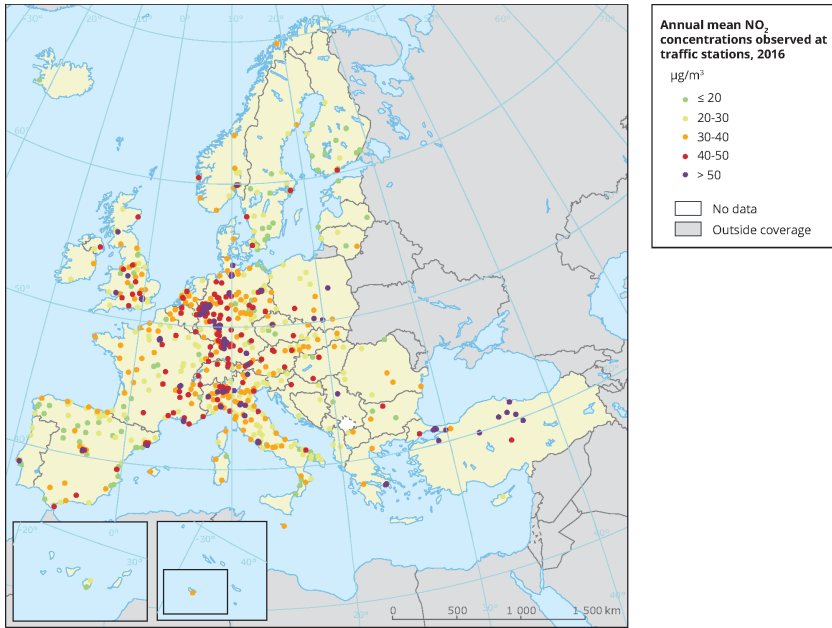


Figure 4.7: Observed concentrations of NO_2 in 2016. Dots in the last two colour categories correspond to values above the annual limit value fixed by EU and WHO ($40 \mu\text{g m}^{-3}$) [4.31].

posites [4.32, 36–43]. However, most of these sensors are based on relevant amounts of nanopowders which lead to high surface area and so high sensitivity [4.44]. Therefore, the fabrication of nanostructured NiO thin films with high surface area and low mass loading of NiO is still challenging. Moreover, the room temperature response and selectivity to sub-ppm NO_2 concentrations have not been properly explored yet, resulting in high LoD values which limit the practical application of these technologies. In addition, despite the chemistry of the interaction between NiO and NO_2 is well-known [4.33], the mechanism behind the NO_2 sensing at room temperature has not been fully clarified.

4.4.2 Morphological and electrical characterization

Figure 4.8(a) reports the schematic illustration of sensor fabrication process by CBD of $\text{Ni}(\text{OH})_2$ nanowalls and post-growth thermal annealing processes ($\text{Ni}(\text{OH})_2 \rightarrow \text{Ni}$ in reducing atmosphere, $\text{Ni} \rightarrow \text{NiO}$ in oxidizing atmosphere). SEM images reported in Figure 4.8 show the characteristic surface morphology of novel nanoporous NiO film, consisting in a self-assembled network of nanosheets formed by bunches of NiO nanoparticles (30-50 nm in size) with high surface-to-volume ratio. These unique morphological features are very promising for easy adsorption and detection of gas molecules.

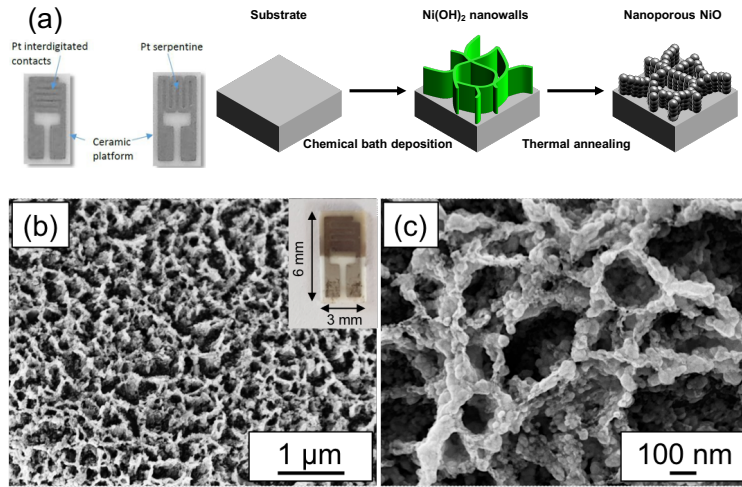


Figure 4.8: (a) Schematic illustration of sensor fabrication process, and (b), (c) SEM images at different magnifications of nanoporous NiO film [4.45].

The $\text{Ni} \rightarrow \text{NiO}$ transformation was confirmed by film resistance measurements during the oxidizing annealing process (Figure 4.9). Prior to the oxidizing annealing, the film showed a room temperature resistance of $\sim 3 \Omega$, which increased with temperature as expected by

a metal. Above $\sim 200^\circ\text{C}$, film resistance decreased with temperature, displaying the typical behaviour of a semiconductor. This change in the electrical behaviour of the film indicates the $\text{Ni} \rightarrow \text{NiO}$ transformation.

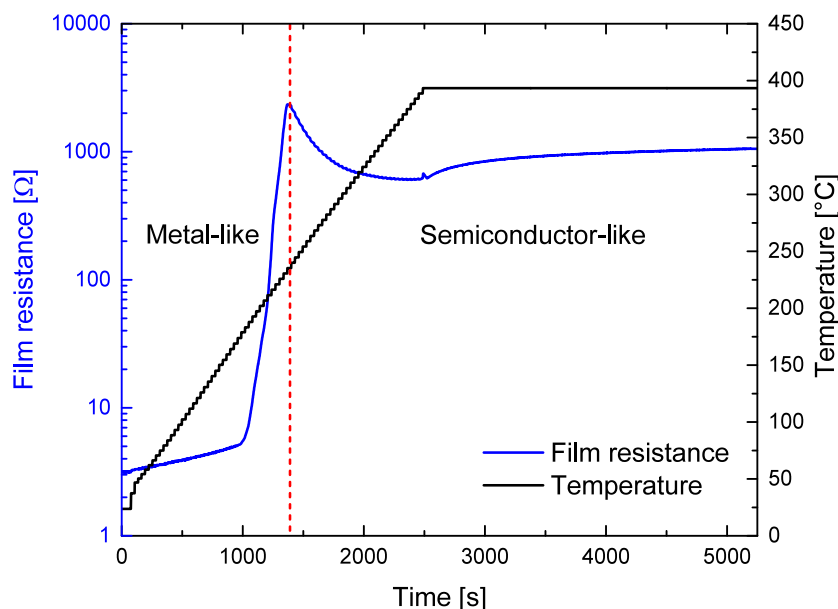


Figure 4.9: Real-time evolution of film resistance during the annealing for 1 h in synthetic dry air at 400°C , performed by using the experimental setup for gas sensing tests [4.45].

4.4.3 NO_2 sensing performances

Both NiO nanowalls and nanoporous NiO film were tested for NO_2 sensing, however only the nanoporous NiO film was considered for

further investigations due to its higher sensitivity (Figure A12).

Figure 4.10 reports the typical dynamic responses of nanoporous NiO film-based sensor when exposed to different pulses of NO_2 (0.14, 0.35, 0.7, 1.4, 2.8, 5.6 ppm) at room temperature ($\sim 20.6^\circ\text{C}$).

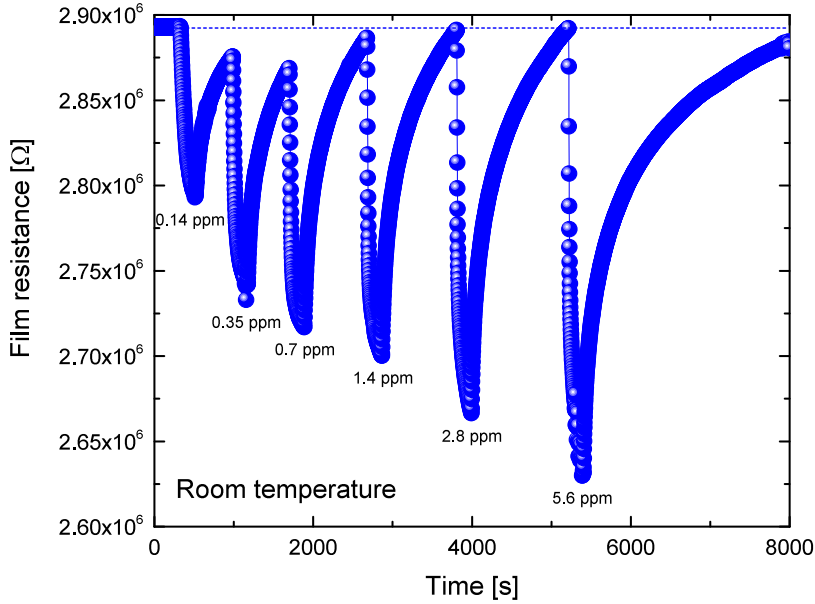


Figure 4.10: Dynamic responses of the sensor when exposed to different pulses of NO_2 (0.14, 0.35, 0.7, 1.4, 2.8, 5.6 ppm) at room temperature [4.45].

The sensor showed a baseline resistance of $\sim 2.89 \text{ M}\Omega$ and a resistance decrease (conductance increase) upon exposure to NO_2 , as expected for a p -type semiconductor interacting with an oxidizing

gas [4.5]. Therefore, sensor response [%] was defined as follows

$$Response = \frac{G_{gas} - G_{air}}{G_{air}} * 100 \quad (4.4)$$

where G_{gas} is the conductance under NO_2 flow [S] and G_{air} is the baseline conductance in synthetic dry air [S].

Previous reports showed that the optimal operating temperature for NiO-based NO_2 sensors is 150°C [4.46, 47]. Therefore, the dynamic responses to NO_2 were also recorded at 150°C (Figure A11). Figure 4.11 compares the calibration curves of the sensor at room temperature and 150°C . Both curves show a non-linear response versus NO_2 concentration, resulting from the complex interaction between NO_2 molecules and NiO surface. In both cases, a response increase with NO_2 concentration is recorded, as expected. Indeed, the response to NO_2 at room temperature is surprisingly higher than 150°C in the sub-ppm concentration range ($0.14 \div 0.7$ ppm), while the response to NO_2 over 3 ppm is almost the same at the two temperatures. Moreover, the LoD, evaluated by considering $S/N = 3$, is 100 ppb at 150°C and as low as 20 ppb at room temperature.

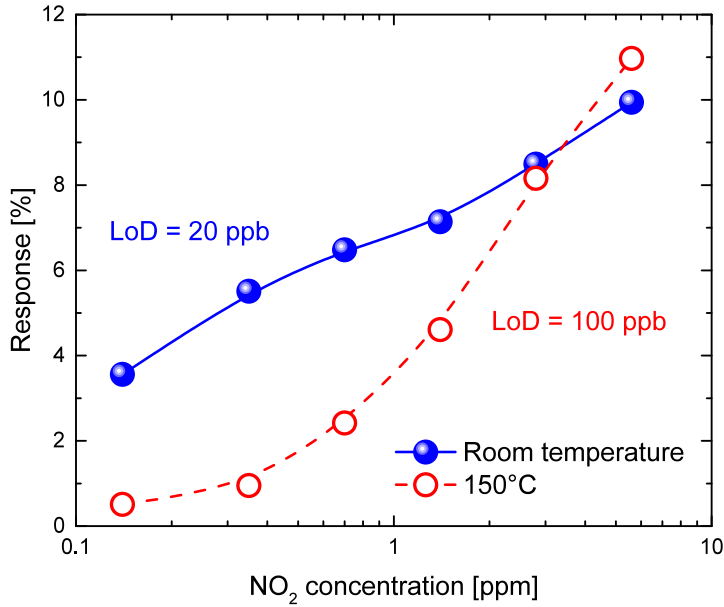


Figure 4.11: NO₂ calibration curves at room temperature (blue spheres) and 150°C (red open circles) [4.45].

To evaluate the response and recovery times of the sensor, the response ($Response(t)_{on}$) and recovery ($Response(t)_{off}$) transients for various NO₂ concentrations (0.14-5.6 ppm) were fitted by using Langmuir adsorption model with a single site, according to the following equations [4.25]

$$Response(t)_{on} = G[1 - \exp(-t/\tau_{on})] \quad (4.5)$$

$$Response(t)_{off} = G \exp(-t/\tau_{off}) \quad (4.6)$$

where G is a pre-exponential factor [%], τ_{on} and τ_{off} are the re-

sponse and recovery times [s]. Figure 4.12(a) shows the fit of the response and recovery transients of 0.7 ppm NO₂ pulse at 150°C. Similar fits were obtained for all NO₂ concentrations (Figure A13) and the results of the fits are reported in Table 4.1. At 150°C τ_{on} decreases and τ_{off} increases with increasing NO₂ concentration. In addition, τ_{on} is typically shorter than τ_{off} for all NO₂ concentrations, in agreement with Langmuir adsorption model.

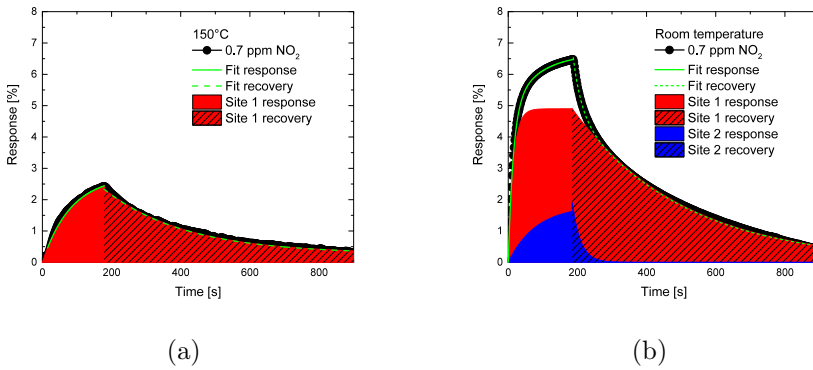


Figure 4.12: Fits of the response and recovery transients to a 0.7 ppm NO₂ pulse based on: (a) a single site isotherm (equations 4.5 and 4.6) at 150°C, and (b) a two-site isotherm (equation 4.7 and 4.8) at room temperature [4.45].

As far as the room temperature behavior is concerned, the results are less straightforward. The 0.14 and 0.35 ppm NO₂ pulses at room temperature can be successfully fitted by a single Langmuir site, while the 0.7-5.6 ppm NO₂ pulses at room temperature required a two-site isotherm as follows [4.25]

$$Response(t)_{on} = G w_{on}[1 - \exp(-t/\tau_{on})] + (100 - w_{on})[1 - \exp(-t/\tau_{on}^*)] \quad (4.7)$$

NO ₂ [ppm]	Response at 150°C	Recovery at 150°C
	τ_{on} [s]	τ_{off} [s]
0.14	294	82
0.35	57	94
0.7	82	234
1.4	57	327
2.8	50	413
5.6	46	494

Table 4.1: Results of the fits of the response and recovery transients for various NO₂ pulses (0.14-5.6 ppm) at 150°C based on a single site isotherm (equations 4.5 and 4.6) [4.45].

$$Response(t)_{off} = G [w_{off} \exp(-t/\tau_{off}^*) + (100 - w_{off}) \exp(-t/\tau_{off}^*)] \quad (4.8)$$

where G is a pre-exponential factor, τ_{on} and τ_{off} are the response and recovery times of site 1 [s], τ_{on}^* and τ_{off}^* are the response and recovery times of site 2 [s], w_{on} and w_{off} represent the weights of the response and recovery, respectively, attributed to site 1 [%].

Figure 4.12(b) reports the fit of the response and recovery transients of 0.7 ppm NO₂ pulse at room temperature, showing the specific contribution of each site in both the response and recovery. Similar impressive fits were obtained for all NO₂ concentrations (Figure A14). The response and recovery times of the two sites and the corresponding weights for all NO₂ concentrations are reported in Table 4.2. Site 1 is always active regardless the NO₂ concentration, τ_{on} is always shorter than τ_{off} , and by increasing NO₂ concentration τ_{on} decreases and τ_{off} increases. Such a behaviour is fully compatible with a typical Langmuir site. On the other hand, site 2 is observed over a NO₂ concentration threshold, τ_{on}^* is always larger than τ_{off}^* , and

NO ₂ [ppm]	Response at room temperature			Recovery at room temperature		
	w_{on} [s]	τ_{off} [s]	τ_{on}^* [s]	w_{off} [s]	τ_{off} [s]	τ_{off}^* [s]
0.14	100	75	/	100	174	/
0.35	100	29	/	100	192	/
0.7	73	14.6	80	72	320	24
1.4	68	13	155	69	526	42.7
2.8	64	10.3	120	68	652	49
5.6	50	8.1	110	60	1230	107

Table 4.2: Results of the fits of the response and recovery transients for various NO₂ concentrations (0.14-5.6 ppm) at room temperature based on a single site isotherm for 0.14 and 0.35 ppm NO₂ (equations 4.5 and 4.6) and a two-site isotherm for 0.7-5.6 ppm NO₂ (equations 4.7 and 4.8) [4.45].

both times have an almost constant trend with NO₂ concentration. Such a behaviour is not compatible with the Langmuir adsorption model and can be attributed to an auxiliary mechanism. In particular, for 0.7 ppm NO₂ site 2 is already active (27% of the response), contributing up to 50% of the response for 5.6 ppm NO₂. Thus, at room temperature a larger contribution from site 2 is observed with increasing NO₂ concentration. Moreover, Table 4.2 shows that at fixed NO₂ concentration the weights of each site in the response and recovery transients, as they came from the fits, are almost the same ($w_{on} = w_{off}$). Therefore, it can be concluded that the two sites act with independent processes and no interaction between them (1 ↔ 2) can be observed. Based on their similar behaviour, site 1 at room temperature can be identified with the single site observed at 150°C. For fixed NO₂ concentration, the longer response time and shorter recovery time of site 1 at 150°C are due to the favoured NO₂ desorption at higher temperatures, which slows down the response and promotes the recovery.

Sensors selectivity to low NO_2 concentrations is critical for practical applications, therefore a selectivity test was performed by exposure to pulses of different gases (140 ppb NO_2 , 100 ppm H_2 , 1000 ppm CO_2 , 50 ppm CO , 1000 ppm methane, 10 ppm acetone, 10% O_2) at room temperature, and the obtained results are reported in Figure 4.13. Sensor response to gases was almost negligible if compared to the response to 140 ppb NO_2 , demonstrating an impressive selectivity at room temperature also when sub-ppm NO_2 concentrations are considered. SEM analysis performed after gas sensing tests showed no appreciable changes in the morphology of nanoporous NiO film, indicating a high stability of the sensing film (Figure A15).

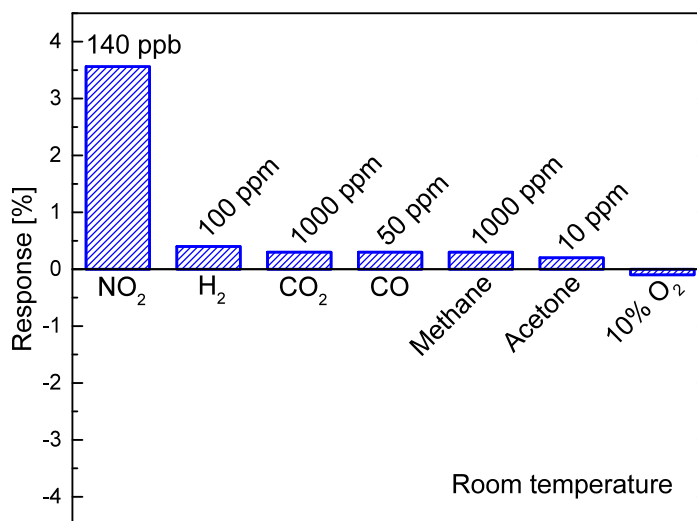


Figure 4.13: Selectivity test at room temperature [4.45].

The long-term stability of sensor response to a 5.6 ppm NO₂ pulse at room temperature was also investigated over a 30-day period (Figure 4.14(a)). Only a 4% loss in the response was observed after 30 days (inset in Figure 4.14(a)), suggesting an exceptional stability of the sensor. Furthermore, the influence of RH variation (<3 → 50%) on both the baseline resistance in air and sensor response to a 5.6 ppm NO₂ pulse at room temperature was examined (Figure 4.14(b)). Such a large humidity variation decreased significantly the baseline resistance from ~2.89 MΩ to ~2.79 MΩ, and also the response to 5.6 ppm NO₂ from ~10 to ~5% (inset in Figure 4.14(b)), while the recovery time increased. Nevertheless, the response loss is relatively small if compared to the large RH variation.

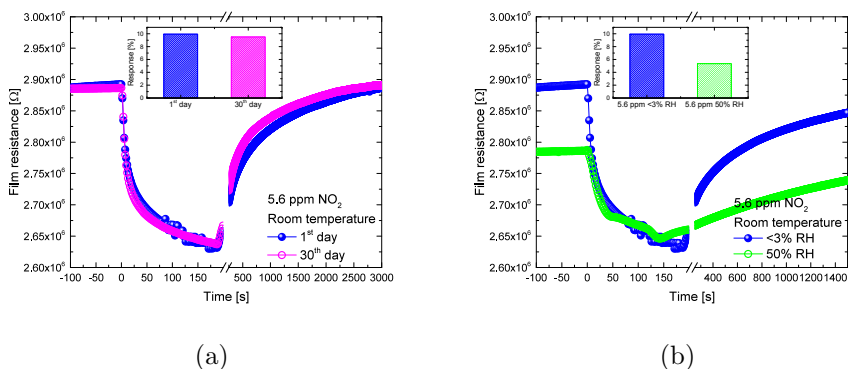


Figure 4.14: (a) Long-term stability of the response to a 5.6 ppm NO₂ pulse at room temperature over a 30-day period, and (b) effect of RH variation (<3 → 50%) on the response to a 5.6 ppm NO₂ pulse at room temperature [4.45].

Table 4.3 reports a comparison of the room temperature NO₂ sensing properties of recent NiO-based sensors. Most of the reported sensors are made of powders which need to be transferred onto electrodes, increasing the complexity of sensor fabrication process [4.9, 32–43]. Only the microwave synthesized NiO thin film by Benedict et al [4.24] and nanoporous NiO film can be grown directly onto electrodes. Furthermore, the nanoporous NiO film showed the lowest experimental (140 ppb) and calculated LoD (20 ppb) and the best selectivity to NO₂ even for concentrations as low as 140 ppb.

Year	Sensing material	Fabrication	Response time, recovery time [s]	Experimental LoD, calculated LoD [ppb]	Selectivity	Ref.
2014	Plate-like p-n heterogenous NiO/WO ₃ nanocomposites	Hydrothermal + annealing	2.5, 1.1 for 30 ppm NO ₂	5000, /	10 ppm NO ₂ vs 10 ppm H ₂ S, CH ₄ , NO, SO ₂ and CO	[4.36]
2015	Camphor sulfonic acid-doped PPy-NiO hybrid nanocomposites	Sol-gel + solid state reaction + doping + transfer onto electrodes	46, 318 for 100 ppm NO ₂	10000, /	100 ppm NO ₂ vs 100 ppm H ₂ S, ethanol, Cl ₂ and NH ₃	[4.38]
2017	In ₂ O ₃ -decorated porous NiO	Nanocasting + calcination + incipient-wetness impregnation + transfer onto electrodes	/	5000, /	15 ppm NO ₂ vs 100 ppm CO, NH ₃ , ethanol, formaldehyde, methanol, toluene, acetone	[4.43]
2017	Al-doped NiO nanosheets	Microwave solvent-thermal reaction + transfer onto electrodes	50, 200 for 10 ppm NO ₂	250, /	/	[4.35]
2017	NiO@CuO nanocomposites	Reflux and hydrothermal + calcination + transfer onto electrodes	2, <150 for 100 ppm NO ₂	1000, /	100 ppm NO ₂ vs CO, CH ₄ , H ₂ (RH 42%)	[4.32]
2017	Mesoporous Ni ₃ N/NiO composite with core-shell structure	Solvothermal + calcination + annealing + transfer onto electrodes	900, 1200 for 1 ppm NO ₂	1000, /	1 ppm NO ₂ vs 1000 ppm toluene, acetone, acetone-trile, H ₂ , ethanol, NH ₃	[4.9]
2018	NiO thin film	Microwave synthesis + annealing	30, / for 0.2 ppm NO ₂	200, /	3 ppm NO ₂ vs 1000 ppm H ₂ , methane, 5 ppm H ₂ S, CO	[4.24]
2018	CuInS ₂ QDs decorated ring-like NiO	Precipitation + hydrothermal + annealing + transfer onto electrodes	/	10000, /	30 ppm NO ₂ vs 1000 ppm CO, 500 NH ₃ , 100 ppm ethanol, formaldehyde and 200 ppm toluene	[4.42]
2019	Nanoporous NiO film	Chemical bath deposition + annealing	75, 174 for 0.14 ppm NO ₂	140, 20	0.14 ppm NO ₂ vs 100 ppm H ₂ , 50 ppm CO, 1000 ppm CO ₂ , methane, acetone, 10% O ₂	[4.45]

Table 4.3: Room temperature NO₂ sensing performances of recent NiO-based sensors [4.45].

4.4.4 NO₂ sensing mechanism

The nanoporous NiO film-based sensor was tested for NO₂ sensing at room temperature and 150°C showing:

- a higher response at room temperature in comparison to 150°C, in the sub-ppm concentration range;
- a single adsorption site at 150°C and two independent adsorption sites at room temperature above a NO₂ concentration threshold.

To explain the higher response at room temperature, the electrical behaviour without NO₂ exposure must be considered. NiO is a *p*-type semiconductor where holes are the majority carriers. Upon exposure to air, O₂ molecules are adsorbed on NiO surface where they capture electrons, leading to upwards band bending and the formation of a hole-accumulation layer beneath the surface. NO₂ has a higher electron affinity (≈ 2.28 eV) than O₂ (0.43 eV), which results in a superior ability to generate holes [4.2]. Therefore, after being exposed to NO₂ a significant hole-accumulation layer is produced, resulting in a higher conductance (lower resistance). By assuming that for a fixed NO₂ concentration the number of holes generated at room temperature and 150°C is almost the same, then the variation of the conductance $\Delta G = G_{gas} - G_{air}$ [S] in equation 4.4 should be the same at the two temperatures. Thus, the following ratio between the response at room temperature and 150°C should be valid

$$\frac{Response(Room\ temperature)}{Response(150^\circ C)} \approx \frac{G_{air}(150^\circ C)}{G_{air}(Room\ temperature)} \quad (4.9)$$

where $G_{air}(Room\ temperature)$ and $G_{air}(150^\circ C)$ are the conductances in air at room temperature and at 150°C, respectively. The ratio in equation 4.9 can be estimated by measuring sensor resistance as function of temperature (Figure A7), leading to $\frac{G_{air}(150^\circ C)}{G_{air}(Room\ temperature)} =$

89. Therefore, equation 4.9 states that the response at room temperature to a fixed NO_2 concentration can be ≈ 89 times higher than 150°C . Actually, Figure 4.11 clearly shows that sensor response to low concentrations of NO_2 at room temperature can be up to 7 times higher than 150°C , that is significantly lower than what expected. In fact, the effect of NO_2 condensation coefficient and hole mobility have not been considered. In particular, it is expected that at higher temperatures the condensation coefficient of NO_2 molecules is lower, leading on average to a lower number of generated holes in NiO. Also, the hole mobility should decrease with increasing temperature. These considerations can explain the divergence of the experimental response enhancement from the expected one.

Concerning the NO_2 sensing mechanism, Zhang et al. have already reported a room temperature NO_2 sensor based on NiO-SnO₂-rGO nanocomposites with two response times in the NO_2 concentration range 5÷60 ppm [4.41]. However, the nature of these response times has not been clarified. In this work, the presence of two response and recovery times at room temperature was confirmed and a model for NO_2 sensing by NiO is proposed based on the following hypotheses:

- the interaction between NO_2 molecules and NiO occurs through two energetically different and independent adsorption sites:
 - site 1, called “Langmuir site”, with short response time and long recovery time;
 - site 2, called “auxiliary site”, with longer response time, shorter recovery time, response slower than recovery, observed only over a NO_2 concentration threshold (0.35-0.7 ppm NO_2 at room temperature).
- at superambient temperatures the desorption of NO_2 molecules from NiO surface is easier, increasing the NO_2 concentration threshold for auxiliary sites activation.

It is worth noting that the behaviour of the auxiliary sites is not common for room temperature NO_2 sensors, however it has been already observed for the NO_2 sensor at room temperature based on graphene flowers by Wu et al. [4.48]. Figure 4.15 shows the schematic illustration of the proposed model for NO_2 sensing by NiO at room temperature and 150°C as function of NO_2 concentration.

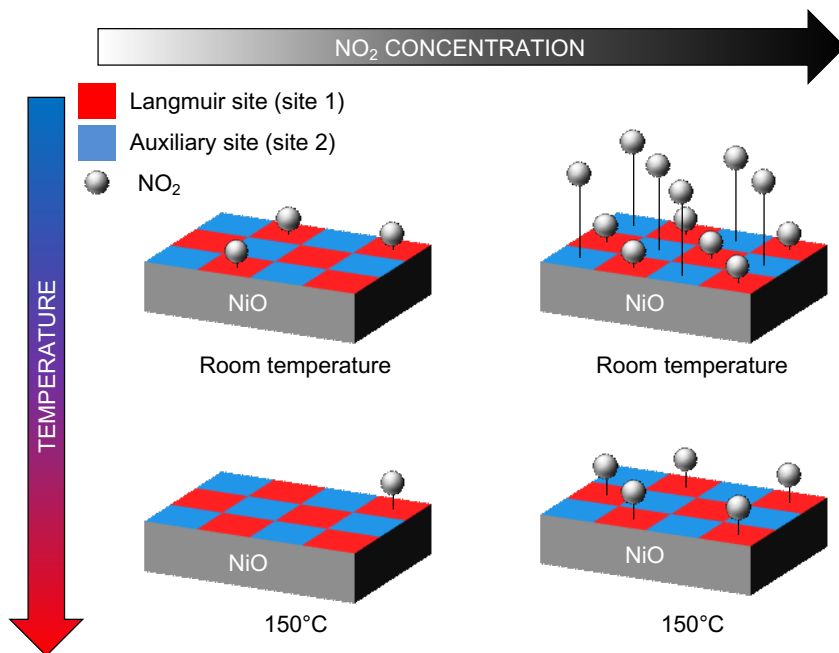


Figure 4.15: Schematic illustration of the proposed model for NO_2 sensing by nanoporous NiO film as function of temperature and NO_2 concentration [4.45].

At room temperature and for low NO_2 concentrations, most of the Langmuir sites are available for NO_2 adsorption, while the auxiliary sites are almost empty due to the easier NO_2 desorption. Therefore, the response to NO_2 is only due to the Langmuir sites. Then, the Langmuir sites coverage increases with NO_2 concentration until a concentration threshold is reached (0.35-0.7 ppm) and only the aux-

iliary sites are available for further NO_2 adsorption. To counterproof this model, the total response at room temperature was decomposed by evaluating the relative weight of each site as function of NO_2 concentration (Figure 4.16). Clearly, above the NO_2 concentration threshold, the response of the Langmuir sites saturates and the response of the auxiliary sites increases.

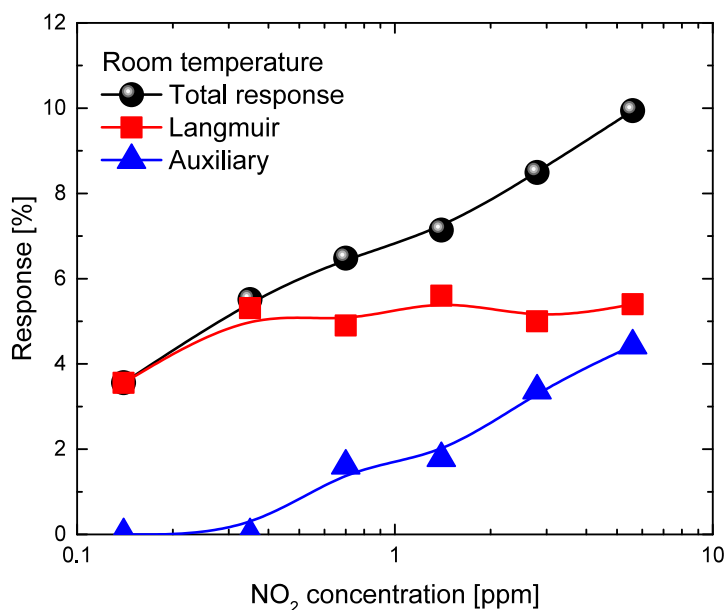


Figure 4.16: Total response to NO_2 at room temperature (black spheres), and response contribution of the Langmuir sites (red squares) and auxiliary sites (blue triangles) [4.45].

At higher temperatures, the desorption of NO_2 molecules from both Langmuir and auxiliary sites is favoured. As a result, the full coverage of the Langmuir sites, and thus the activation of the auxil-

ary sites, is reached at a higher NO_2 concentration threshold than at room temperature. In particular, at 150°C such a threshold is higher than 5.6 ppm NO_2 . As a result, at 150°C only the response of the Langmuir sites is observed in the explored NO_2 concentration range ($0.14\div 5.6 \text{ ppm}$). To further confirm this, the response to a 5.6 ppm NO_2 pulse at higher temperatures (200 and 250°C) was recorded and fitted successfully by using the single site Langmuir model (Figure A16 and A17).

4.5 Conclusions

The low-cost fabrication of gas sensors based on NiO nanostructures (NiO nanowalls and nanoporous NiO film) by chemical bath deposition and post-growth thermal annealing processes was reported.

NiO nanowalls were directly grown onto interdigitated electrodes by CBD method and thermal annealing in inert atmosphere, and applied for acetone sensing. The response transients at various temperatures were recorded and successfully modelled by two adsorption sites. Both sites are active below 250°C , while only the site with shorter response time is active above 250°C . This model explains the variation of the signal shape with the temperature and further deepens the comprehension of acetone-NiO interaction mechanism. At the optimal temperature of 250°C , the NiO nanowalls-based sensor demonstrated remarkable acetone sensing performances in terms of high sensitivity, low LoD ($\sim 200 \text{ ppb}$) and good selectivity, which are particularly promising for non-invasive diagnosis of diabetes.

Novel nanoporous NiO film, a porous thin film formed by NiO nanoparticles ($30\text{-}50 \text{ nm}$ in size) with high surface-to-volume ratio, was applied for NO_2 sensing at room temperature. The sensor showed high sensitivity to NO_2 in the sub-ppm concentration range at room temperature, an extremely low LoD (20 ppb), excellent selectivity to 140 ppb NO_2 and stability. In order to get insight into the NO_2 sensing mechanism, the response and recovery transients were analysed

for various NO₂ concentrations at room temperature and 150°C. Two energetically different and independent adsorption sites were found: the Langmuir site with short response time and long recovery time, and the auxiliary site with longer response time and shorter recovery time. Both sites contribute to the NO₂ sensing at room temperature where the auxiliary sites become relevant only above a NO₂ concentration threshold related to the full coverage of the Langmuir sites. Only the Langmuir sites are active at superambient temperatures due to the favoured NO₂ desorption from both sites. The reported cheap preparation of nanoporous NiO film and its excellent response and selectivity to sub-ppm level NO₂ at room temperature make it a promising NO₂ sensor for environmental monitoring.

References

- [4.1] Y. Deng, *Semiconducting Metal Oxides for Gas Sensing* (Springer, 2019).
- [4.2] N. D. Hoa and S. A. El-Safty, Synthesis of Mesoporous NiO Nanosheets for the Detection of Toxic NO₂ gas, *Chemistry–A European Journal* **17**, 12896 (2011).
- [4.3] S. Thirumalairajan, K. Girija, V. R. Mastelaro, and N. Ponpandian, Surface Morphology-Dependent Room-Temperature LaFeO₃ Nanostructure Thin Films as Selective NO₂ Gas Sensor Prepared by Radio Frequency Magnetron Sputtering, *ACS Applied Materials & Interfaces* **6**, 13917 (2014).
- [4.4] <https://www.nps.gov>.
- [4.5] J. Zhang, X. Liu, G. Neri, and N. Pinna, Nanostructured Materials for Room-Temperature Gas Sensors, *Advanced Materials* **28**, 795 (2016).
- [4.6] <https://en.wikipedia.org>.

- [4.7] S.-Y. Han, D.-H. Lee, Y.-J. Chang, S.-O. Ryu, T.-J. Lee, and C.-H. Chang, The Growth Mechanism of Nickel Oxide Thin Films by Room-Temperature Chemical Bath Deposition, *Journal of the Electrochemical Society* **153**, C382 (2006).
- [4.8] G.-J. Sun, H. Kheel, S. Park, S. Lee, S. E. Park, and C. Lee, Synthesis of TiO₂ nanorods decorated with NiO nanoparticles and their acetone sensing properties, *Ceramics International* **42**, 1063 (2016).
- [4.9] M. Zou, H. Meng, F. Qu, L. Feng, and M. Yang, A mesoporous Ni₃N/NiO composite with a core-shell structure for room temperature, selective and sensitive NO₂ gas sensing, *RSC Advances* **6**, 42917 (2016).
- [4.10] J. Hu, J. Yang, W. Wang, Y. Xue, Y. Sun, P. Li, K. Lian, W. Zhang, L. Chen, J. Shi, and Y. Chen, Synthesis and gas sensing properties of NiO/SnO₂ hierarchical structures toward ppb-level acetone detection, *Materials Research Bulletin* **102**, 294 (2018).
- [4.11] T. P. Mokoena, H. C. Swart, and D. E. Motaung, A review on recent progress of *p*-type nickel oxide based gas sensors: Future perspectives, *Journal of Alloys and Compounds* **805**, 267 (2019).
- [4.12] M. Urso, G. Pellegrino, V. Strano, E. Bruno, F. Priolo, and S. Mirabella, Enhanced sensitivity in non-enzymatic glucose detection by improved growth kinetics of Ni-based nanostructures, *Nanotechnology* **29**, 165601 (2018).
- [4.13] K. O. Iwu, A. Lombardo, R. Sanz, S. Scirè, and S. Mirabella, Facile synthesis of Ni nanofoam for flexible and low-cost non-enzymatic glucose sensing, *Sensors and Actuators B: Chemical* **224**, 764 (2016).

- [4.14] M. Urso, G. Torrasi, S. Boninelli, C. Bongiorno, F. Priolo, and S. Mirabella, Ni(OH)₂@Ni core-shell nanochains as low-cost high-rate performance electrode for energy storage applications, *Scientific Reports* **9**, 7736 (2019).
- [4.15] A. Mirzaei, S. G. Leonardi, and G. Neri, Detection of hazardous volatile organic compounds (VOCs) by metal oxide nanostructures-based gas sensors: A review, *Ceramics international* **42**, 15119 (2016).
- [4.16] W. Liu, L. Xu, K. Sheng, X. Zhou, B. Dong, G. Lu, and H. Song, A highly sensitive and moisture-resistant gas sensor for diabetes diagnosis with Pt@In₂O₃ nanowires and a molecular sieve for protection, *NPG Asia Materials* **10**, 293 (2018).
- [4.17] C. Wang, J. Liu, Q. Yang, P. Sun, Y. Gao, F. Liu, J. Zheng, and G. Lu, Ultrasensitive and low detection limit of acetone gas sensor based on W-doped NiO hierarchical nanostructure, *Sensors and Actuators B: Chemical* **220**, 59 (2015).
- [4.18] C. Liu, L. Zhao, B. Wang, P. Sun, Q. Wang, Y. Gao, X. Liang, T. Zhang, and G. Lu, Acetone gas sensor based on NiO/ZnO hollow spheres: Fast response and recovery, and low (ppb) detection limit, *Journal of Colloid and Interface Science* **495**, 207 (2017).
- [4.19] T. Zhou, X. Liu, R. Zhang, Y. Wang, and T. Zhang, NiO/NiCo₂O₄ Truncated nanocages with PdO Catalyst Functionalization as Sensing Layers for Acetone Detection, *ACS Applied Materials & Interfaces* **10**, 37242 (2018).
- [4.20] M. ul Haq, Z. Wen, Z. Zhang, S. Khan, Z. Lou, Z. Ye, and L. Zhu, A two-step synthesis of nanosheet-covered fibers based on α -Fe₂O₃/NiO composites towards enhanced acetone sensing, *Scientific Reports* **8**, 1705 (2018).

- [4.21] S. Park, G.-J. Sun, H. Kheel, S. Choi, and C. Lee, Acetone Gas Sensing Properties of NiO Particle-Decorated TeO₂ Nanorod Sensors, *Journal of Nanoscience and Nanotechnology* **16**, 8589 (2016).
- [4.22] L. Wang, Z. Lou, T. Fei, and T. Zhang, Enhanced acetone sensing performances of hierarchical hollow Au-loaded NiO hybrid structures, *Sensors and Actuators B: Chemical* **161**, 178 (2012).
- [4.23] M. Urso, S. G. Leonardi, G. Neri, S. Petralia, S. Conoci, F. Priolo, and S. Mirabella, Acetone sensing and modelling by low-cost NiO nanowalls, Under review (2019).
- [4.24] S. Benedict, M. Singh, T. R. R. Naik, S. A. Shivashankar, and N. Bhat, Microwave-Synthesized NiO as a Highly Sensitive and Selective Room-Temperature NO₂ Sensor, *ECS Journal of Solid State Science and Technology* **7**, Q3143 (2018).
- [4.25] K. Mukherjee and S. B. Majumder, Analyses of response and recovery kinetics of zinc ferrite as hydrogen gas sensor, *Journal of Applied Physics* **106**, 064912 (2009).
- [4.26] Z. Li, Y. Liu, D. Guo, J. Guo, and Y. Su, Room-temperature synthesis of CuO/reduced graphene oxide nanohybrids for high-performance NO₂ gas sensor, *Sensors and Actuators B: Chemical* **271**, 306 (2018).
- [4.27] Y. Qin, D. Liu, Z. Wang, and Y. Jiang, Ag nanoparticles-functionalized rough silicon nanowires array and its unique response characteristics to ultrararefied NO₂, *Sensors and Actuators B: Chemical* **258**, 730 (2018).
- [4.28] Y. Liu, X. Gao, F. Li, G. Lu, T. Zhang, and N. Barsan, Pt-In₂O₃ mesoporous nanofibers with enhanced gas sensing performance towards ppb-level NO₂ at room temperature, *Sensors and Actuators B: Chemical* **260**, 927 (2018).

- [4.29] Y. Wu, M. Hu, and Y. Tian, Room temperature NO₂-sensing properties of hexagonal tungsten oxide nanorods, *Chinese Physics B* **26**, 020701 (2017).
- [4.30] J. Hu, Y. Liang, Y. Sun, Z. Zhao, M. Zhang, P. Li, W. Zhang, Y. Chen, and S. Zhuiykov, Highly sensitive NO₂ detection on ppb level by devices based on Pd-loaded In₂O₃ hierarchical microstructures, *Sensors and Actuators B: Chemical* **252**, 116 (2017).
- [4.31] <https://www.eea.europa.eu>.
- [4.32] H. Xu, J. Zhang, A. U. Rehman, L. Gong, K. Kan, L. Li, and K. Shi, Synthesis of NiO@CuO nanocomposite as high-performance gas sensing material for NO₂ at room temperature, *Applied Surface Science* **412**, 230 (2017).
- [4.33] J. Zhang, D. Zeng, Q. Zhu, J. Wu, K. Xu, T. Liao, G. Zhang, and C. Xie, Effect of Grain-Boundaries in NiO Nanosheet Layers Room-Temperature Sensing Mechanism under NO₂, *The Journal of Physical Chemistry C* **119**, 17930 (2015).
- [4.34] J. Zhang, D. Zeng, Q. Zhu, J. Wu, Q. Huang, and C. Xie, Effect of Nickel Vacancies on the Room-Temperature NO₂ Sensing Properties of Mesoporous NiO Nanosheets, *The Journal of Physical Chemistry C* **120**, 3936 (2016).
- [4.35] S. Wang, D. Huang, S. Xu, W. Jiang, T. Wang, J. Hu, N. Hu, Y. Su, Y. Zhang, and Z. Yang, Two-dimensional NiO nanosheets with enhanced room temperature NO₂ sensing performance via Al doping, *Physical Chemistry Chemical Physics* **19**, 19043 (2017).
- [4.36] M. Bao, Y. Chen, F. Li, J. Ma, T. Lv, Y. Tang, L. Chen, Z. Xu, and T. Wang, Plate-like p-n heterogeneous NiO/WO₃ nanocomposites for high performance room temperature NO₂ sensors, *Nanoscale* **6**, 4063 (2014).

- [4.37] S. R. Nalage, A. T. Mane, R. C. Pawar, C. S. Lee, and V. B. Patil, Polypyrrole–NiO hybrid nanocomposite films: highly selective, sensitive, and reproducible NO₂ sensors, *Ionic* **20**, 1607 (2014).
- [4.38] S. R. Nalage, S. T. Navale, R. S. Mane, M. Naushad, F. J. Stadlar, and V. B. Patil, Preparation of camphor-sulfonic acid doped PPy–NiO hybrid nanocomposite for detection of toxic nitrogen dioxide, *Synthetic Metals* **209**, 426 (2015).
- [4.39] J. Zhang, D. Zeng, S. Zhao, J. Wu, K. Xu, Q. Zhu, G. Zhang, and C. Xie, Room temperature NO₂ sensing: what advantage does the rGO–NiO nanocomposite have over pristine NiO?, *Physical Chemistry Chemical Physics* **17**, 14903 (2015).
- [4.40] J. Zhang, D. Zeng, Q. Zhu, J. Wu, Q. Huang, W. Zhang, and C. Xie, Enhanced room temperature NO₂ response of NiO–SnO₂ nanocomposites induced by interface bonds at the p–n heterojunction, *Physical Chemistry Chemical Physics* **18**, 5386 (2016).
- [4.41] J. Zhang, J. Wu, X. Wang, D. Zeng, and C. Xie, Enhancing room-temperature NO₂ sensing properties via forming heterojunction for NiO-rGO composited with SnO₂ nanoplates, *Sensors and Actuators B: Chemical* **243**, 1010 (2017).
- [4.42] J. Zhang, D. Hu, S. Tian, Z. Qin, D. Zeng, and C. Xie, CuInS₂ QDs decorated ring-like NiO for significantly enhanced room-temperature NO₂ sensing performances via effective interfacial charge transfer, *Sensors and Actuators B: Chemical* **256**, 1001 (2018).
- [4.43] Z. Dong and S. Liu, In₂O₃-decorated ordered mesoporous NiO for enhanced NO₂ sensing at room temperature, *Journal of Materials Science: Materials in Electronics* **29**, 2645 (2018).

- [4.44] M. Hjiri, M. Aida, and G. Neri, NO₂ Selective Sensor Based on α -Fe₂O₃ Nanoparticles Synthesized via Hydrothermal Technique, *Sensors* **19**, 167 (2019).
- [4.45] M. Urso, S. G. Leonardi, G. Neri, S. Petralia, S. Conoci, F. Priolo, and S. Mirabella, Room temperature detection and modelling of sub-ppm NO₂ by low-cost nanoporous NiO film, Under review (2019).
- [4.46] I. Hotovy, V. Rehacek, P. Siciliano, S. Capone, and L. Spiess, Sensing characteristics of NiO thin films as NO₂ gas sensor, *Thin Solid Films* **418**, 9 (2002).
- [4.47] G. Li, X. Wang, L. Liu, R. Liu, F. Shen, Z. Cui, W. Chen, and T. Zhang, Controllable Synthesis of 3D Ni(OH)₂ and NiO Nanowalls on Various Substrates for High-Performance Nanosensors, *Small* **11**, 731 (2015).
- [4.48] J. Wu, S. Feng, X. Wei, J. Shen, W. Lu, H. Shi, K. Tao, S. Lu, T. Sun, L. Yu, C. Du, J. Miao, and L. K. Norford, Facile Synthesis of 3D Graphene Flowers for Ultrasensitive and Highly Reversible Gas Sensing, *Advanced Functional Materials* **26**, 7462 (2016).

Chapter 5

Ni(OH)₂@Ni core-shell nanochains for energy storage applications

Contents

5.1	Hybrid supercapacitors	147
5.2	Materials and methods	152
5.2.1	Synthesis	152
5.2.2	Characterization	153
5.3	Ni(OH)₂@Ni core-shell nanochains	153
5.3.1	Morphological, structural and chemical characterization . . .	153
5.3.2	Energy storage performances	160
5.3.3	Energy storage mechanism	169
5.4	Conclusions	175
	References	175

Hybrid supercapacitors, formed by a high power density capacitor-type electrode and a high energy density battery-type electrode, have attracted enormous attention due to their potential application in future electric vehicles, smart electric grids, miniaturized electronic and optoelectronic devices, etc. Ni(OH)₂ is considered a promising battery-type material for hybrid supercapacitors because of its high theoretical capacity and low-cost. Clearly, the energy storage performances of Ni(OH)₂ electrodes rely mainly on their peculiar design. In literature, various Ni(OH)₂ nanostructures have been tested, however they typically suffer from poor rate capability, i.e. low capacity retention at fast charge-discharge rates, limiting their coupling with capacitor-type electrodes. In this chapter, a novel and low-cost approach to fabricate a promising core-shell battery-type electrode for hybrid supercapacitors is presented. Ni(OH)₂@Ni core-shell nanochains were obtained by an electrochemical oxidation of Ni nanoparticles grown by chemical bath deposition (CBD) and thermal annealing in reducing atmosphere. This innovative nanostructure demonstrated a remarkable charge storage ability in terms of high capacity (237 mAh g⁻¹ at 1 A g⁻¹) and rate capability (76% at 16 A g⁻¹, 32% at 64 A g⁻¹). The relationships between electrochemical properties and core-shell architecture were investigated and modelled. The high-conductivity Ni core provides low electrode resistance and excellent electron transport from the Ni(OH)₂ shell to the current collector, resulting in improved capacity and rate capability. The reported preparation method and unique electrochemical behaviour of Ni(OH)₂@Ni core-shell nanochains show great potentialities in many field, including hybrid supercapacitors, batteries, electrochemical (bio)sensing, gas sensing and photocatalysis.

5.1 Hybrid supercapacitors

The growing world energy demand, finite supply of fossil fuels and climate change due to detrimental gases emission have attracted a great attention of researchers in renewable energy resources and related energy storage technologies. A large variety of energy storage devices has been developed so far, including batteries and supercapacitors (Figure 5.1) [5.1].

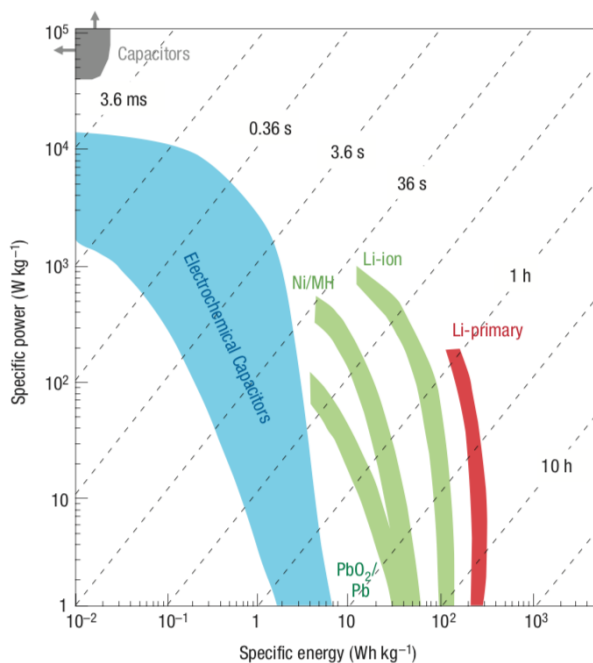


Figure 5.1: Ragone plot (specific power density against specific energy density) of various electrical energy storage devices [5.2].

Batteries store energy through diffusion controlled redox reactions in bulk electrode material, leading to high energy density. However, their low power density hinders their use in those applications where high power is required. On the other hand, supercapacitors, such as

the electrical double layer capacitors (EDLCs) based on charge separation at large electrode/electrolyte interface, bridge the gap between conventional capacitors and batteries, providing higher energy density than conventional capacitors and higher power density than batteries [5.2]. Figure 5.2 shows the schematic illustration of the energy storage mechanisms of batteries and supercapacitors. Batteries are characterized by redox peaks in cyclic voltammograms and plateaus in galvanostatic discharge profiles (Figure 5.2(f) and (h)). Contrarily, EDLCs are characterized by rectangular cyclic voltammograms and linear galvanostatic discharge profiles (Figure 5.2(e) and (g)). The electrochemical behaviour of EDLCs has been observed also for some materials, such as RuO₂ and MnO₂, which store energy through fast and reversible surface redox reactions. This class of materials is typically referred to as “pseudocapacitors”. Despite this clear definition, many battery-type electrodes such as LiCoO₂, Ni(OH)₂, NiO and other materials that exhibit faradaic behaviour have been often presented as pseudocapacitive materials. As a result, the concept of specific capacitance [F g⁻¹] has been applied for these materials where the most significant feature is the specific capacity [mAh g⁻¹], leading to confusing results and no straightforward comparison in literature [5.3–5].

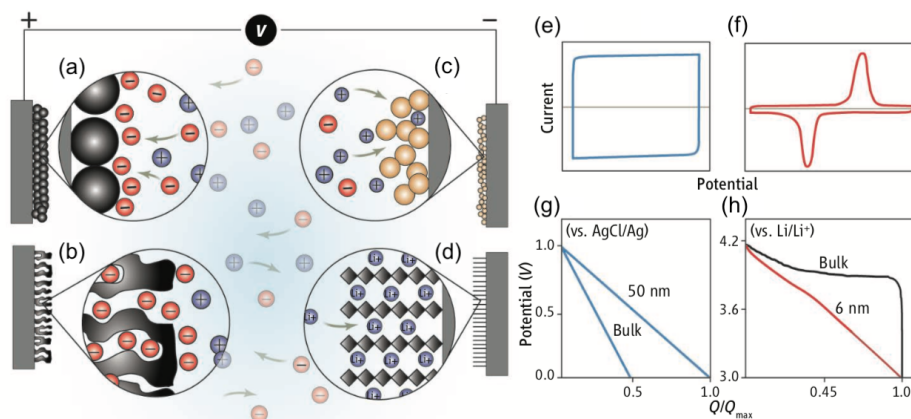


Figure 5.2: (a-d) Schematic illustration of the different energy storage mechanisms of capacitors and batteries. Double-layer capacitance develops at (a) carbon particles or (b) porous carbon electrodes, arising from adsorption of negative ions from the electrolyte onto the positively charged electrodes. Pseudocapacitive mechanisms include (c) redox pseudocapacitance, as it occurs in RuO_2 , and (d) intercalation pseudocapacitance, where Li^+ ions are inserted into the host material. (e-h) Electrochemical characteristics distinguishing capacitor and battery-type materials. Cyclic voltammograms distinguish a capacitor-type material, where the response to a linear change in potential is a constant current (e), from a battery-type material, which exhibits faradaic redox peaks (f). The galvanostatic discharge behaviour (where Q is the charge) of a MnO_2 pseudocapacitor is linear for both bulk and nanoscale material (g), while for LiCoO_2 is linear for nanoscale material and shows a voltage plateau for bulk material (h), leading to a wrong classification of LiCoO_2 as a pseudocapacitive material, as it has occurred for $\text{Ni}(\text{OH})_2$ and NiO nanostructures [5.3].

Recently, novel supercapacitor-battery hybrid systems, namely, hybrid supercapacitors, have received increasing interest since they combine the high power density of a supercapacitor-type material (negative electrode) with the high energy density of a battery-type material (positive electrode) (Figure 5.3) [5.6].

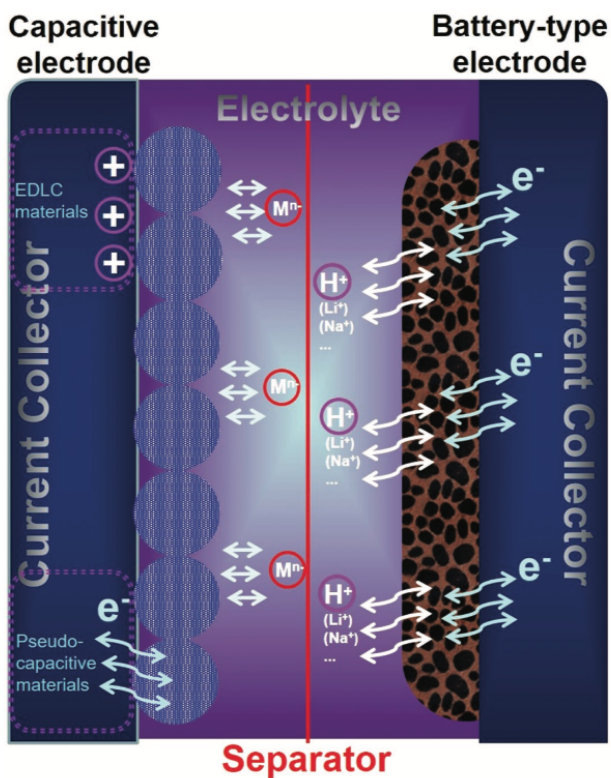


Figure 5.3: General structure and energy storage mechanism of hybrid supercapacitors [5.6].

Among the most investigated positive electrodes for hybrid supercapacitors are NiO and Ni(OH)₂ owing to their low-cost, well-defined redox reactions, environmental friendliness and high theoretical capacity (359 and 289 mAh g⁻¹, respectively) [5.5].

The most efficient strategy to obtain Ni(OH)₂ and NiO electrodes with high capacity is to fabricate nanostructured materials. In fact, it has been demonstrated that Ni(OH)₂ and NiO nanostructures possess superior electrochemical properties due to their high surface-to-volume ratio, efficient electrolyte penetration and low resistance [5.7]. Over the past years, 0D (nanoparticles [5.8]), 1D (nanowires [5.9]), 2D (nanosheets [5.10]) and 3D (flower-like structures [5.11], nanowalls [5.12]) nanostructures have been developed. Among them, 3D nanostructures are the most advantageous ones, since their better connectivity results in higher electrical conductivity and improved mechanical stability [5.13]. In particular, Ni(OH)₂ nanowalls are particularly promising, adding the advantage of a unique open nanoporous structure formed by a tight network of nanosheets (20 nm thick, 0.1÷2 μm tall) with excellent flexibility [5.12]. Also, Ni(OH)₂ nanowalls can be prepared by simple, low-cost, low-temperature and large-area CBD [5.7]. Despite these promising features, only a few nanostructures have a capacity close to the theoretical one [5.5]. Moreover, most of them suffer from poor rate capability, since capacity dramatically decreases at the high charge-discharge rates required for high power applications. This is commonly attributed to the poor electrical conductivities of Ni(OH)₂ and NiO-based materials [5.13].

An effective approach to improve the rate capability of Ni(OH)₂ and NiO nanostructures is to deposit them onto highly conductive current collectors, such as Ni nanotubes arrays [5.14], graphene [5.15], carbon nanotubes [5.16] and carbon coated 3D copper structure [5.17]. Another favourable strategy is based on core-shell nanostructures, which take advantage of the synergistic properties offered by the two components (electrochemically active shell and high-conductivity core). Semiconductive (3D TiO₂ nanowires arrays [5.18]) and metallic (3D Ni nanoparticles [5.19] and Ni nanoparticle tube arrays [5.20]) cores have been reported, showing remarkable energy storage performances for application in hybrid supercapacitors.

Despite the increasing number of reports on Ni(OH)₂ and NiO core-shell nanostructures for hybrid supercapacitors, a simple and

cost-effective approach to fabricate core-shell nanostructured electrodes with high capacity and rate capability is still absent, limiting their transfer to commercial products [5.5, 13]. Furthermore, the effects of core-shell architecture on the energy storage process have not been fully clarified yet. Therefore, a detailed comprehension of the electrochemical behaviour of core-shell nanostructures could lead to an effective improvement of the energy storage performances of these materials.

5.2 Materials and methods

5.2.1 Synthesis

Ni foam substrates ($1 \times 1.5 \text{ cm}^2$, Goodfellow, thickness 1.6 mm, porosity 95%, 20 pores cm^{-1}) were rinsed with acetone, isopropanol and deionized water (MilliQ, 18 $\text{M}\Omega \text{ cm}$), and dried under N_2 gas flow. Ni(OH)_2 nanowalls were grown on cleaned substrates by a 50°C CBD [5.21]. Solution for CBD was prepared by mixing 0.42 M $\text{NiSO}_4 \cdot 6\text{H}_2\text{O}$ (Alfa Aesar, 98%), 0.07 M $\text{K}_2\text{S}_2\text{O}_8$ (Alfa Aesar, 97%) and 3.5 wt% ammonia (Merck, 30-33 wt% NH_3 in H_2O). The solution was heated up to 50°C and kept at this temperature through a bain-marie configuration. The substrates were immersed ($1 \times 1 \text{ cm}^2$ area) in the solution for 20 min, and then rinsed with deionized water to remove unwanted microparticulate and dried in N_2 gas flow. Some samples were further annealed at 350°C for 60 min in Ar followed by 60 min in forming gas (Ar: H_2 95:5 mixture) to obtain Ni nanoparticles, as previously reported [5.21, 22]. Finally, Ni(OH)_2 @Ni core-shell nanochains were obtained by electrochemical oxidation of Ni nanoparticles surface through 100 cycles of cyclic voltammetry (CV) in the potential range $-0.2 \div 0.8 \text{ V}$ at 50 mV s^{-1} scan rate.

Film mass after each synthesis step was measured with a Mettler Toledo MX5 Microbalance (sensitivity: 0.001 mg). Before weighing, samples were washed several times with deionized water, dried in N_2 gas flow and put in an oven at 60°C for 1 h.

5.2.2 Characterization

Samples morphology and structure were characterized by a scanning electron microscope (Gemini field emission SEM Carl Zeiss SUPRA 25) and a transmission electron microscope (JEOL JEM-2010F TEM) operating at 200 keV accelerating voltage. A chemical analysis was conducted by electron energy loss spectroscopy (EELS) in scanning transmission electron microscopy mode (STEM). Samples for TEM observation were prepared by standard TEM specimen preparation techniques by using a flat Ni substrate.

The electrochemical oxidation process and electrochemical measurements were performed at room temperature by using a potentiostat (VersaSTAT 4, Princeton Applied Research, USA) and a three-electrode setup with a Pt counter electrode, a saturated calomel electrode (SCE) as reference electrode, Ni-based nanostructures as working electrodes ($1 \times 1 \text{ cm}^2$ immersed area), in 1 M potassium hydroxide (KOH, Sigma Aldrich, $\geq 85\%$) supporting electrolyte. CV curves were recorded at different scan rates ($1\text{-}50 \text{ mV s}^{-1}$) in the potential range $-0.2 \div 0.8 \text{ V}$. Galvanostatic charge-discharge (GCD) tests were conducted at different current densities ($1\text{-}64 \text{ A g}^{-1}$) in the potential range $0 \div 0.4 \text{ V}$. Electrochemical impedance spectroscopy (EIS) was performed at 0 V versus open circuit potential with a 5 mV superimposed sinusoidal voltage in the frequency range $10^4\text{-}10^{-2} \text{ Hz}$.

5.3 Ni(OH)₂@Ni core-shell nanochains

5.3.1 Morphological, structural and chemical characterization

A conductive core is required to enable faster electron transfer, and thus high-rate energy storage performances. In this work, Ni(OH)₂@Ni core-shell nanochains were obtained by a three-step synthesis (CBD, thermal annealing in reducing atmosphere and electrochemical oxidation) as shown in Figure 5.4.

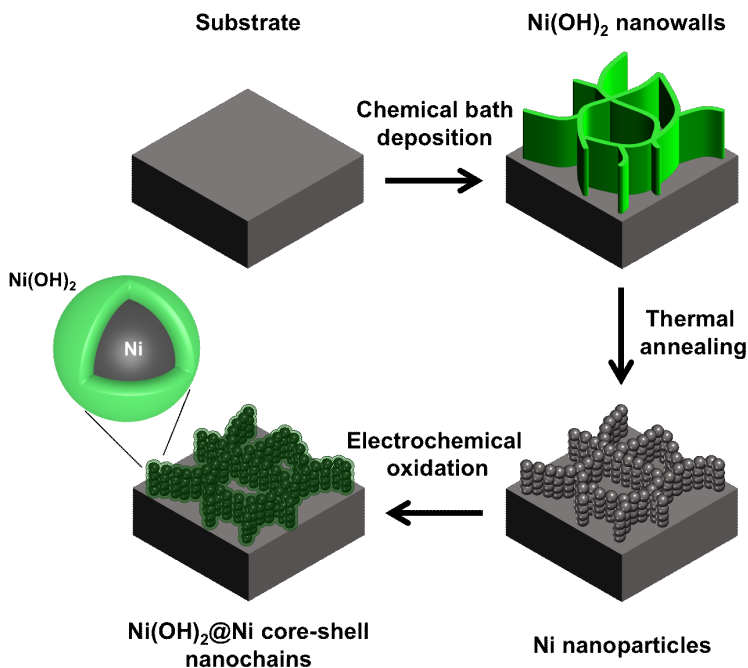


Figure 5.4: Schematic illustration of the three-step synthesis of $\text{Ni(OH)}_2@Ni$ core-shell nanochains [5.23].

Figure 5.5(a) and (b) report SEM images at different magnifications of Ni(OH)_2 nanowalls grown by CBD. Then, the reducing annealing led to a structural and chemical transformation. As shown in Figure 5.5(c) and (d), Ni(OH)_2 nanowalls were transformed into chain-like clusters of metallic Ni nanoparticles (20-30 nm in size). XRD patterns before and after annealing confirmed the $\text{Ni(OH)}_2 \rightarrow Ni$ transformation [5.22].

An electrochemical oxidation process was finally used to obtain the core-shell structure by CV. Figure 5.6 reports the CV curves recorded during the electrochemical oxidation of Ni nanoparticles. Two pronounced oxidation and reduction peaks appeared with in-

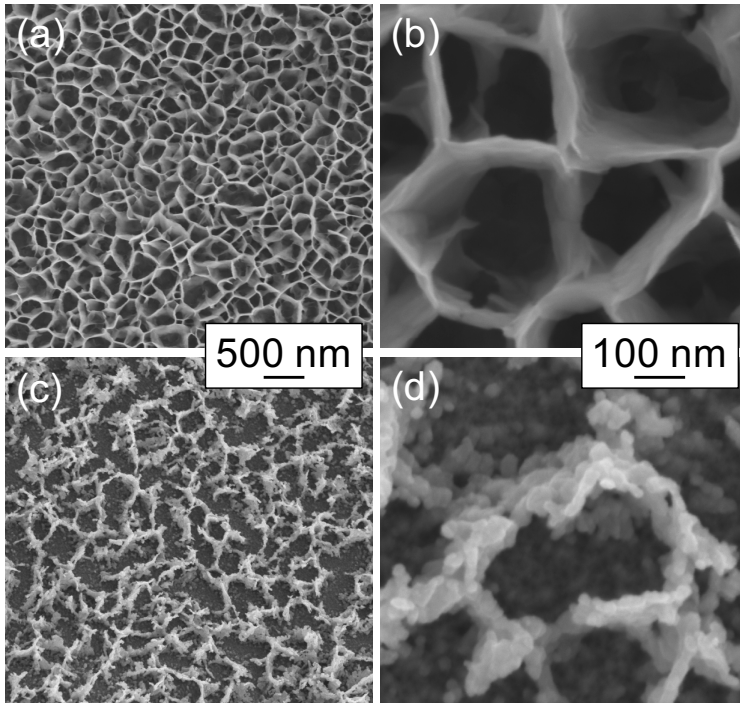
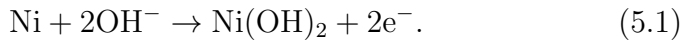


Figure 5.5: SEM images of (a), (b) Ni(OH)₂ nanowalls, and (c), (d) Ni nanoparticles at different magnifications [5.23].

creasing cycle number, which are attributed to the redox couple Ni²⁺/Ni³⁺. In fact, first Ni(OH)₂ is formed because of the reaction between Ni nanoparticles surface and OH⁻ ions in solution [5.24]:



Then, the reversible redox reaction Ni²⁺/Ni³⁺ in alkaline medium occurs (equation 1.1), forming Ni(OH)₂/NiOOH.

Peaks area enlargement with cycling is due to the increasing volume of Ni(OH)₂/NiOOH. The electrochemical oxidation was stopped after 100 CV cycles since almost stable curves were obtained.

TEM analyses were performed to investigate the crystallinity of

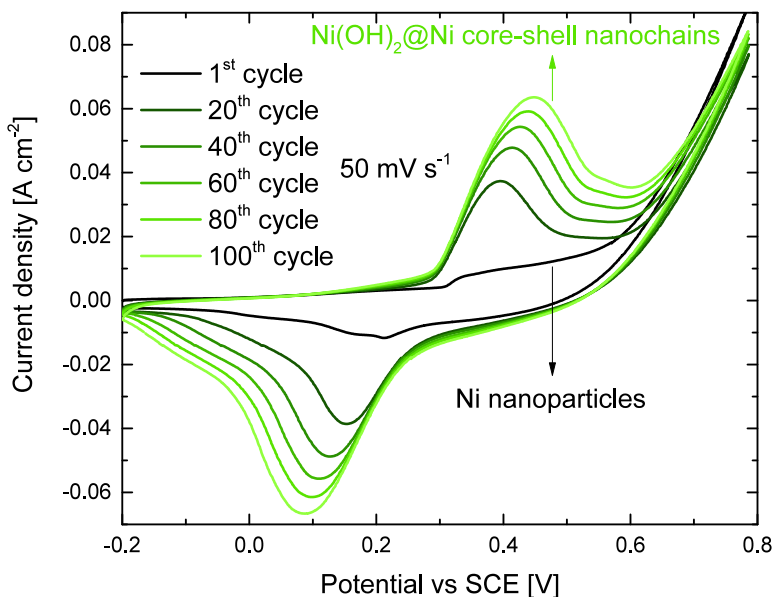


Figure 5.6: Electrochemical oxidation of Ni nanoparticles performed by 100 CV cycles at 50 mV s^{-1} in the potential range $-0.2 \div 0.8 \text{ V}$ in 1 M KOH [5.23].

$\text{Ni(OH)}_2@Ni$ core-shell nanochains. Figure 5.7(a) reports a bright field image of the sample, displaying some bunches of nanoparticles with diameters ranging between 20-30 nm. The high resolution TEM (HR-TEM) image reported in the inset in Figure 5.7(a) clearly demonstrates the core-shell structure, showing a 20 nm large nanoparticle surrounded by a 3-4 nm thin shell. The core presents a set of family planes with fringes separated by a distance equal to 1.8 \AA , while the shell displays two different family planes whose interplanar distances are equal to 2.1 and 2.3 \AA . Such interplanar

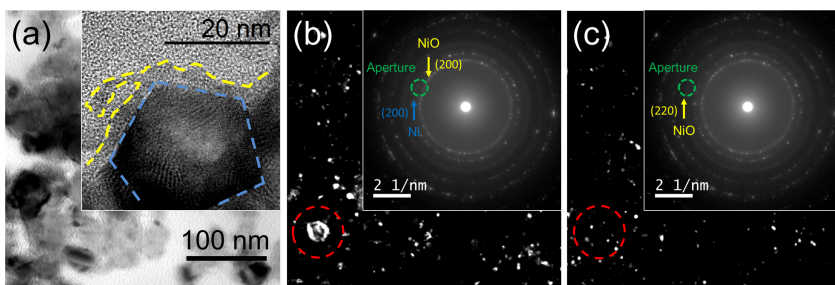


Figure 5.7: TEM images of $\text{Ni}(\text{OH})_2@ \text{Ni}$ core-shell nanochains: (a) bright field image (HR-TEM image in inset), (b), (c) dark field images for different position of objective aperture (green dashed circle) in SAED pattern (inset) [5.23].

distances are compatible with $\{200\}$ Ni (1.8 \AA), $\{200\}$ NiO (2.1 \AA) and $\{101\}$ $\text{Ni}(\text{OH})_2$ (2.3 \AA), respectively [5.14]. Selected Area Electron Diffraction (SAED) ring-like patterns, acquired from the same region, are shown in the insets in Figures 5.7(b) and (c), denoting the polycrystalline nature of the sample, and confirm the presence of $\{200\}$ Ni, $\{200\}$ and $\{220\}$ NiO planes. To better distinguish Ni from NiO domains, dark field images were acquired by putting TEM objective aperture in correspondence of both $\{200\}$ Ni and $\{200\}$ NiO diffraction rings (Figure 5.7(b)), and in correspondence of the $\{220\}$ NiO diffraction ring (Figure 5.7(c)) in the SAED pattern (all images shown in Figure 5.7 were acquired from the same region of the sample). It should be underlined that even by employing the smallest TEM objective aperture it was not possible to separate the diffraction rings corresponding to $\{200\}$ Ni and $\{200\}$ NiO, whose distance in the SAED pattern is smaller than the objective aperture diameter (inset in Figure 5.7(b)). Both large ($\sim 20 \text{ nm}$) and small ($\sim 3\text{-}4 \text{ nm}$) crystalline grains show high contrast in Figure 5.7(b), while Figure 5.7(c) evidences only the presence of the small ones. In particular the large particle underlined in Figure 5.7(b) is not visible in Figure 5.7(c) where it appears surrounded by small nanocrystals. Moreover, the size of the large grains is consistent with that of the Ni nanoparti-

cles, while the size of the small ones is comparable with the thickness of the NiO/Ni(OH)₂ shell. In conclusion, this dark field analysis strongly support that these core-shell nanostructure is formed by Ni crystalline grains surrounded by a ~3-4 nm thick NiO/Ni(OH)₂ shell.

Finally, it worth to be noted that both HR-TEM and dark field techniques are sensitive to the crystallography of nanomaterials. Thus, to corroborate the conclusions drawn so far, a chemical analysis at the nanoscale level was conducted by means of STEM-EELS applied to a ten of nanoparticles. First of all, the high energy EELS spectrum of each nanoparticle was acquired; as expected it shows an edge at 532 eV, corresponding to the O_K ionization shell, and an edge at 855 eV corresponding to the Ni_L shell (Figure 5.8(a)). Secondly, the elemental mapping of Ni and O was generated based on this spectrum (Figure 5.8(b)). It clearly demonstrates that the core shell structure is composed by a Ni core surrounded by an uniform NiO shell, in strong agreement with the HR-TEM investigation.

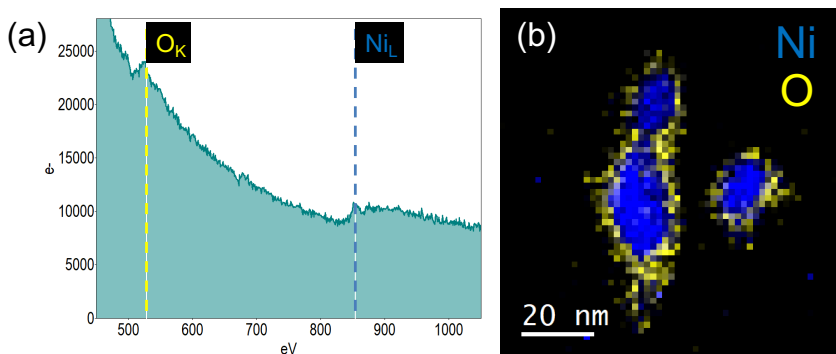


Figure 5.8: (a) EELS spectrum and (b) spectrum imaging of some core-shell nanoparticles of Ni(OH)₂@Ni core-shell nanochains (Ni in blue colour, O in yellow colour) [5.23].

Accurate mass measurements of the active material are required to properly evaluate its energy storage performances and to allow a straightforward comparison with other materials. The obtained results are reported in Table 5.1.

Ni(OH)₂ nanowalls mass was measured as the mass difference of samples before and after CBD, finding $1.68 \pm 0.04 \text{ mg cm}^{-2}$.

Ni(OH)₂ shell mass measurement is more complicate, however two different strategies have been used, giving similar results. First, Ni nanoparticles mass was measured as the mass difference of samples before CBD and after thermal annealing (Table 5.1). Once assumed that the mass difference between Ni(OH)₂@Ni core-shell nanochains and Ni nanoparticles ($\Delta m \text{ [g cm}^{-2}\text{]}$) is due to OH⁻ ions incorporation, Ni(OH)₂ shell mass can be estimated by the following equation

$$m_{Ni(OH)_2 \text{ shell (estimated)}} = \frac{\Delta m}{2M_{OH^-}} M_{Ni(OH)_2} \quad (5.2)$$

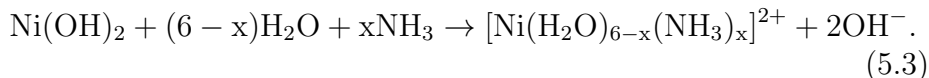
where M_{OH^-} and $M_{Ni(OH)_2}$ are the molar masses of OH⁻ (17.0 g mol⁻¹) and Ni(OH)₂ (92.7 g mol⁻¹), respectively. A value of $0.47 \pm 0.05 \text{ mg cm}^{-2}$ was found.

Sample	Specific mass [mg cm ⁻²]	#Ni [10 ¹⁸ atoms cm ⁻²]	#Ni [%]
Ni(OH) ₂ nanowalls	1.68 ± 0.04	10.9	/
Ni nanoparticles	0.85 ± 0.01	8.7	100
Ni(OH) ₂ @Ni core-shell nanochains	1.02 ± 0.04	/	/
Ni(OH) ₂ shell (experimental)	0.43 ± 0.01	2.8	32
Ni(OH) ₂ shell (estimated)	0.47 ± 0.05	3.1	36
Ni core (estimated)	0.55 ± 0.09	5.6	64

Table 5.1: Mass measurements.

Secondly, Ni(OH)₂ shell mass was measured experimentally following the procedure proposed by Dai et al., leading to a more accurate estimation [5.14]. Ni(OH)₂@Ni core-shell nanochains were immersed in a 10 M ammonia solution for 24 hours at room temperature. Since ammonia molecules coordinate Ni²⁺ ions, forming the

nickel ammonia complex, $\text{Ni}(\text{OH})_2$ dissolves [5.25]:



Therefore, $\text{Ni}(\text{OH})_2$ shell mass was further evaluated as the mass difference before and after immersion in the ammonia solution. A value of 0.434 mg cm^{-2} was obtained, which is consistent with the expected one. In this way a possible contribution due to the electrochemical oxidation of the Ni foam substrate is also considered, leading to more reliable results.

Ni areal density [$10^{18} \text{ atoms cm}^{-2}$] was calculated for the different samples and reported in Table 5.1. It was estimated that 36% Ni of Ni nanoparticles was consumed to form the $\text{Ni}(\text{OH})_2$ shell. The remaining Ni atoms (64%) constitute the highly conductive 3D backbone.

5.3.2 Energy storage performances

To demonstrate the superior energy storage performances provided by the core-shell architecture, $\text{Ni}(\text{OH})_2$ nanowalls (labelled “nanowalls”) and $\text{Ni}(\text{OH})_2@ \text{Ni}$ core-shell nanochains (labelled “core-shell”) electrodes were tested and compared.

CV was employed to identify the energy storage mechanism of nanowalls and core-shell. Figure 5.9 compares the CV curves of the two electrodes at 1 mV s^{-1} scan rate in 1 M KOH .

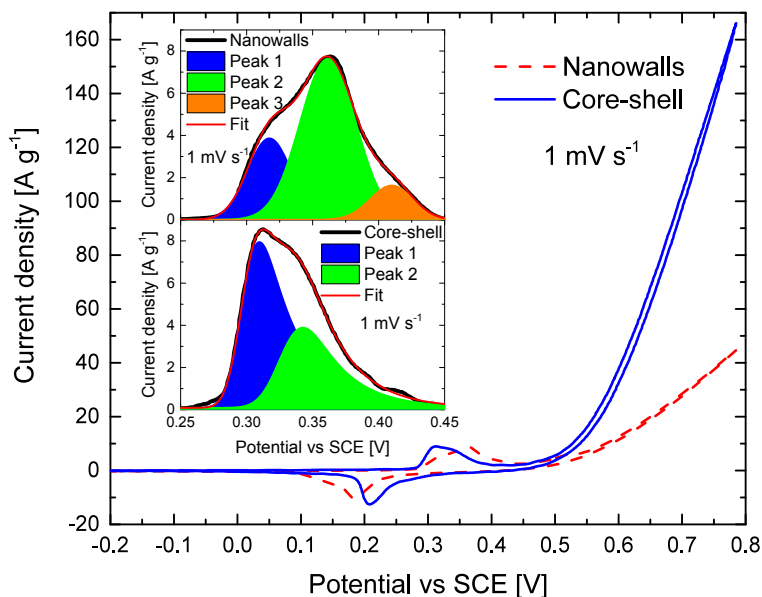


Figure 5.9: CV curves of nanowalls (red dashed line) and core-shell (blue solid line) recorded at 1 mV s^{-1} scan rate in the potential range $-0.2 \div 0.8 \text{ V}$ in 1 M KOH . The inset shows the fitted oxidation peak of nanowalls (top) and core-shell (bottom) [5.23].

Both curves are very distinct from the classic rectangular shape of EDLCs (Figure 5.2), showing instead the characteristic faradaic redox peaks of battery-type materials [5.3–5]. The inset in Figure 5.9 reports an enlarged scale of the oxidation peak, revealing clear differences among the two electrodes. The oxidation peak of nanowalls (top inset in Figure 5.9) was fitted by a three-component model: peak 1 at $\sim 0.320 \text{ V}$, peak 2 at $\sim 0.360 \text{ V}$ and peak 3 at $\sim 0.410 \text{ V}$. Instead, the oxidation peak of core-shell (bottom inset in Figure 5.9) was fitted by a two-component model: peak 1 at $\sim 0.310 \text{ V}$, and peak 2 at ~ 0.340

V. Typically, CV peaks of Ni-based electrodes are associated to the redox reactions $\alpha\text{-Ni(OH)}_2 \rightleftharpoons \gamma\text{-NiOOH}$ and $\beta\text{-Ni(OH)}_2 \rightleftharpoons \beta\text{-NiOOH}$ [5.26, 27]. $\alpha\text{-Ni(OH)}_2$ is oxidized to $\gamma\text{-NiOOH}$ at a lower potential than $\beta\text{-Ni(OH)}_2$ is oxidized to $\beta\text{-NiOOH}$ [5.28]. Therefore, it can be reasonably concluded that peak 1 is related to $\gamma\text{-NiOOH}$ formation, while peak 2 and 3 are related to $\beta\text{-NiOOH}$ formation. Consequently, the reduction peaks of nanowalls (~ 0.180 V) and core-shell (~ 0.210 V) are attributed to the totally overlapped components of $\alpha\text{-Ni(OH)}_2$ and $\beta\text{-Ni(OH)}_2$ formation.

CV curves were also recorded at higher scan rates (Figure A18). Contrary to nanowalls, the shape of core-shell CV does not change significantly with increasing scan rate. This suggests a low equivalent series resistance (ESR), which is the combined resistance of electrolyte and internal resistance of the sample [5.17]. As the scan rate increases, the oxidation and reduction peaks shift towards more positive and negative values, respectively. However, core-shell always presents a smaller separation among oxidation and reduction peaks than nanowalls, which is commonly associated to a better redox reversibility [5.26].

The specific capacity (electrode capacity divided by the mass of the active material) [mAh g^{-1}] is the most informative property to describe and compare the energy storage ability of different materials. GCD tests from 0.4 to 0 V at different current densities (Figure A19) were performed to evaluate the specific capacity of nanowalls and core-shell. Figure 5.10 compares the discharge profiles of the two samples at 16 A g^{-1} . A voltage plateau is present in both curves, confirming the battery-type behaviour resulted from CV [5.3–5]. The voltage drop (IR drop) at the beginning of the discharge curves results from the ESR, which is the main contribution to energy and power loss at high charge-discharge rates. Core-shell clearly shows a lower IR drop, and thus a smaller ESR in agreement with CV measurements.

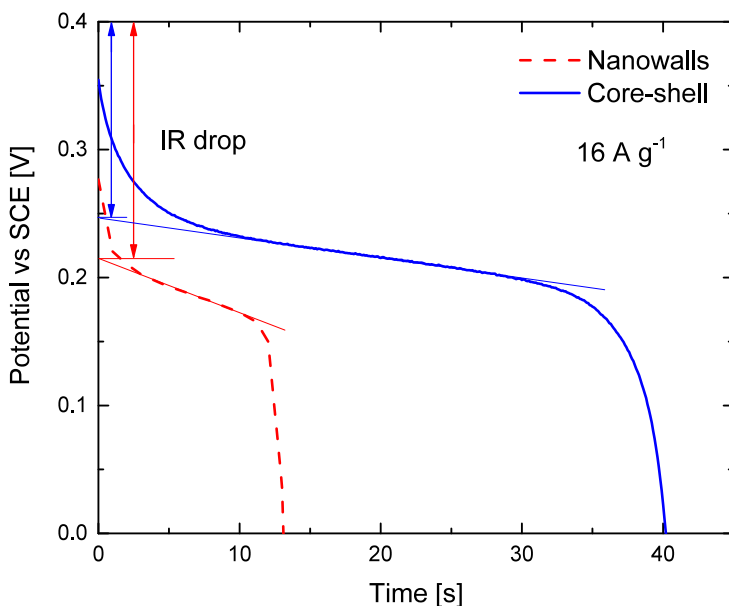


Figure 5.10: Discharge curves of nanowalls (red dashed line) and core-shell (blue solid line) measured at 16 A g^{-1} current density in 1 M KOH [5.23].

The specific capacity Q_s [mAh g^{-1}] of the two electrodes was calculated by [5.5]

$$Q_s = \frac{I \Delta t}{3.6 m} \quad (5.4)$$

where I is the constant current density [A cm^{-2}], Δt is the discharge time [s] and m is the specific mass of the active material [g cm^{-2}]. Figure 5.11(b) reports the specific capacity of the electrodes as function of current density. The specific capacity decreases with increasing current density. However, nanowalls shows a specific capacity of 176

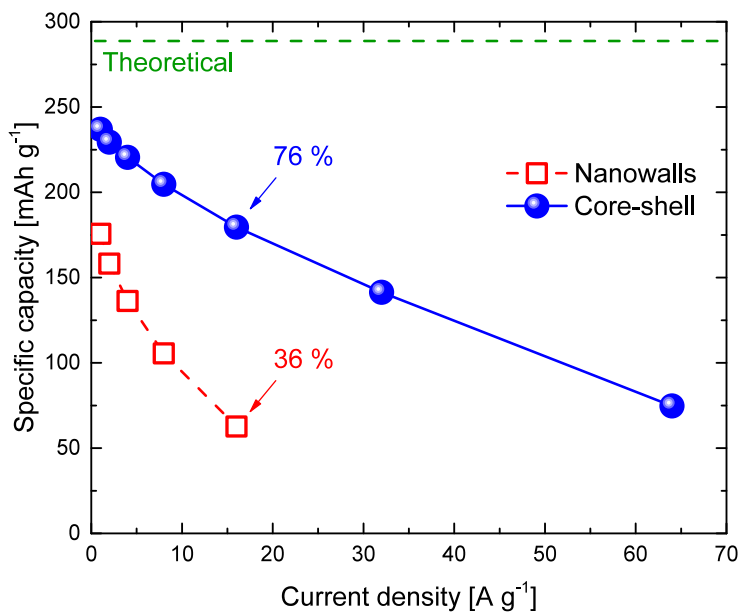


Figure 5.11: Specific capacity of nanowalls (red open squares) and core-shell (blue spheres) as function of current density as obtained by GCD curves [5.23].

mAh g⁻¹ at 1 A g⁻¹ and 63 mAh g⁻¹ at 16 A g⁻¹, retaining 36%. Instead, core-shell shows a specific capacity of 237 mAh g⁻¹ at 1 A g⁻¹ and 180 mAh g⁻¹ at 16 A g⁻¹, retaining 76%. The superior rate capability of core-shell enabled even higher current densities. In particular, at the high current density of 64 A g⁻¹ the specific capacity of core shell was still higher than nanowalls at 16 A g⁻¹.

The specific capacity was also calculated from CV measurements (Figure A20). The obtained results are consistent with those of GCD tests, indicating that core-shell has a superior charge storage ability

than nanowalls, especially when high charge-discharge rates are considered.

The electrochemical utilization z [%] of the active material can be calculated from GCD tests according to the following equation [5.29]

$$z = 3.6 Q_s \frac{M_{Ni(OH)_2}}{F} 100 \quad (5.5)$$

where Q_s is the specific capacity [mAh g⁻¹], $M_{Ni(OH)_2}$ is the molar mass of Ni(OH)₂ (92.7 g mol⁻¹) and F is the Faraday constant (96485 C mol⁻¹). $z = 100\%$ means that the whole active material undergoes redox reactions. The z values of nanowalls and core-shell at different current densities are reported in Table 5.2.

Current density [A g ⁻¹]	z [%]	
	Nanowalls	Core-shell
1	61	82
2	55	79
4	47	76
8	37	71
16	22	62
32	/	49
64	/	26

Table 5.2: Electrochemical utilization of the active material z [%] in nanowalls and core-shell, as obtained by equation 5.5 [5.23].

At 1 A g⁻¹ 61% and 82% Ni(OH)₂ are used in nanowalls and core-shell, respectively. Such a difference is even more pronounced at higher current densities, as expected from Figure 5.11. In fact, at 16 A g⁻¹ only 22% Ni(OH)₂ is used in nanowalls, while 62% in core-shell is still involved in the redox process. This result indicates an improved electrochemical utilization of the active material in core-shell.

Ni-based electrodes suffer from significant capacity decay during charge-discharge cycles because redox reactions are involved [5.2]. Since a long cycling stability is critical for the applications, a cycling stability test was performed by 1000 GCD cycles at the high current density of 16 A g^{-1} . Figure 5.12(a) compares the cycling characteristics of nanowalls and core-shell. After 1000 cycles, nanowalls

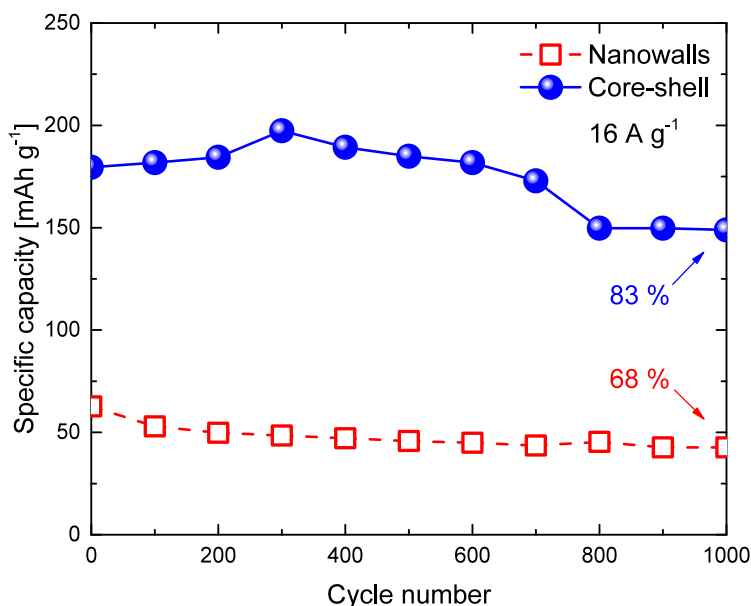


Figure 5.12: Cycling stability tests of nanowalls (red open squares) and core-shell (blue spheres) for 1000 GCD cycles at 16 A g^{-1} current density in 1 M KOH [5.23].

presents a specific capacity of 43 mAh g^{-1} , retaining only 68% of the initial capacity. This capacity decay can be explained by crystals size growth, leading to a surface area decrease, and to Ni(OH)_2 flaking off

caused by the volume change during charge-discharge, as indicated by SEM analysis after cycling test (Figure A21) [5.28]. Instead, core-shell shows first a rise in specific capacity (1-300 cycles) attributed to the fully activation of the Ni core, followed by a decay (300-800 cycles), and finally a nearly constant capacity (800-1000 cycles). The capacity decay from cycle 300 to 1000 can not be ascribed to morphological variations as demonstrated by SEM analysis after cycling tests (Figure A21). To explain this behaviour it should be noted that α -Ni(OH)₂ ⇌ γ -NiOOH contributes more than β -Ni(OH)₂ ⇌ β -NiOOH to the energy storage process in core-shell (inset in Figure 5.9). In addition, β -Ni(OH)₂ ⇌ β -NiOOH has a lower theoretical capacity than α -Ni(OH)₂ ⇌ γ -NiOOH [5.28, 30, 31]. However, α -Ni(OH)₂ is unstable in water and typically recrystallizes into β -Ni(OH)₂ with cycling (ageing) [5.27, 32]. Therefore, it can be reasonably concluded that the α -Ni(OH)₂ → β -Ni(OH)₂ transformation is responsible for capacity decay in core-shell. The full transformation into β -Ni(OH)₂ after 800 cycles determines a nearly constant capacity of 149 mAh g⁻¹ (83% of the initial capacity). This value is higher than nanowalls specific capacity after 1000 cycles, indicating a better cycling stability of core-shell.

The specific energy ρ_E [Wh kg⁻¹] and specific power ρ_P [kW kg⁻¹] of nanowalls and core-shell were calculated by using the following equations [5.1]

$$\rho_E = \frac{I}{3.6 m} \int V(t) dt \quad (5.6)$$

$$\rho_P = 3.6 \frac{\rho_E}{\Delta t} \quad (5.7)$$

where I is the constant current density [A cm⁻²], m is the specific mass of the active material [g cm⁻²], $V(t)$ is the discharge potential [V], Δt is the discharge time [s]. Figure 5.13 compares the Ragone plots of nanowalls and core-shell with other energy storage technologies. Both samples show excellent energy storage performances in terms of high specific energy and power, and are very close to the top-right corner

of the Ragone plot. In particular, at $\sim 3 \text{ kW kg}^{-1}$ specific power, the specific energy of core-shell ($\sim 40 \text{ Wh kg}^{-1}$) is ~ 4 times higher than nanowalls ($\sim 10 \text{ Wh kg}^{-1}$), while at $\sim 10 \text{ Wh kg}^{-1}$ specific energy, the specific power of core-shell ($\sim 9 \text{ kW kg}^{-1}$) is ~ 3 times higher than nanowalls ($\sim 3 \text{ kW kg}^{-1}$). These results further confirm the superior energy storage performances of core-shell.

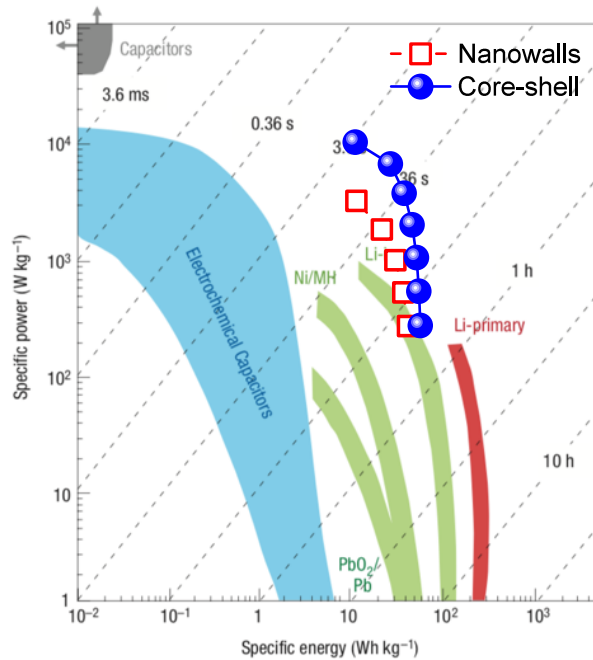


Figure 5.13: Ragone plot (specific power against specific energy) of nanowalls (red open squares) and core-shell (blue spheres), calculated by using equation 5.6 and 5.7 (adapted from the figure in ref. [5.2]).

5.3.3 Energy storage mechanism

To consolidate the improved energy storage properties of core-shell, EIS analysis was performed. Figure 5.14 compares the Nyquist plots (imaginary versus real part of the impedance) of nanowalls and core-shell, with an enlarged scale for core-shell at high frequencies (inset).

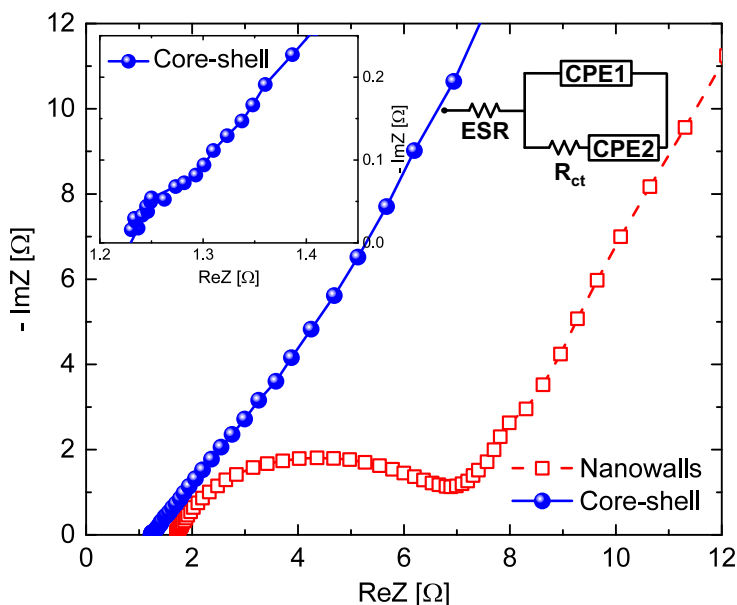


Figure 5.14: Nyquist plots of nanowalls (red open squares) and core-shell (blue spheres) recorded at 0 V vs open circuit potential with a 5 mV superimposed sinusoidal voltage in the frequency range $10^4 \div 10^{-2}$ Hz in 1 M KOH solution (the inset is the magnified high-frequency region of core-shell). The equivalent circuit model for the Nyquist plots is also reported [5.23].

The two Nyquist plots show a semicircle arc in the high-frequency

region and a straight line in the low-frequency region. This shape can be modelled by the equivalent circuit model reported in Figure 5.14, formed by an equivalent series resistance (ESR) connected in series with a constant phase element (CPE1), which is in parallel with the charge transfer resistance (R_{ct}) and a constant phase element (CPE2). The slopes of the two lines are similar, indicating a low ions diffusion resistance and a behaviour close to that of an ideal capacitor (line parallel to the imaginary axis). ESR can be evaluated as the intercept on the real axis of the Nyquist plot. The lower ESR of core-shell ($\sim 1.2 \Omega$) than nanowalls ($\sim 1.7 \Omega$) is due to the presence of the Ni core, which results in a smaller IR drop in the discharge curves for fixed current density (Figure 5.10). R_{ct} can be measured as the diameter of the semicircle in the high-frequency region. It can be seen that core-shell has a lower R_{ct} ($\sim 0.1 \Omega$) than nanowalls ($\sim 5.4 \Omega$).

To explain the excellent electrochemical behaviour of core-shell, the electric field in nanowalls and core-shell was simulated by using COMSOL Multiphysics software. Nanowalls was simulated by a 20 nm thick $\text{Ni}(\text{OH})_2$ nanosheet, while core-shell was simulated by a 17 nm thick Ni nanosheet surrounded by a 3 nm thick $\text{Ni}(\text{OH})_2$ shell, both on Ni substrates. The following room temperature conductivities were also considered: $10^{-13} \text{ S cm}^{-1}$ for $\text{Ni}(\text{OH})_2$, 10^5 S cm^{-1} for Ni, and 0.2 S cm^{-1} for 1 M KOH [5.32, 33]. A steady-state model was used to evaluate the electric field in the two structures at an applied voltage of 0.4 V. The resulted electric field module distributions are reported in Figure 5.15 in false colour scale from 0 to $1.5 \times 10^8 \text{ V m}^{-1}$. Nanowalls displays a moderate electric field ($\sim 0.4 \times 10^8 \text{ V m}^{-1}$) near the substrate interface, which is dramatically reduced with increasing distance from the substrate. On the contrary, the conductive Ni core in core-shell provides a uniform and enhanced electric field ($\sim 0.8 \times 10^8 \text{ V m}^{-1}$) along the entire shell, in agreement with the improved electrochemical utilization reported in Table 5.2.

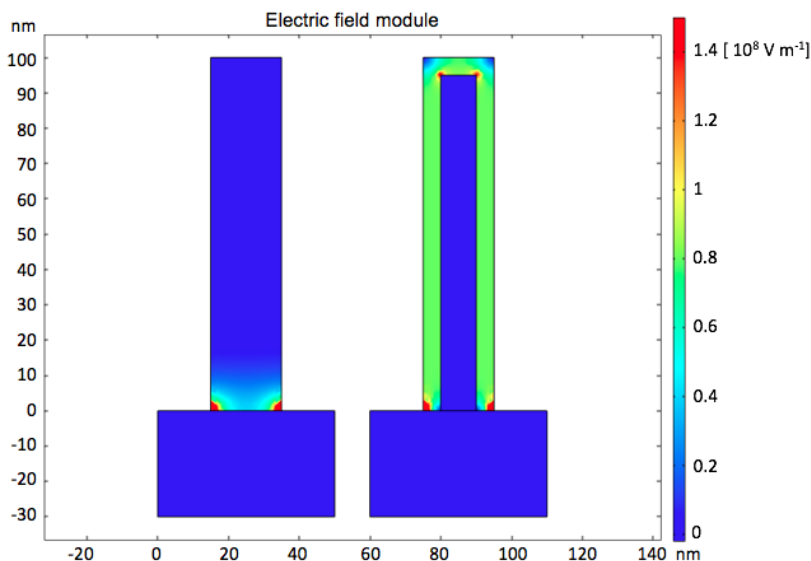


Figure 5.15: Electric field module distribution in nanowalls (left) and core-shell (right) in 1 M KOH solution at an applied voltage of 0.4 V, as simulated by COMSOL Multiphysics software [5.23].

Based on the aforementioned results, the following model was developed to explain the improved specific capacity, rate capability and cycling stability of $\text{Ni}(\text{OH})_2@\text{Ni}$ core-shell nanochains:

- the Ni core reduces ESR (thus the energy dissipation) and R_{ct} . Furthermore, it enhances the electric field in the whole $\text{Ni}(\text{OH})_2$ shell, leading to an improved electrochemical utilization of the active material. These features result in higher charge storage ability and faster redox process;
- the 3 nm thin $\text{Ni}(\text{OH})_2$ shell shortens electrons migration paths to the current collector (schematic illustration in Figure 5.16), supporting high charge-discharge rates;

- a high OH^- ions diffusion coefficient of $(1.415 \pm 0.002) \times 10^{-6} \text{ cm}^2 \text{ s}^{-1}$ was estimated based on the Randles-Sevcik equation (Figure A22 [5.34]). This value is higher than $2.491 \times 10^{-7} \text{ cm}^2 \text{ s}^{-1}$ reported for $\text{Ni}(\text{OH})_2/\text{graphene}$ nanosheets [5.15]. Therefore, OH^- ions have sufficient time to reach and activate also inner $\text{Ni}(\text{OH})_2$ sites;
- the thermal annealing and in situ electrochemical oxidation allow a good contact between Ni core and substrate, as well as $\text{Ni}(\text{OH})_2$ shell and Ni core. As a consequence, $\text{Ni}(\text{OH})_2$ can easily relax the volume change during charge-discharge cycles, showing a better cycling stability.

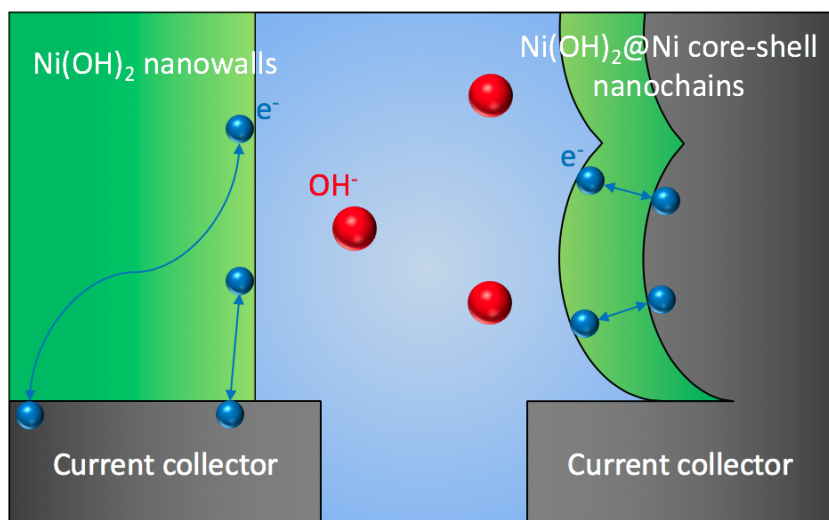


Figure 5.16: Schematic illustration of the electron transport in $\text{Ni}(\text{OH})_2$ nanowalls and $\text{Ni}(\text{OH})_2@$ Ni core-shell nanochains [5.23].

Table 5.3 compares the energy storage performances of recent Ni-based nanostructured electrodes. An excellent capacity retention at high charge-discharge rate is required for the development of commercial hybrid supercapacitors. From Table 5.3 it can be seen that

even at a high charge-discharge current density $\text{Ni}(\text{OH})_2@ \text{Ni}$ core-shell nanochains show higher specific capacity than most of the previous reports [5.11, 17, 35–38]. A few electrodes present comparable specific capacity values, but measured at a lower current density [5.18, 39]. Su et al. reported a similar $\text{Ni}(\text{OH})_2@ \text{Ni}$ core-shell electrode with a higher specific capacity but lower rate capability [5.19], while Jiang and co-workers obtained a specific capacity higher than $\text{Ni}(\text{OH})_2$ theoretical limit by using a $\text{NiMoO}_4@ \text{Ni}(\text{OH})_2$ core-shell electrode where both core and shell are active materials [5.40]. The good cycling stability of $\text{Ni}(\text{OH})_2@ \text{Ni}$ core-shell nanochains can be further improved by using graphene nanosheets [5.15] or carbon nanotubes as current collectors [5.36].

Year	Electrode material	Fabrication	Specific capacity [mAh g ⁻¹]	Current density [A g ⁻¹]	Cycling stability Cycle number	Retention [%]	Ref.
2014	Au NP-deposited Ni(OH) ₂	Hydrothermal + colloidal deposition	~142	20	5000	80	[5.35]
2014	Ni(OH) ₂ nanosheets on Ni foam	Wet environment + solution oxidation	~179	5	3000	75	[5.39]
2014	Amorphous Ni(OH) ₂ @3D core-shell nanostructures	Electrodeposition	~269	20	3000	30	[5.19]
2015	Ni@NiO core-shell nanoparticles	Electrodeposition + oxidation	~110	25	1000	92	[5.20]
2015	3D TiO ₂ @Ni(OH) ₂ core-shell arrays	Hydrothermal + annealing + CBD	178	10	/	/	[5.18]
2015	CNT@Ni(OH) ₂ core-shell composites	CBD	~53	20	1000	92	[5.36]
2015	NiMoO ₄ @Ni(OH) ₂ core/shell nanorods	Hydrothermal + electrodeposition	~328	16	1000	72	[5.40]
2016	3D flower-like β-Ni(OH) ₂	Solvothermal	~37	10	600	90	[5.11]
2016	Ni(OH) ₂ /graphene nanosheets	Carbonization + hydrothermal	~156	10	1000	97	[5.15]
2017	Ni-Co double hydroxide	Electrodeposition	~140	20	5000	96	[5.37]
2018	Ni(OH) ₂ nanosheets on hollow mesoporous carbon spheres	Solvothermal + precipitation	~154	10	3000	81	[5.38]
2019	Ni(OH) ₂ nanowalls	CBD	63	16	1000	68	[5.21]
2019	Ni(OH) ₂ @Ni nanochains	CBD + annealing + CV	180	16	1000	83	[5.21]

Table 5.3: Energy storage performances of recent Ni-based nanostructures (specific capacity [mAh g⁻¹] values with “~” were calculated from specific capacitance [F g⁻¹] values reported in the corresponding references) [5.23].

5.4 Conclusions

Novel Ni(OH)₂@Ni core-shell nanochains with promising high-rate energy storage performances were reported. The core-shell structure consists of a 3D nanostructured and porous Ni core, surrounded by a thin Ni(OH)₂ shell. The Ni core is formed by interconnected chains-like clusters of Ni nanoparticles (20-30 nm), grown by low-cost CBD of Ni(OH)₂ nanowalls and thermal annealing in reducing atmosphere. The Ni(OH)₂ shell is made of nanocrystalline grains (3-4 nm), obtained by in situ electrochemical oxidation of Ni nanoparticles surface. The electrochemical behaviour of Ni(OH)₂@Ni core-shell nanochains is dominated by faradaic redox processes (battery-type signature), which enabled a high specific capacity of 237 mAh g⁻¹ at 1 A g⁻¹, a high rate capability (76% retention at 16 A g⁻¹, 32% at 64 A g⁻¹), and good stability (83% retention after 1000 charge-discharge cycles at 16 A g⁻¹). These remarkable features if compared with those of similar NiO and Ni(OH)₂-based nanostructures are attributed to the high surface area, faster electron transport, enhanced electric field and improved utilization of the active material provided by the core-shell architecture. As a result, Ni(OH)₂@Ni core-shell nanochains have potential in many applications, including hybrid supercapacitors, batteries, electrochemical (bio)sensing, gas sensing and photocatalysis. Finally, the reported low-cost preparation of core-shell nanostructures can be applied also to all other existing NiO and Ni(OH)₂-based material, in such a way to improve their electrochemical properties.

References

- [5.1] S. Zhang and N. Pan, Supercapacitors Performance Evaluation, *Advanced Energy Materials* **5**, 1401401 (2015).
- [5.2] P. Simon and Y. Gogotsi, Materials for electrochemical capacitors, *Nature Materials* **7**, 845 (2008).

- [5.3] P. Simon, Y. Gogotsi, and B. Dunn, Where Do Batteries End and Supercapacitors Begin?, *Science* **343**, 1210 (2014).
- [5.4] T. Brousse, D. Bélanger, and J. W. Long, To Be or Not To Be Pseudocapacitive?, *Journal of The Electrochemical Society* **162**, A5185 (2015).
- [5.5] A.-L. Brisse, P. Stevens, G. Toussaint, O. Crosnier, and T. Brousse, Ni(OH)₂ and NiO Based Composites: Battery Type Electrode Materials for Hybrid Supercapacitor Devices, *Materials* **11**, 1178 (2018).
- [5.6] W. Zuo, R. Li, C. Zhou, Y. Li, J. Xia, and J. Liu, Battery-Supercapacitor Hybrid Devices: Recent Progress and Future Prospects, *Advanced Science* **4**, 1600539 (2017).
- [5.7] N. A. Alhebshi, R. B. Rakhi, and H. N. Alshareef, Conformal coating of Ni(OH)₂ nanoflakes on carbon fibers by chemical bath deposition for efficient supercapacitor electrodes, *Journal of Materials Chemistry A* **1**, 14897 (2013).
- [5.8] Y. Liu, R. Wang, and X. Yan, Synergistic Effect Between Ultra-Small Nickel Hydroxide Nanoparticles and Reduced Graphene Oxide Sheets for the Application in High-Performance Asymmetric Supercapacitor, *Scientific Reports* **5**, 11095 (2015).
- [5.9] L. Li, X. Liu, C. Liu, H. Wan, J. Zhang, P. Liang, H. Wang, and H. Wang, Ultra-long life nickel nanowires@nickel-cobalt hydroxide nanoarrays composite pseudocapacitive electrode: Construction and activation mechanism, *Electrochimica Acta* **259**, 303 (2018).
- [5.10] Z. Li, W. Zhang, Y. Liu, J. Guo, and B. Yang, 2D nickel oxide nanosheets with highly porous structure for high performance capacitive energy storage, *Journal of Physics D: Applied Physics* **51**, 045302 (2018).

- [5.11] N. Parveen and M. H. Cho, Self-Assembled 3D Flower-Like Nickel Hydroxide Nanostructures and Their Supercapacitor Applications, *Scientific Reports* **6**, 27318 (2016).
- [5.12] Z. Lu, Z. Chang, W. Zhu, and X. Sun, Beta-phased Ni(OH)₂ nanowall film with reversible capacitance higher than theoretical Faradic capacitance, *Chemical Communications* **47**, 9651 (2011).
- [5.13] M. M. Sk, C. Y. Yue, K. Ghosh, and R. K. Jena, Review on advances in porous nanostructured nickel oxides and their composite electrodes for high-performance supercapacitors, *Journal of Power Sources* **308**, 121 (2016).
- [5.14] X. Dai, D. Chen, H. Fan, Y. Zhong, L. Chang, H. Shao, J. Wang, J. Zhang, and C.-N. Cao, Ni(OH)₂/NiO/Ni composite nanotube arrays for high-performance supercapacitors, *Electrochimica Acta* **154**, 128 (2015).
- [5.15] K. Wang, X. Zhang, X. Zhang, D. Chen, and Q. Lin, A novel Ni(OH)₂/graphene nanosheets electrode with high capacitance and excellent cycling stability for pseudocapacitors, *Journal of Power Sources* **333**, 156 (2016).
- [5.16] W. Jiang, S. Zhai, L. Wei, Y. Yuan, D. Yu, L. Wang, J. Wei, and Y. Chen, Nickel hydroxide–carbon nanotube nanocomposites as supercapacitor electrodes: crystallinity dependent performances, *Nanotechnology* **26**, 314003 (2015).
- [5.17] K.-N. Kang, I.-H. Kim, A. Ramadoss, S.-I Kim, J.-C. Yoon, and J.-H. Jang, Ultrathin nickel hydroxide on carbon coated 3D-porous copper structures for high performance supercapacitors, *Physical Chemistry Chemical Physics* **20**, 719 (2018).
- [5.18] Q. Ke, M. Zheng, H. Liu, C. Guan, L. Mao, and J. Wang, 3D TiO₂@Ni(OH)₂ Core-Shell Arrays with Tunable Nanostructure

for Hybrid Supercapacitor Application, *Scientific Reports* **5**, 13940 (2015).

- [5.19] Y.-Z. Su, K. Xiao, N. Li, Z.-Q. Liu, and S.-Z. Qiao, Amorphous Ni(OH)₂ @ three-dimensional Ni core-shell nanostructures for high capacitance pseudocapacitors and asymmetric supercapacitors, *Journal of Materials Chemistry A* **2**, 13845 (2014).
- [5.20] Q. Li, C.-L. Liang, X.-F. Lu, Y.-X. Tong, and G.-R. Li, Ni@NiO core-shell nanoparticle tube arrays with enhanced supercapacitor performance, *Journal of Materials Chemistry A* **3**, 6432 (2015).
- [5.21] M. Urso, G. Pellegrino, V. Strano, E. Bruno, F. Priolo, and S. Mirabella, Enhanced sensitivity in non-enzymatic glucose detection by improved growth kinetics of Ni-based nanostructures, *Nanotechnology* **29**, 165601 (2018).
- [5.22] K. O. Iwu, A. Lombardo, R. Sanz, S. Scirè, and S. Mirabella, Facile synthesis of Ni nanofoam for flexible and low-cost non-enzymatic glucose sensing, *Sensors and Actuators B: Chemical* **224**, 764 (2016).
- [5.23] M. Urso, G. Torrisi, S. Boninelli, C. Bongiorno, F. Priolo, and S. Mirabella, Ni(OH)₂@Ni core-shell nanochains as low-cost high-rate performance electrode for energy storage applications, *Scientific Reports* **9**, 7736 (2019).
- [5.24] S. L. Medway, C. A. Lucas, A. Kowal, R. J. Nichols, and D. Johnson, In situ studies of the oxidation of nickel electrodes in alkaline solution, *Journal of Electroanalytical Chemistry* **587**, 172 (2006).
- [5.25] A. Van Bommel and J. R. Dahn, Analysis of the Growth Mechanism of Coprecipitated Spherical and Dense Nickel, Manganese, and Cobalt-Containing Hydroxides in the Presence of Aqueous Ammonia, *Chemistry of Materials* **21**, 1500 (2009).

- [5.26] Y. F. Yuan, X. H. Xia, J. B. Wu, J. L. Yang, Y. B. Chen, and S. Y. Guo, Nickel foam-supported porous Ni(OH)₂/NiOOH composite film as advanced pseudocapacitor material, *Electrochimica Acta* **56**, 2627 (2011).
- [5.27] S. R. Ede, S. Anantharaj, K. T. Kumaran, S. Mishra, and S. Kundu, One step synthesis of Ni/Ni(OH)₂ nano sheets (NSs) and their application in asymmetric supercapacitors, *RSC Advances* **7**, 5898 (2017).
- [5.28] G. Hu, C. Li, and H. Gong, Capacitance decay of nanoporous nickel hydroxide, *Journal of Power Sources* **195**, 6977 (2010).
- [5.29] A. Numan, N. Duraisamy, F. Saiha Omar, D. Gopi, K. Ramesh, and S. Ramesh, Sonochemical synthesis of nanostructured nickel hydroxide as an electrode material for improved electrochemical energy storage application, *Progress in Natural Science: Materials International* **27**, 416 (2017).
- [5.30] P. Oliva, J. Leonardi, J. F. Laurent, C. Delmas, J. J. Braconnier, M. Figlarz, F. Fievet, and A. de Guibert, Review of the structure and the electrochemistry of nickel hydroxides and oxy-hydroxides, *Journal of Power Sources* **8**, 229 (1982).
- [5.31] K.-H. Young, L. Wang, S. Yan, X. Liao, T. Meng, H. Shen, and W. Mays, Fabrications of High-Capacity Alpha-Ni(OH)₂, *Batteries* **3**, 6 (2017).
- [5.32] D. S. Hall, D. J. Lockwood, C. Bock, and B. R. MacDougall, Nickel hydroxides and related materials: a review of their structures, synthesis and properties, *Proceedings of the Royal Society A: Mathematical, Physical and Engineering Sciences* **471**, 20140792 (2015).
- [5.33] R. J. Gilliam, J. W. Graydon, D. W. Kirk, and S. J. Thorpe, A review of specific conductivities of potassium hydroxide so-

lutions for various concentrations and temperatures, *International Journal of Hydrogen Energy* **32**, 359 (2007).

- [5.34] A. J. Bard and L. R. Faulkner, *Inorganic Chemistry in Focus III* (Wiley, 2001).
- [5.35] S.-I Kim, P. Thiyagarajan, and J.-H. Jang, Great improvement in pseudocapacitor properties of nickel hydroxide via simple gold deposition, *Nanoscale* **6**, 11646 (2014).
- [5.36] H. Yi, H. Wang, Y. Jing, T. Peng, Y. Wang, J. Guo, Q. He, Z. Guo, and X. Wang, Advanced asymmetric supercapacitors based on CNT@Ni(OH)₂ core-shell composites and 3D graphene networks, *Journal of Materials Chemistry A* **3**, 19545 (2015).
- [5.37] L. Gao, J. U. Surjadi, K. Cao, H. Zhang, P. Li, S. Xu, C. Jiang, J. Song, D. Sun, and Y. Lu, Flexible Fiber-Shaped Supercapacitor Based on Nickel-Cobalt Double Hydroxide and Pen Ink Electrodes on Metallized Carbon Fiber, *ACS Applied Materials & Interfaces* **9**, 5409 (2017).
- [5.38] Y. Fu, Y. Zhou, Q. Peng, C. Yu, Z. Wu, J. Sun, J. Zhu, and X. Wang, Hollow mesoporous carbon spheres enwrapped by small-sized and ultrathin nickel hydroxide nanosheets for high-performance hybrid supercapacitors, *Journal of Power Sources* **402**, 43 (2018).
- [5.39] X. Xiong, D. Ding, D. Chen, G. Waller, Y. Bu, Z. Wang, and M. Liu, Three-dimensional ultrathin Ni(OH)₂ nanosheets grown on nickel foam for high-performance supercapacitors, *Nano Energy* **11**, 154 (2015).
- [5.40] G. Jiang, M. Zhang, X. Li, and H. Gao, NiMoO₄@Ni(OH)₂ core/shell nanorods supported on Ni foam for high-performance supercapacitors, *RSC Advances* **5**, 69365 (2015).

Conclusions and perspectives

The aim of this thesis was the controlled synthesis of novel Ni-based nanostructures for application in sensing and energy storage. In particular, the chemical bath deposition (CBD) of Ni-based nanowalls-shaped thin films was carefully investigated and controlled. A model for film formation and growth was also proposed. Such a model led to an optimization of CBD parameters (50°C deposition temperature) which resulted in enhanced nanowalls physical and chemical properties.

The optimized Ni-based nanowalls were subjected to various post-growth processes to obtain low-cost Ni-based nanostructures with unique properties for specific applications:

- a novel Ni nanofoam, consisting of Ni nanoparticles (20 nm), was obtained upon annealing at 350°C in reducing atmosphere. The Ni nanofoam was applied for non-enzymatic glucose sensing, showing an unprecedentedly high sensitivity of 31 mA cm⁻² mM⁻¹ in the linear range 0.02÷0.4 mM, a very low limit of detection (LoD) of 5 μM, quick response (1-2 s), high selectivity (200 μM glucose versus 20 μM uric acid, 10 μM ascorbic acid and 10 μM acetaminophen) and long-term stability (4% response loss after 64 days). The unique performances of the Ni nanofoam make it a promising material for the development of non-invasive glucose sensor in human saliva and tears;

- novel Au decorated NiO nanowalls were obtained upon annealing at 350°C in vacuum and Au electroless deposition. They served as a low-cost and high surface area platform for *Mycoplasma agalactiae* (Ma) thiolated probe ssDNA immobilization, and then used as an impedimetric sensor of Ma complementary ssDNA. The Au decorated NiO nanowalls were able to selectively detect Ma DNA at the very low concentration of 1.7 ng μl^{-1} , opening the route towards Polymerase Chain Reaction (PCR)-free Ma detection for the early diagnosis of Contagious Agalactia in goats and sheep;
- NiO nanowalls were obtained upon annealing at 350°C in Ar and applied for acetone sensing. The response to acetone at various temperatures was recorded and modelled by two adsorption sites. At the optimal temperature of 250°, the NiO nanowalls showed high sensitivity, low LoD (~ 200 ppb) and good selectivity to acetone, which are the requirements of acetone sensors for non-invasive diagnosis of diabetes. Moreover, a novel nanoporous NiO film, consisting of NiO nanoparticles (30-50 nm) was obtained upon thermal annealing at 350°C in reducing atmosphere and at 400°C in air, and applied for NO₂ sensing at room temperature. The response to NO₂ at various temperatures and NO₂ concentrations was recorded and modelled by two adsorption sites. A NO₂-NiO sensing mechanism based on these sites was also proposed. At room temperature, the nanoporous NiO film showed high sensitivity and selectivity to sub-ppm NO₂, a LoD as low as 20 ppb and long-term stability, which are the requirements of NO₂ sensors for environmental monitoring;
- novel Ni(OH)₂@Ni core-shell nanochains were obtained upon thermal annealing in reducing atmosphere and electrochemical oxidation in alkaline solution. This core-shell architecture showed superior electrochemical properties in terms of, high specific capacity, rate capability and cycling stability, which

are promising for the development of high energy and power density hybrid supercapacitors.

Further experiments are on going to modify these novel Ni-based nanostructures by doping and decoration with other metal or semiconductor nanostructures, and apply them in other fields, among which photoelectrochemical water splitting and reduction of CO₂.

Appendix

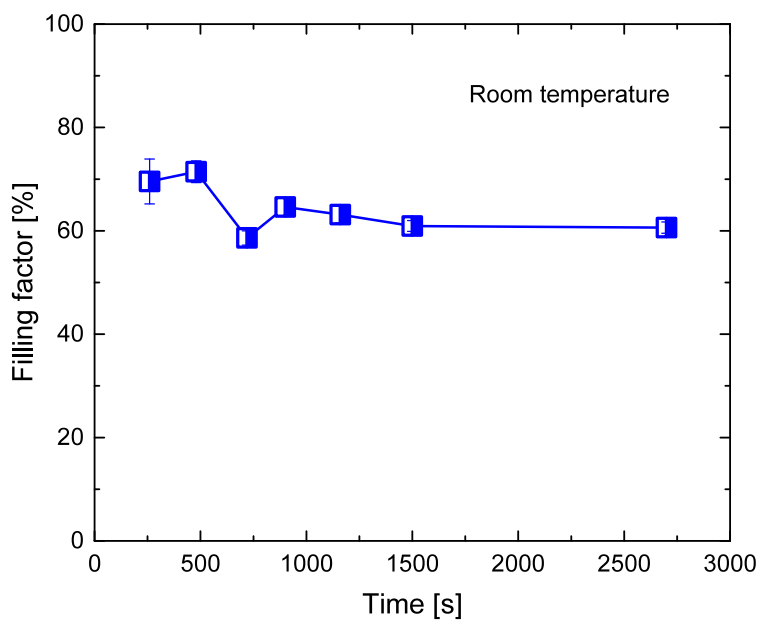


Figure A1: Filling factor versus growth time at room temperature.

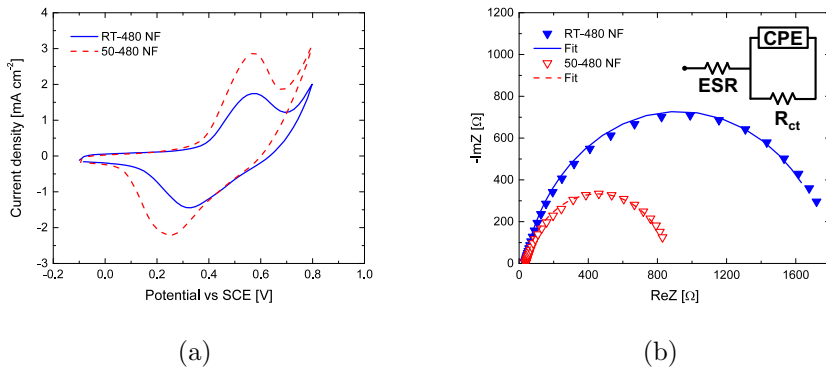


Figure A2: (a) CV curves of RT-480 NF (blue solid line) and 50-480 NF (red dashed line) recorded at 50 mV s^{-1} scan rate in the potential range $-0.1 \div 0.9 \text{ V}$ in 0.1 M NaOH . (b) Nyquist plots of RT-480 NF (blue closed triangles) and 50-480 NF (red open triangles) recorded at the oxidation potential with a 20 mV superimposed sinusoidal voltage in the frequency range $10^2 \div 10^{-2} \text{ Hz}$ in 0.1 M NaOH . Lines are fits of Nyquist plots based on the reported equivalent circuit model.

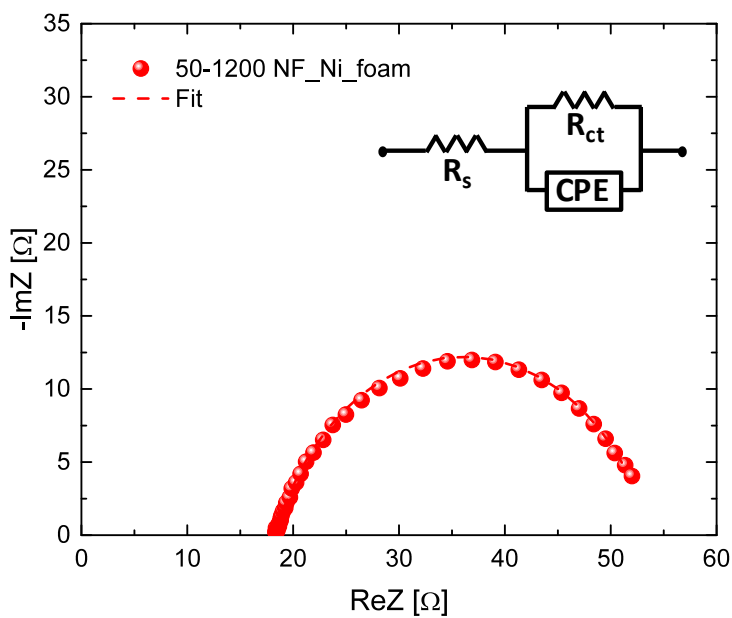


Figure A3: Nyquist plot of 50-1200 NF_Ni_foam recorded at the oxidation potential with a 20 mV superimposed sinusoidal voltage in the frequency range $10^2 \div 10^{-2}$ Hz in 0.1 M NaOH. The line is the fit of the Nyquist plot based on the reported equivalent circuit model.

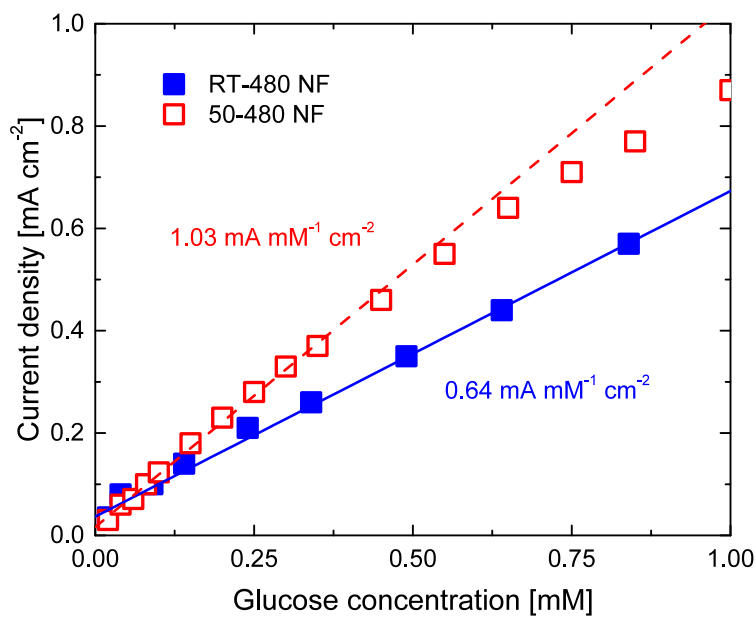


Figure A4: Calibration curves of RT-480 NF (blue closed squares) and 50-480 NF (red open squares) obtained from CA measurements in 0.1 M NaOH.

Sample	$ Z $ [Ω]	Phase(Z) [$^\circ$]
NiO nanowalls	368.8 ± 0.2	-70.6 ± 0.3
NiO/Au nanowalls	149 ± 4	-35.5 ± 0.6
NiO/Au/Ma probe ssDNA	194 ± 2	-51 ± 2
Prehybridization (1 h)	160 ± 12	-57.7 ± 0.5
Prehybridization (2 h)	103 ± 7	-62.3 ± 0.8
Prehybridization (3 h)	87 ± 9	-58 ± 1
Prehybridization (4 h)	80 ± 1	-56.67 ± 0.09
Prehybridization (5 h)	69 ± 2	-52.0 ± 0.4
Hybridization (1.7 ng μl^{-1})	79 ± 2	-55.2 ± 0.6
Hybridization (6 ng μl^{-1})	98 ± 0.2	-45 ± 1
Hybridization (14.5 ng μl^{-1})	102 ± 6	-54 ± 2
Hybridization (27.2 ng μl^{-1})	103 ± 1	-53.96 ± 0.07
Hybridization (48.5 ng μl^{-1})	104 ± 2	-50.8 ± 0.4

Table A1: Sensor impedance at 0.1 Hz at various fabrication and sensing steps.

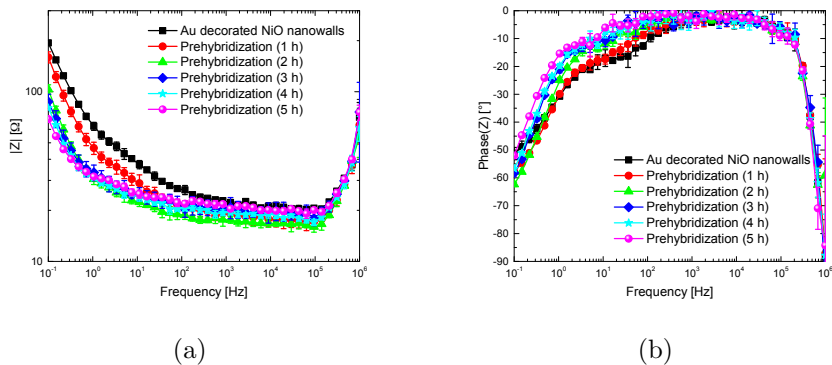
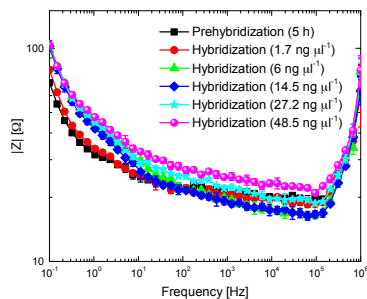
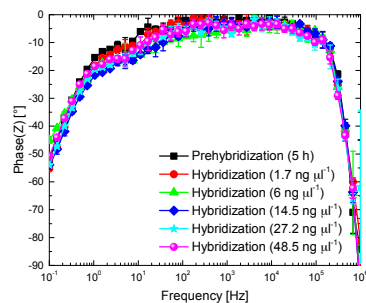


Figure A5: Bode plots ((a) impedance modulus versus frequency and (b) impedance phase versus frequency) of the sensor as function of prehybridization time with non-complementary ssDNA as obtained by EIS experiments at 0 V versus open circuit potential with 10 mV superimposed sinusoidal voltage in the frequency range $10^6 \div 10^{-1}$ Hz in PBS (pH 7) containing 10 mM $[\text{Fe}(\text{CN})_6]^{3-/4-}$.



(a)



(b)

Figure A6: Bode plots ((a) impedance modulus versus frequency and (b) impedance phase versus frequency) of the sensor upon hybridization with different concentrations of Ma complementary ssDNA as obtained by EIS experiments at 0 V versus open circuit potential with 10 mV superimposed sinusoidal voltage in the frequency range $10^6 \div 10^{-1}$ Hz in PBS (pH 7) containing 10 mM $[\text{Fe}(\text{CN})_6]^{3-/4-}$.

Linear fits of the Arrhenius plots were performed to calculate the activation energy for conduction (E_a) by using the Arrhenius equation

$$R_{air} = A \exp\left(\frac{E_a}{k T}\right) \quad (8)$$

where A is a pre-exponential factor [Ω], k is the Boltzmann constant [eV K^{-1}] and T is the temperature [K]. An activation energy of 0.35 and 0.36 eV was obtained for NiO nanowalls and nanoporous NiO film, respectively.

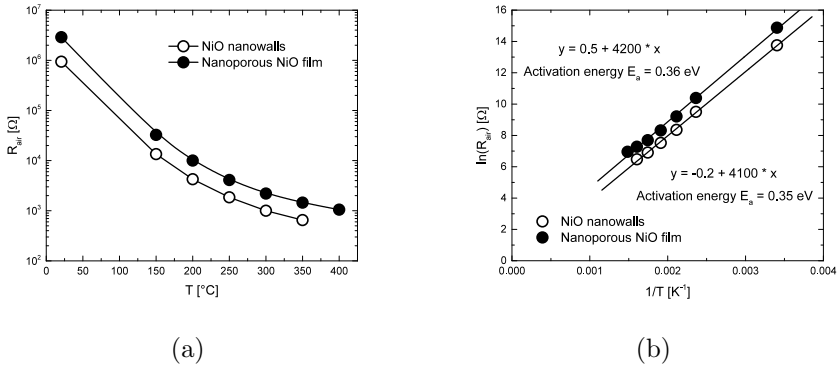
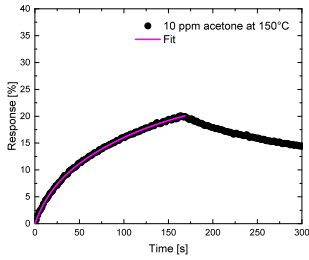
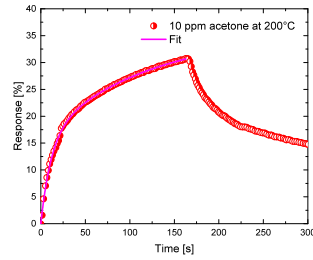


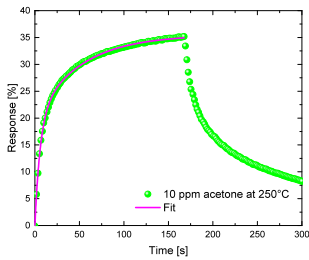
Figure A7: (a) Resistance in air as function of temperature, and (b) Arrhenius plots of NiO nanowalls (black open circles) and nanoporous NiO film (black closed circles).



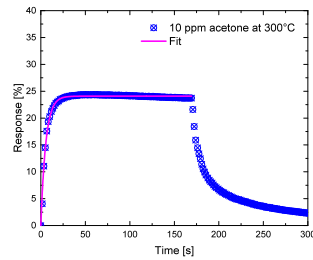
(a)



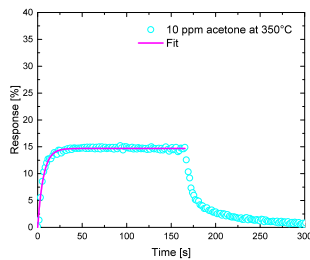
(b)



(c)

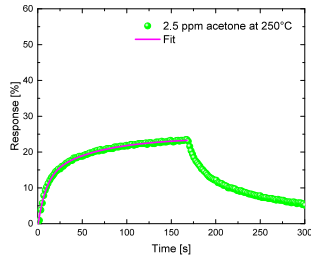


(d)

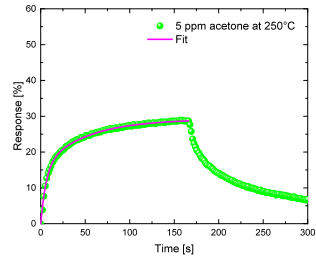


(e)

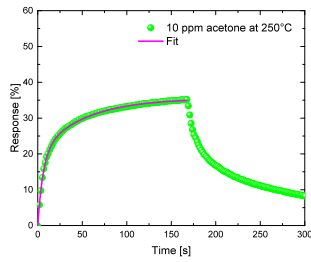
Figure A8: Fits of the response transients of a 10 ppm acetone pulse at 150°C (a), 200°C (b) and 250°C (c) based on a two-site isotherm (equation 4.3), and at 300°C (d) and 350°C (e) based on a single site isotherm (equation 4.2).



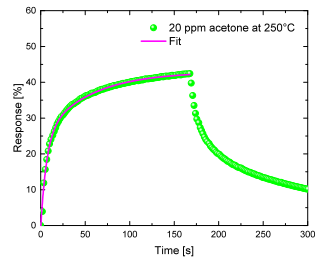
(a)



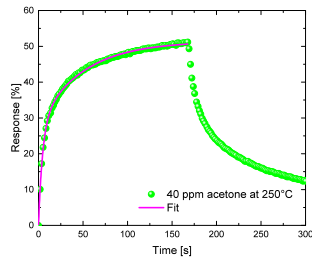
(b)



(c)



(d)



(e)

Figure A9: Fits of the response transients of 2.5 ppm (a), 5 ppm (b), 10 ppm (c), 20 ppm (d), 40 ppm (e) acetone pulses at 250°C based on a two-site isotherm (equation 4.3).

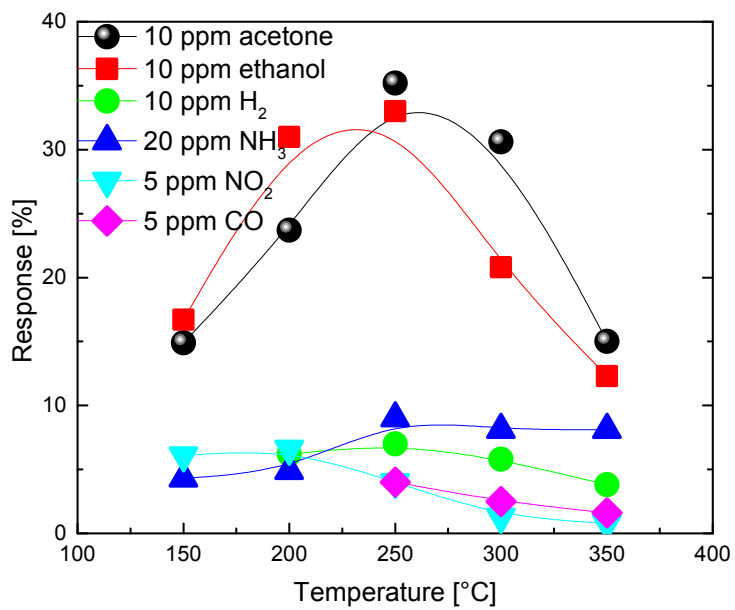


Figure A10: Selectivity tests at various temperatures.

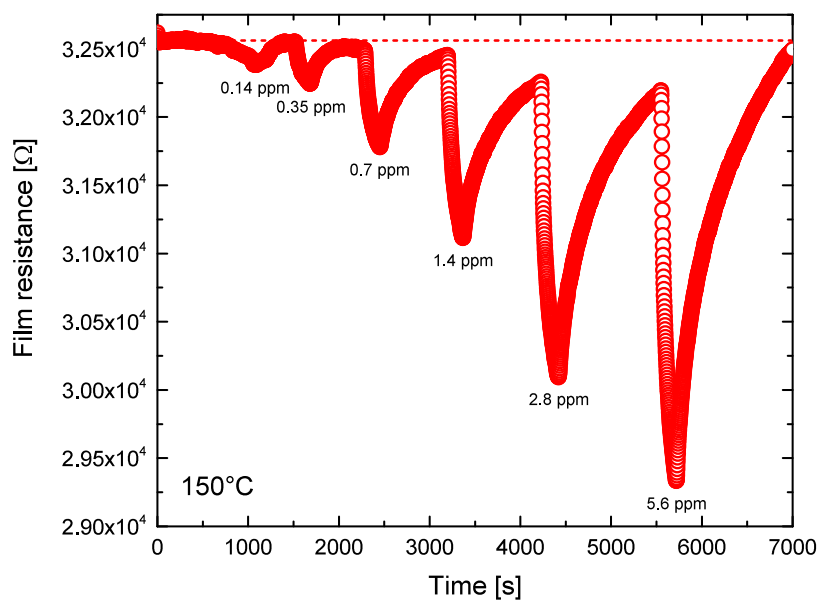


Figure A11: Dynamic responses of the sensor when exposed to different pulses of NO₂ (0.14, 0.35, 0.7, 1.4, 2.8, 5.6 ppm) at 150°C.

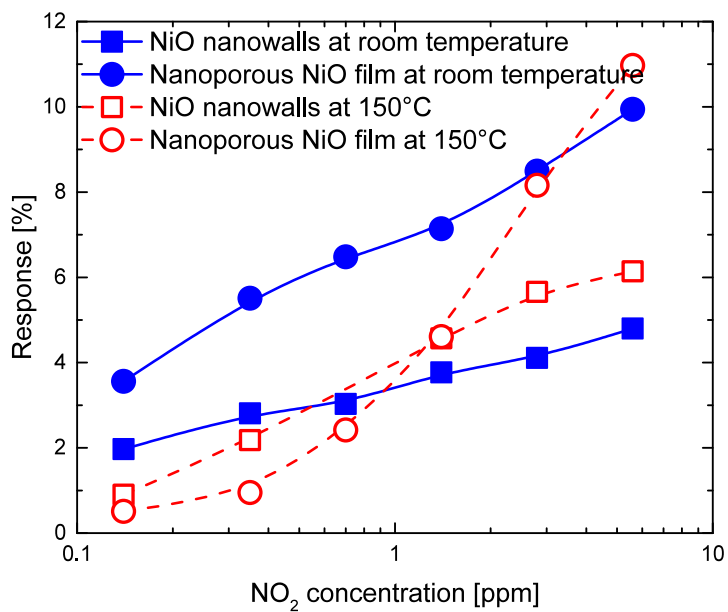
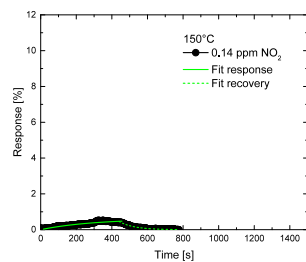
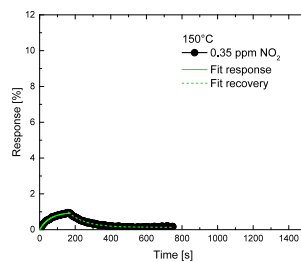


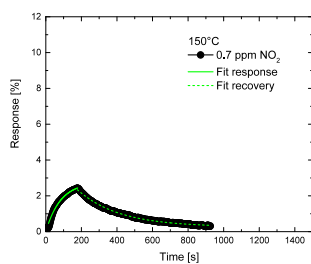
Figure A12: NO₂ calibration curves of NiO nanowalls (squares) and nanoporous NiO film (circles) at room temperature (blue closed symbols) and 150°C (red open symbols).



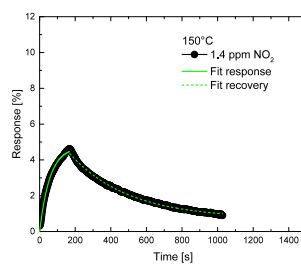
(a)



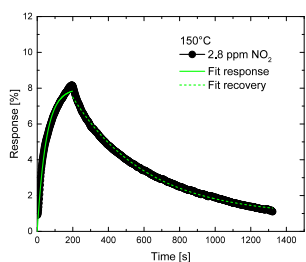
(b)



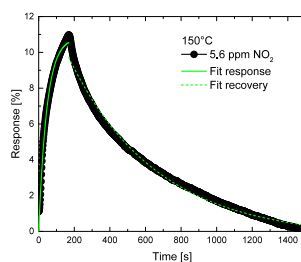
(c)



(d)

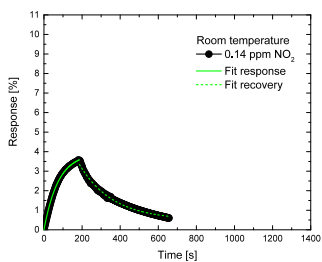


(e)

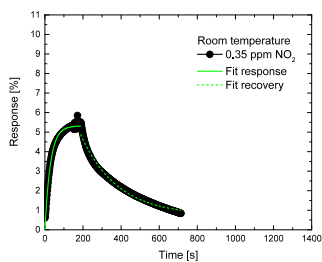


(f)

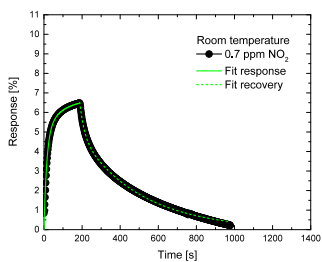
Figure A13: Fits of the response and recovery transients to different pulses of NO_2 at 150°C based on a single site isotherm (equations (2) and (3)): (a) 0.14 ppm, (b) 0.35, (c) 0.7 ppm, (d) 1.4 ppm, (e) 2.8 ppm and (f) 5.6 ppm.



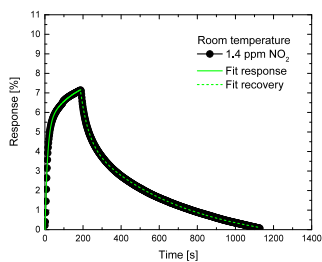
(a)



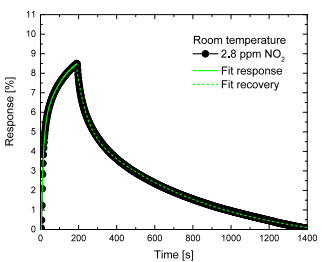
(b)



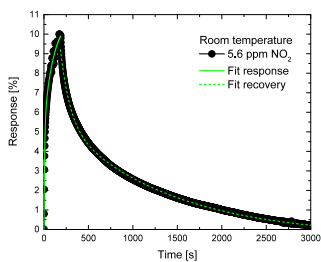
(c)



(d)



(e)



(f)

Figure A14: Fits of the response and recovery transients to different pulses of NO_2 at room temperature: (a) 0.14 ppm and (b) 0.35 ppm were fitted by a single site isotherm (equations 4.5 and 4.6), (c) 0.7 ppm, (d) 1.4 ppm, (e) 2.8 ppm and (f) 5.6 ppm were fitted by a two-site isotherm (equation 4.7 and 4.8).

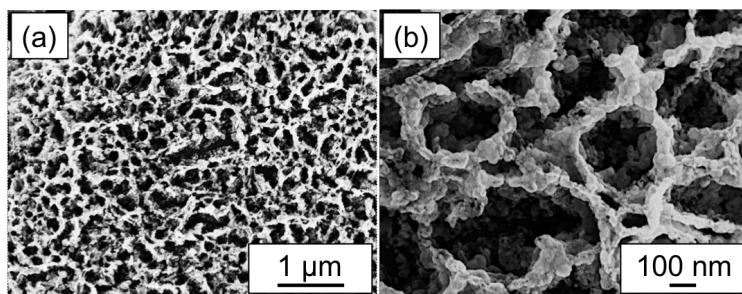


Figure A15: SEM images at different magnifications of nanoporous NiO film after gas sensing experiments.

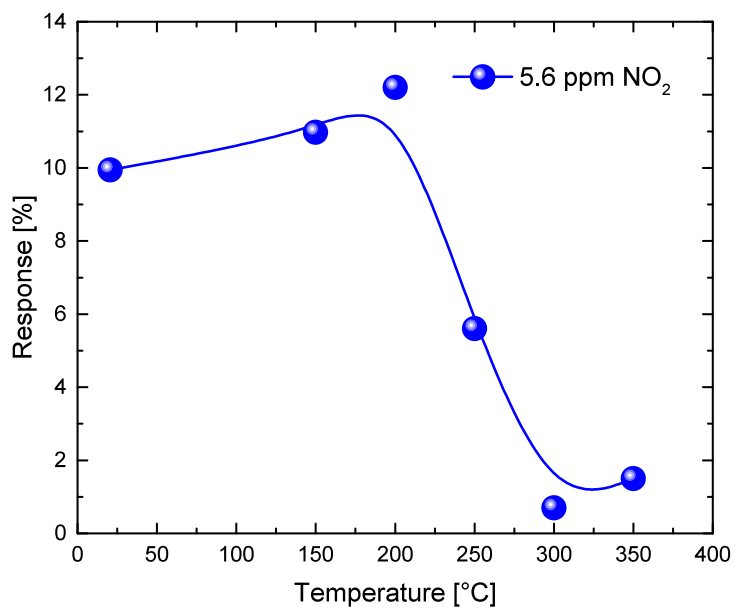
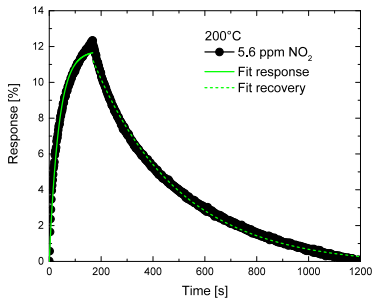
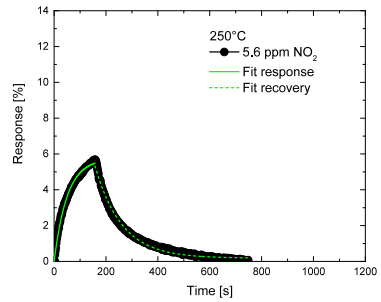


Figure A16: Response to a 5.6 ppm NO₂ pulse at various temperatures.

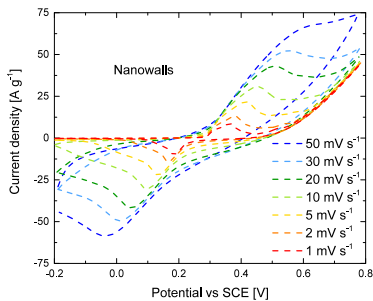


(a)

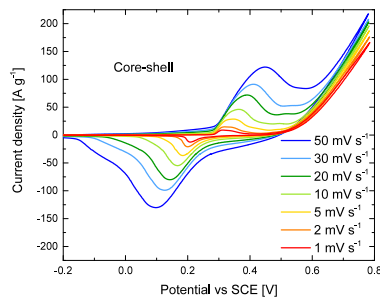


(b)

Figure A17: Fits of the response and recovery transients to a 5.6 ppm NO_2 pulses at (a) 200°C and (b) 250°C based on a single site isotherm (equations 4.5 and 4.6).

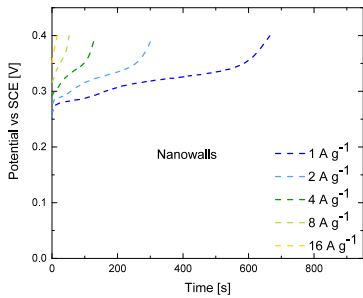


(a)

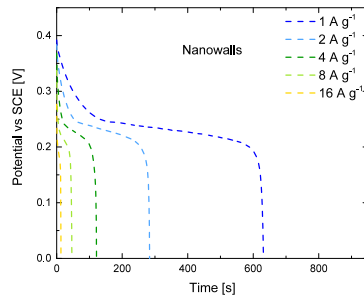


(b)

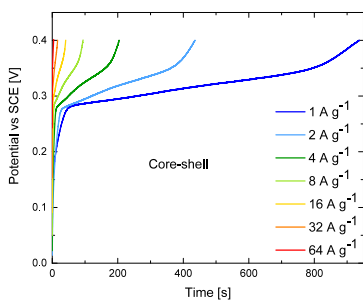
Figure A18: CV curves of nanowalls (a) and core-shell (b) recorded at different scan rates ($1\text{--}50 \text{ mV s}^{-1}$) in the potential range $-0.2\div 0.8 \text{ V}$ in 1 M KOH .



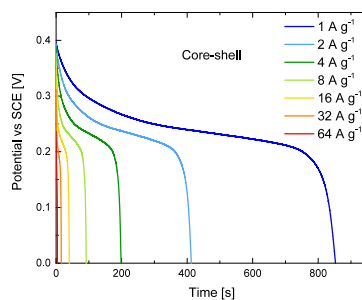
(a)



(b)



(c)



(d)

Figure A19: Galvanostatic charge and discharge curves of (a), (b) nanowalls, and (c), (d) core-shell recorded at different current densities (1-64 A g⁻¹) in 1 M KOH.

Specific capacity Q_s [mAh g⁻¹] was calculated from the reduction (discharge) peak in CV curves according to the following equation

$$Q_s = \frac{1}{m \frac{dV}{dt}} \int I dV \quad (9)$$

where I is the current density [A cm⁻²], m is the specific mass of the active material [g cm⁻²] and $\frac{dV}{dt}$ is the scan rate [V s⁻¹].

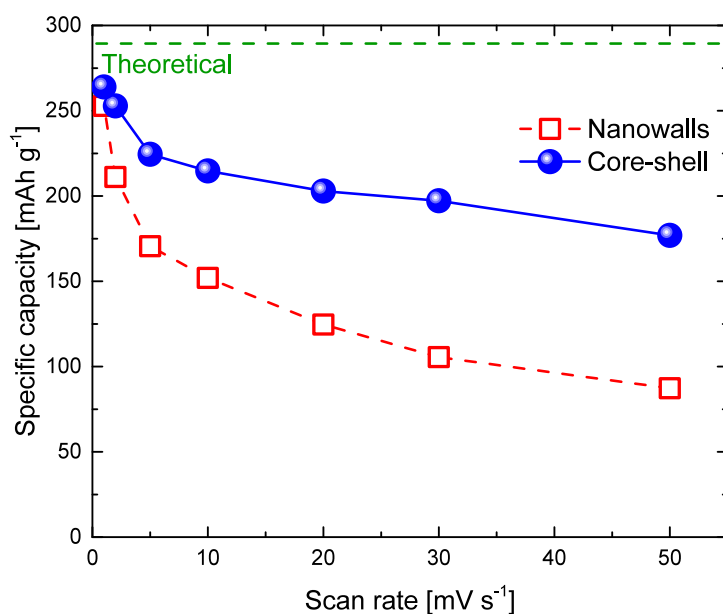


Figure A20: Specific capacity of nanowalls (red open squares) and core-shell (blue spheres) as function of scan rate as obtained by CV curves.

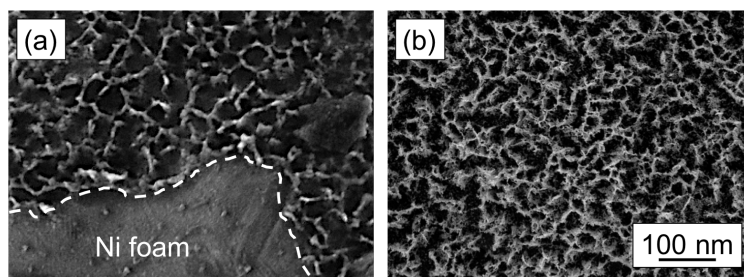


Figure A21: SEM images of (a) Ni(OH)_2 nanowalls and (b) $\text{Ni(OH)}_2@$ Ni core-shell nanochains after cycling stability test.

Randles-Sevcik equation was used to evaluate OH⁻ ions diffusion coefficient

$$I_p = 0.4463nFAC \left(\frac{nF\nu D}{RT} \right) \quad (10)$$

where I_p is the peak current [A], n is the number of electron involved in the redox process, F is the Faraday constant (96485 C mol⁻¹), C is the concentration of the diffusing species [mol cm⁻³], ν is the scan rate [V s⁻¹], D is the diffusion coefficient [cm² s⁻¹], R is the gas constant (8.314 J mol⁻¹ K⁻¹) and T is the temperature [K].

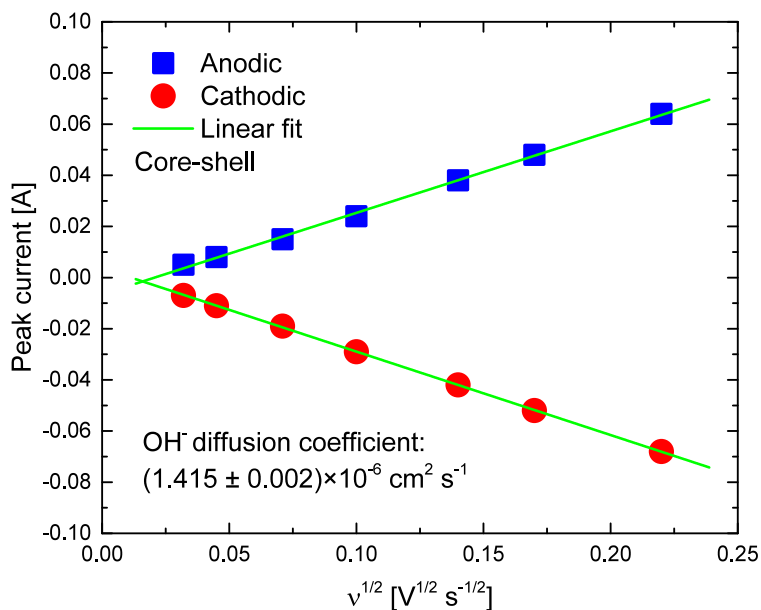


Figure A22: Anodic (blue squares) and cathodic (red circles) peaks current of core-shell versus scan rates, as obtained by CV curves.

Curriculum Vitae

Mario Urso was born in Catania (Italy) on October 21st, 1992.

Education

Post-doc position

at the University of Catania since December 2019

Supervisor: Prof. S. Mirabella

PhD in Materials Science & Nanotechnologies

at the University of Catania (October 2016 - October 2019)

Thesis title: **Novel Ni-based Nanostructures: Synthesis and Application in Sensing and Energy Storage**

Supervisors: Prof. F. Priolo, Prof. S. Mirabella

2019 **Visiting student** at the Tel Aviv University, Tel Aviv (Israel) working from January to April 2019 (during the PhD course) at the Department of Physical Electronics in the group of Prof. Y. Shacham-Diamand
Project: “*Impedimetric DNA sensors for PCR-free Mycoplasma agalactiae detection*”

2016 **Master Degree in Physics** [110/110] cum laude
at the University of Catania, with a dissertation entitled:
“*Synthesis and characterization of Ni nanostructures for non-enzymatic glucose detection*”
Supervisors: Prof. F. Priolo, Prof. S. Mirabella

2014 **Bachelor Degree in Physics** [110/110] cum laude
at the University of Catania, with a dissertation entitled:
*“Impact of photonic crystals on light emission and trapping in
LEDs and solar cells”*
Supervisors: Prof. F. Priolo, Dr. M. P. Miritello

Collaboration with the following institutions:

- CNR-IMM, Catania, Italy
- STMicroelectronics, Catania, Italy
- University of Messina, Department of Engineering, Messina, Italy
- University of Catania, Department of Agriculture, Food and Environment, Catania, Italy
- Experimental Zooprophyllactic Institute of Sicily, Palermo, Italy
- Tel Aviv University, Department of Physical Electronics, Tel Aviv, Israel

Oral presentations

1. **9th National Days on Energy Harvesting and Storage**
May 23-24th, 2019, Blois (France)
Title: *“Novel Ni-based nanostructures for hybrid supercapacitors”*
Invited author
2. **FisMat 2019**
September 30th-October 4th, 2019, Catania (Italy)
Title: *“Ni(OH)₂@Ni core-shell nanochains as low-cost high-rate performance electrode for energy storage applications”*
Presenting author
3. **FisMat 2019**
September 30th-October 4th, 2019, Catania (Italy)
Title: *“Low-cost synthesis of NiO nanofoam for selective NO₂ detection at room temperature”*
Presenting author

4. **FisMat 2019**
September 30th-October 4th, 2019, Catania (Italy)
Title: *“PCR-free Mycoplasma agalactiae electrochemical sensor based on Au decorated NiO nanowalls”*
Presenting author
5. **EMRS Fall Meeting 2019**
September 16-19th, 2019, Warsaw (Poland)
Title: *“Ni(OH)₂@Ni core-shell nanochains as low-cost high-rate performance electrode for energy storage applications”*
Presenting author
6. **EMRS Fall Meeting 2019**
September 16-19th, 2019, Warsaw (Poland)
Title: *“Low-cost synthesis of NiO nanofoam for selective NO₂ detection at room temperature”*
Presenting author
7. **EMRS Spring Meeting 2019**
May 27-31st, 2019, Nice (France)
Title: *“Low-cost synthesis of NiO nanofoam for selective room temperature NO₂ detection”*
Presenting author
8. **Materials.it 2018**
October 22-26th, 2018, Bologna (Italy)
Title: *“Supercapacitive properties of Ni-based nanostructures grown by chemical bath deposition”*
Presenting author
9. **Frontiers in Nanomaterials for Energy Harvesting and Storage**
August 27-29th, 2018, Tours (France)
Title: *“Supercapacitive properties of Ni-based nanostructures grown by chemical bath deposition”*
Presenting author

10. **EMRS Spring Meeting 2018**
June 18-22nd, 2018, Strasbourg (France)
Title: *“Optimization of chemical bath deposition of Ni oxide nanostructures for non-enzymatic glucose detection”*
Presenting author
11. **EMRS Spring Meeting 2018**
June 18-22nd, 2018, Strasbourg (France)
Title: *“Supercapacitive properties of Ni based nanostructures”*
Presenting author
12. **4° Convegno nazionale dei sensori**
February 21-23rd, 2018, Catania (Italy)
Title: *“Enhanced sensitivity in non-enzymatic glucose detection by improved growth kinetics of Ni based nanostructures”*
Presenting author
13. **FisMat 2017**
October 01-05th, 2017, Trieste (Italy)
Title: *“Low-cost and controlled synthesis of Ni nanofoam for non-enzymatic glucose sensing”*
Presenting author
14. **Materials.t 2016**
December 12-16th, 2016, Aci Castello (Italy)
Title: *“NiO based nanostructures for low-cost, high sensitive glucometer devices”*
Presenting author

Poster presentations

1. **EMRS Fall Meeting 2019**
September 16-19th, 2019, Warsaw (Poland)
Title: *“Enhanced sensitivity in non-enzymatic glucose detection by improved growth kinetics of Ni-based nanostructures”*
Presenting author

2. **EMRS Spring Meeting 2019**
May 27-31st, 2019, Nice (France)
Title: “*Ni(OH)₂@Ni core-shell nanochains: a low-cost high-rate performance electrode for energy storage applications*”
Presenting author
3. **The Fred Chaoul 12th Annual Workshop on Nanoscience and Nanotechnology**
February 19-21st, 2019, Dead Sea (Israel)
Title: “*Low-cost synthesis of Ni-based nanostructures for sensing and energy storage*”
Presenting author
4. **EMRS Spring Meeting 2017**
May 21-26th, 2017, Strasbourg (France)
Title: “*Ni(OH)₂/Ni for low-cost, high sensitive glucometer devices*”
Presenting author

Schools

1. **Scanning Electron Microscopy in Materials Science**
December 12-15th, 2017, Bologna (Italy)
2. **International School of Materials for Sustainable Development and Energy 1st course “Materials for Energy and Sustainability – ISMES VII”**
July 06-13th, 2018, Erice (Italy)

Awards

1. **Graduated Student Award of the European Materials Research Society**
EMRS Fall Meeting 2019, September 16-19th, 2019, Warsaw (Poland)
Symposium M: “Metal oxide- and oxyhydride-based nanomaterials for energy and environment-related applications”

2. Graduated Student Award of the European Materials Research Society

EMRS Spring Meeting 2017, May 22-26th, 2017, Strasbourg (France)

Symposium T: “Synthesis, processing and characterization of nanoscale multi functional oxide films VI”

List of publications

This thesis is based on the following publications:

1. **Enhanced sensitivity in non-enzymatic glucose detection by improved growth kinetics of Ni-based nanostructures**
M. Urso, G. Pellegrino, V. Strano, E. Bruno, F. Priolo, S. Mirabella
Nanotechnology, Vol. 29, n. 16, p.165601 (2018)
DOI: <https://doi.org/10.1088/1361-6528/aaacb6>
2. **Ni(OH)₂@Ni core-shell nanochains as low-cost high-rate performance electrode for energy storage applications**
M. Urso, G. Torrisi, S. Boninelli, C. Bongiorno, F. Priolo, S. Mirabella
Scientific Reports, Vol. 9, n. 7736 (2019)
DOI: <https://doi.org/10.1038/s41598-019-44285-1>
3. **Room temperature detection and modelling of sub-ppm NO₂ by low-cost nanoporous NiO film**
M. Urso, S. G. Leonardi, G. Neri, S. Petralia, S. Conoci, F. Priolo, S. Mirabella
Accepted for publication in Sensors and Actuators B: Chemical.
4. **Acetone sensing and modelling by NiO nanowalls**
M. Urso, S. G. Leonardi, G. Neri, S. Petralia, S. Conoci, F.

Priolo, S. Mirabella

Accepted for publication in Materials Letters

5. **PCR-free Mycoplasma agalactiae electrochemical sensor based on Au decorated NiO nanowalls**

M. Urso, S. Tumino, S. Bordonaro, G. R. Loria, A. Criscione, D. Marletta, A. Avni, Y. Shacham-Diamand, F. Priolo, S. Mirabella
In preparation

Other publications

6. **Hybrid Nickel-free graphene/porphyrin rings for photodegradation of emerging pollutants in water**

M. Ussia, M. Urso, M. Miritello, E. Bruno, G. Curcuruto, D. Vitalini, G. Condorelli, M. Cantarella, V. Privitera, S. C. Carroccio

RSC Advances, Vol 9, pp.30182-30194 (2019)

DOI: <https://doi.org/10.1039/C9RA06328E>

7. **A new synthetic route for the growth of α -FeOOH/NH₂-Mil-101 films on copper foils for high surface area electrodes**

F. Monforte, M. Urso, A. Alberti, E. Smecca, S. Mirabella, C. Bongiorno, G. Mannino, G. Condorelli

ACS Omega, Vol. 4, n. 20, pp.18495–18501 (2019)

DOI: <https://doi.org/10.1021/acsomega.9b01840>

Acknowledgments

Ringrazio il mio tutor, il prof. Francesco Priolo, per l'entusiasmo con cui mi ha seguito in tutta la mia carriera accademica, dalla laurea triennale al dottorato di ricerca, trasmettendomi la passione per la fisica sperimentale della materia.

Il prof. Salvo Mirabella è stato per me, ancor prima che un eccellente tutor e mentore, un modello di ricercatore, insegnante e di uomo a cui ispirarsi. A lui vanno i miei più profondi ringraziamenti per la sua disponibilità, cordialità e pazienza, per i suoi preziosi consigli e insegnamenti, per l'entusiasmo e la passione con cui ha guidato la mia attività di ricerca, per la fiducia che ha riposto in me e per avermi sempre spronato a superare i miei limiti.

Voglio poi ringraziare il prof. Giovanni Neri e, in particolare, il Dr. Gianluca Leonardi per aver condiviso con me le loro profonde competenze sui sensori di gas a base di ossidi metallici.

I would like to thank prof. Yosi Shacham-Diamand for the opportunity to work in his group at the Tel Aviv University, increasing my knowledge in electrochemical sensors. Also, I would like to thank prof. Adi Avni for his valuable advices, and prof. Yuval Ebenstein and Dr. Christian Heck who showed me how to work with DNA. I am deeply grateful to Dr. Alexandra Inberg and Dr. Yelena Sverdlov for sharing their expertise on electroless deposition method with me. A special thanks goes to my friends and labmates at the Tel Aviv University: Dayananda, Chithira, Aakash, Kian, Tali, Idan and Maya.

Ringrazio la prof.ssa Maria Grazia Grimaldi, coordinatore del dottorato di ricerca in "Scienza dei Materiali e Nanotecnologie", e tutto

il personale del CNR-IMM Unità di Catania (dottorandi, assegnisti, ricercatori, tecnici e amministrativi) con cui ho avuto modo di interagire durante il dottorato. A tal proposito, un ringraziamento speciale va a Maria, Martina e Antonio per aver condiviso con me questo percorso faticoso ma anche ricco di soddisfazioni.

Ringrazio Giacomo e Saro per la sincera amicizia che è nata tra noi, e Davide per la lunga e vera amicizia che ci lega.

Infine, ringrazio la mia famiglia per il costante sostegno e, più di ogni altro, Martina, che con il suo autentico amore mi ha cambiato la vita. Ti amo!

La ricerca del sogno impossibile continua...

